INVESTIGATING THE ASTROPHYSICAL RP-PROCESS THROUGH ATOMIC MASS MEASUREMENTS

BY

JASON ALLAN CLARK

A Thesis Submitted to
the Faculty of Graduate Studies
in Partial Fulfillment of the Requirements for the Degree of

DOCTOR OF PHILOSOPHY

Department of Physics and Astronomy
University of Manitoba
Winnipeg, Manitoba

Abstract

The Canadian Penning Trap (CPT) mass spectrometer at the Argonne National Laboratory makes precise mass measurements of both stable and unstable nuclides. To date, more than 60 radioactive isotopes having half-lives as short as one second have been measured with the CPT with a precision ($\Delta m/m$) approaching 10^{-8}. This thesis will present measurements made of nuclides along the rp-process path, which describes a process resulting from a series of rapid proton-capture reactions in an astrophysical environment. One possible site for the rp-process mechanism is an x-ray burst which results from the rapid accretion of hydrogen and helium from one star onto the surface of its neutron star binary companion. Mass measurements are required as key inputs to network calculations used to describe the rp-process in terms of the abundances of the nuclides produced, the light-curve profile of the x-ray bursts, and the energy produced. This thesis will describe the CPT apparatus, explain the method used to make precise mass measurements, and present the masses of the "waiting-point" nuclides ^{68}Se and ^{64}Ge. The mass measurement results, when used in x-ray burst models, confirm both ^{68}Se and ^{64}Ge as waiting-point nuclides which delay the rp-process by approximately 30 s and 7 s respectively.

Acknowledgements

Throughout my entire program of study, numerous individuals have helped me along the way. Without their assistance, completing this thesis would have been much more difficult. In fact, so many people have been involved that recognizing every contribution is an impossible task. Nevertheless, there are a few people who deserve special mention.

As for any graduate student, choosing one good advisor can be challenging. I was fortunate to find two. Both Kumar Sharma and Guy Savard set high standards which drove me to always do better, try harder, and strive for more. Their humour, sharp wit, guidance, devotion, and endurance are all qualities I have admired. Leonardo da Vinci has been quoted as saying "Poor is the pupil who does not surpass his master." I hope, for my sake, he was only referring to pupils of art. If I become half the scientists that Guy and Kumar are today, I will consider myself lucky.

Any contribution I may have made to science is at least partly due to the hard work of graduate students who preceded me. Pedro Martinez and Hiroshi Fukutani both played a big role in the initial development, assembly, and testing of the experimental apparatus. They set a strong foundation for my thesis work. I also thank the graduate students who started and completed their theses during my program, namely Chantal Boudreau, Michael Maier, Joseph Vaz, and Yuyan Wang. I have lived with all of them while in Chicago, and the fact that we managed not to get on each others nerves while both working and living together is proof of their adaptive nature. I have no doubt they will succeed in all their pursuits. To the future students, Daniel Lascar and Jennifer Fallis, I wish you the best of luck. I am confident the project has been left in good hands, and I look forward to working with you in the future. There have been many postdocs and summer students with whom I have had the privilege to work. I will refrain from mentioning their names since I am fearful I will forget a number of them. Nevertheless, their innumerable contributions are much appreciated. My life was made much easier because of all the assistance from the staff both at the University of Manitoba and Argonne National Laboratory. The ATLAS operations staff, secretaries, machinists, engineers, and support staff all deserve an award. Any success I have is as much theirs as it is mine.

Last, but certainly not least, I thank my family and friends. I'm not so certain I would have completed this thesis if it were not for their encouragement and support during some especially trying times. To Mom and Dad. Mom always found the time to take care of what I consider to be life's annoyances, such as cooking, cleaning, and laundry, while I was home. If there was anything that she could do for me, she did it without question. Although I can't pinpoint the moment in my life when I first became interested in physics and astronomy, I do fondly recall early childhood memories of Dad showing me the constellations during harvest nights. His quiet encouragement, yet competitive spirit, has been most definitely responsible for all I have achieved. For their unconditional love and support in many forms throughout the years, it is to the memory of Mom and Dad that I dedicate this thesis.

To the loving memory of
Mom and Dad

“mass: The quantity of matter which a body contains, irrespective of its bulk or volume.”

Webster’s Revised Unabridged Dictionary

“The crux... is that the vast majority of the mass of the universe seems to be missing.”

William J. Broad

“The universe is full of magical things, patiently waiting for our wits to grow sharper.”

Eden Phillpotts

Contents

List of Figures

List of Tables

Chapter 1

Introduction: The Goal

The leviathan universe is full of wonders that never cease to amaze us. From the displays of the aurora borealis to the echo of the Big Bang as heard through the cosmic microwave background, our curiosity drives us to unravel these astronomical phenomena. An x-ray burst is one such event in which a tremendous amount of energy is released in brief increments from what is believed to be a neutron star. The study of these x-ray bursts, however, directs our attention from the massive stellar object to a minuscule, but basic building block of matter: the atomic nucleus.

One of the basic properties of a nucleus is its mass. The mass of the nucleus cannot be simply calculated by summing the masses of the constituent protons and neutrons. The small but measurable mass equivalent of the binding energy must be subtracted from the constituent masses. Take the helium nucleus, for example, which has two protons and two neutrons. Bringing two protons together to within a distance of 2 fm, roughly equivalent to the size of the helium nucleus, requires on the order of 0.6 MeV of energy. However, the energy equivalent of the mass used to bind the helium nucleus has been measured to be approximately 28 MeV, or about 7 MeV per nucleon, more than enough to overcome the Coulomb repulsion of the protons. Indeed, helium is an extremely stable nucleus. The neutrons also help to space the protons and introduce additional stability from pairing effects between protons and neutrons. Measuring the masses of a wide variety of nuclides, therefore, provides information on the forces which bind the nucleons together.

This thesis will bring the large and small worlds together whereby the mass measurements of some select nuclides will help to explain the nature of x-ray bursts. Just as the energy output of a hydrogen bomb is related to the release of energy which binds protons and neutron together to form a nucleus, the observed explosions of x-ray bursts are attributed to similar energy releases on the surface of a neutron star.

Anyone with an undergraduate degree in physics should not have any difficulty understanding the concepts presented throughout this document. Although the material is presented in sequence, from the first chapter which discusses the motivation underlying the mass measurements reported here to the last chapter which summarizes the results, the chapters can be read in any order as the material within each chapter is self-sustaining with few exceptions. With that said, more insight will be gained if this thesis is read in sequence. Chapter 1 gives an introduction to x-ray bursts and provides the justification for mass measurements of particular nuclides. Chapter 2 provides the theoretical background for the Paul trap and Penning trap which are two types of ion traps used to confine ions in space. Many such traps are utilized throughout the Canadian Penning trap (CPT) apparatus to cool, accumulate and study the trapped ions. The entire CPT apparatus is described in Chapter 3, from the production of the nuclides of interest to the precision Penning trap where the mass measurements take place. Techniques to efficiently and quickly transfer ions from their initial production to their final detection while simultaneously minimizing systematic effects will also be presented in Chapter 3. Within Chapter 4, the reader will find details about the mass measurements themselves and a discussion regarding the issue of precision versus accuracy as it applies to Penning trap mass measurements with the CPT. Chapter 5 relates atomic masses to x-ray burst timescales and shows the consequences of the masses reported here on the rp-process. Finally, a summary of the thesis is presented in Chapter 6 with comments pertaining to the future of the CPT.

1.1 The astrophysical rp-process

Observations of one class of astronomical explosive events known as x-ray bursts have indicated that a possible candidate for their source are binary star systems consisting of a red giant and neutron star. Since 50 % of all stars are estimated to be members of binary star systems, an abundance of stars are thought to participate in x-ray bursts at some point in their evolution. Neutron stars involved in x-ray bursts are compact objects with a typical mass of 1.4 times the mass of the sun, or approximately 2.8×10^{30} kg, but with a radius of only 10^4 m. When compared with the 6.95×10^8-meter radius of the sun, neutron stars are much more compact objects with extreme gravitational pressures on the surface of the star. In fact, the mass density of a neutron star is comparable to that of an atomic nucleus! If the red giant companion is of sufficient size or proximity to the neutron star, hydrogen and helium from the gas giant can escape its gravitational pull and accrete onto the surface of the neutron star. Consider the accretion of a single proton. At first glance, the nuclear physics contribution to the overall x-ray burst phenomenon seems to be negligible since the gravitational energy released per accreted baryon is on the order of 200 MeV, almost two orders of magnitude greater than the energy which would be released from fusion of the proton. However, the continual accretion of baryonic material onto the surface of the neutron star at rates of $\sim 10^{-9}\ M_{\odot}\ \mathrm{yr}^{-1}$, where $M_{\odot} \equiv 1$ solar mass, subjects the accreted material to an ever-increasing change in pressure and temperature until fusion of the material becomes possible [1], at which point the accumulated material burns rapidly and results in a thermonuclear runaway [2] with temperatures reaching up to 3×10^9 K. At this time, the nuclear energy released during the rapid series of proton capture reactions, termed the rp-process [3], is sufficient to be observed above the relatively constant accretion background. The resulting burst of energy is ultimately observed as the x-ray burst [4] with typical durations of 10 - 100 seconds.

During the thermonuclear runaway, the reaction path is dictated by thousands of

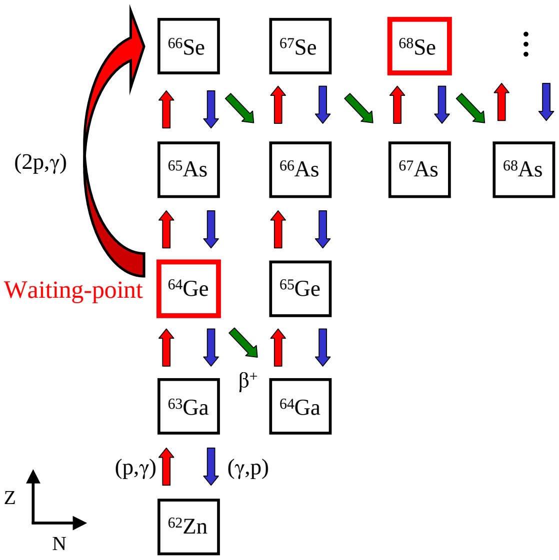

Figure 1.1: A section of the chart of the nuclides showing the rp-process path. Proton-capture reactions are shown by red arrows, photodisintegration reactions are indicated by the blue arrows, and β-decay processes are shown by the green arrows. Each waiting-point nuclide can be destroyed either by β-decay or through the rapid successive capture of two protons.

reaction rates, including those of predominant proton-capture, photodisintegration, and β-decay reactions. For the most part, β-decay reactions occur less frequently than the proton-capture or photodisintegration reactions. Therefore, the rp-process, as shown in Fig. 1.1, proceeds by a series of rapid-proton capture reactions until reaching a nuclide along this path where the inverse photodisintegration reaction rate is comparable to the proton-capture rate. This nuclide is termed a "waiting-point" nuclide. At such nuclides, the rp-process essentially stalls and cannot continue until the destruction of the waiting-point nuclide, either through its β decay, or through the rapid capture of two protons to bypass the impeding nucleus. Another series of reactions then ensues until reaching the next waiting-point nuclide. The timescale of the rp-process, or equivalently the light-curve profile of x-ray bursts, depends largely upon the contribution of the individual delays at each waiting-point nuclide. Since these delays are dependent upon the reaction rates of the nuclides involved, information about β-decay half-lives and energy levels which can be thermally populated are necessary to assess the delay at each waiting-point nuclide. Furthermore, since the photodisintegration rates are exponentially dependent upon differences in the masses of the nuclides involved [1], masses of potential waiting-point nuclides are critical. Even a small uncertainty in the masses yields a large uncertainty in the effective half-lives of, or delays at, the waiting-point nuclides. With temperatures of $\sim 10^9$ K which are reached during x-ray burst events, a mass precision of at least kT c^{-2} ($\sim$100 keV c^{-2}) is required. Such a precision is obtained easily with Penning trap mass spectrometers.

Before the delay at each waiting-point nuclide can be determined, the potential waiting-point nuclides must be identified. Due to the predicted structure of the proton drip-line, whereby isotopes with fewer neutrons can exist for nuclides with an even number of protons, the even Z nuclei with N=Z are found to be waiting-point nuclide candidates. Since the delay each waiting-point nuclide contributes to the timescale of the rp-process can be at most equal to its β-decay lifetime, the waiting-point nuclides which could have the biggest influence are those at the beginning of the N=Z chain since they have the longest β-decay lifetimes. In particular, ^{64}Ge and ^{68}Se, with β-decay half-lives of 63.7 s and 35.5 s respectively, are the most important waiting-point nuclides to consider [1].

The dependence of the delay in the rp-process upon the proton-capture Q value, Q_p, for ^{68}Se can be seen in Fig. 1.2, where typical parameters which describe the conditions during x-ray bursts are used to generate the plotted curve. (See Appendix A for a discussion regarding Q values.) For small (even negative) Q_p values, the proton-capture rate on ^{68}Se is small in comparison with the inverse photodisintegration rate. Therefore, bypassing the impeding intermediate nuclide by capturing two protons in rapid succession is highly improbable, and the rp-process is delayed until the β decay of ^{68}Se occurs. For larger Q_p values, the increased likelihood of destruction of ^{68}Se via proton-capture decreases the effective half-life of ^{68}Se since the rp-process can bridge the intermediate nucleus and continue before the β decay of ^{68}Se takes place. As of

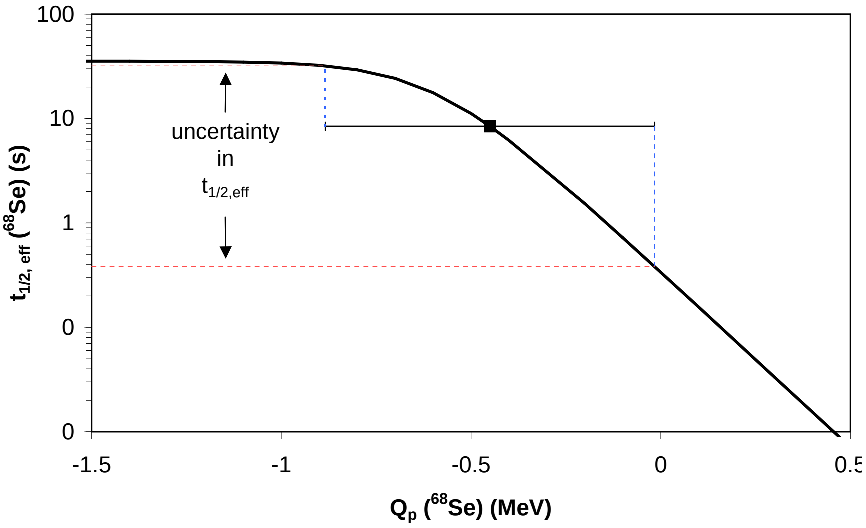

Figure 1.2: Plotted is the effective delay in the rp-process due to the waiting-point nuclide ^{68}Se. The solid black line shows the dependence of the delay upon the proton-capture Q value and the datum point represents one estimate of the actual Q value as taken from the 1995 Atomic Mass Evaluation [5]. The extents of the error bars are projected onto the curve with blue lines and translate via the red lines to an uncertainty in the effective delay.

1995, the best estimate for the Q value was from the 1995 Atomic Mass Evaluation [5]. (The results from the evaluation are published as a table of masses, the value for each mass having been determined from averaging experimental input; nuclides with no empirical data, such as ^{68}Se, are estimated based upon systematic trends arising from the evaluated set of measured masses.) Due to the uncertainty in the Q value for the waiting-point nuclide ^{68}Se, the effective delay could be as little as 380 milliseconds or as long as 31.9 seconds. Since the duration of the x-ray burst is observed to be typically between 10 and 100 seconds, an uncertainty of 32 seconds in the delay at ^{68}Se does not allow significant conclusions.

Since the β-decay half-life of ^{64}Ge is almost twice that of ^{68}Se, the delay in rp-process due to ^{64}Ge could be even more considerable. Under the same assumptions as those used to generate the curve for ^{68}Se earlier, the effective delay for ^{64}Ge as of 1995 was calculated to be between 2 milliseconds and 2.1 seconds as can be seen

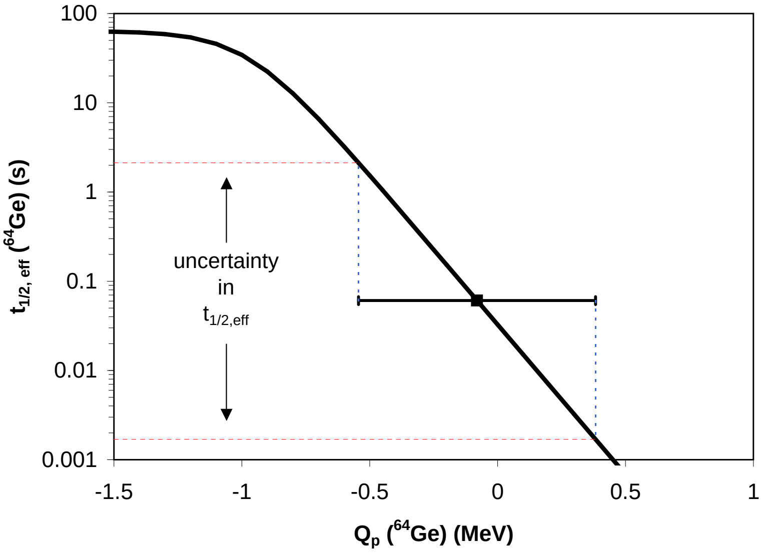

Figure 1.3: Plotted is the effective delay in the rp-process due to the waiting-point nuclide ^{64}Ge. See the caption of Fig. 1.2 for details regarding the plot.

in Fig. 1.3. Since the uncertainty in the effective delay at ^{64}Ge does not represent as significant a portion of the total timescale for the x-ray burst (100 s) as does the interval for ^{68}Se, a mass measurement was first performed on ^{68}Se.

Overall, an explanation of the x-ray burst timescale requires mass information of waiting-point nuclides. Obtaining these measurements is the subject of the next section.

1.2 Measuring the masses of nuclides

The mass precision which is required to characterize x-ray bursts dictates the method used to obtain the mass information. Mass models provide one option to generate values for masses of nuclides which have never been measured. However, the models themselves have parameters which are adjusted to fit the set of known, or measured, masses and the different models are known to diverge significantly when predicting the masses of nuclides far from stability. Even among the set of measured masses used to constrain the models, average deviations in the 600 keV range are not unusual.

This level of precision is inadequate for x-ray burst network calculations.

In the absence of reliable models, the mass measurements of the desired nuclides is the only alternative. However, measurements of waiting-point nuclides ^{68}Se and ^{64}Ge, for example, are difficult. Due to their short half-life, these nuclides are not natural to Earth and must be produced by nuclear reactions at accelerator facilities, such as the ATLAS accelerator at Argonne National Laboratory (ANL). The combination of the short half-lives and low production rates demands a mass measurement apparatus which is both fast and efficient. Adding to the complication of any measurement process is the presence of systematic effects which can render a measurement useless, despite the statistical precision achieved. Indirect mass measurements, through reaction and decay Q values, are often used to estimate the masses of nuclides far from stability. However, systematic effects present in these measurements accumulate along the reaction or decay chains linking the mass of an extremely proton-rich or neutron-rich nuclide to a well-known reference mass. Because of this, only one 'weak' link in the chain is enough to render an exotic mass inaccurate. Instead, a direct mass measurement of the desired nuclides with an accuracy to better than 100 keV is desirable for modelling x-ray bursts.

Since the early days of J.J. Thomson [6] whose work first demonstrated the existence of isotopes among stable elements, technological advances and the evolution of various techniques have pushed the bounds of precision mass spectrometry. As seen in Fig. 1 of Ref. [7], the precision of mass measurements has increased significantly from the 10^7 parts per billion (ppb) in Thomson's era to 0.01 ppb today. (See Ref. [8] and Ref. [9] for recent articles about the high precision currently achievable.) This change in the precision of mass determinations corresponds to roughly an order of magnitude improvement every 10 years, or 20 dB per decade! The Penning trap mass spectrometer, in which a mass is determined by a measurement of the ion's cyclotron frequency, is the latest advance in technology responsible in improving mass precision. The high accuracy and sensitivity obtainable with frequency measurements is one advantage Penning trap mass spectrometers have over its predecessor – the deflection type mass spectrometers, only one of which remains active today [7]. In addition, the motion of ions within a Penning trap is well understood such that systematic effects can be minimized.

The mass measurements required for the study of x-ray bursts are of rare isotopes. Due to their short-lived nature, mass spectrometers must be online with the accelerator facility which creates the nuclides. The first such direct mass measurements were reported in 1975 [10]. Now, a number of online mass spectrometers exist, including SPEG [11] and CSS2 [12] at GANIL (France), the ESR storage ring at GSI (Germany) [13], the ISOLTRAP Penning trap at CERN (Switzerland) [14, 15], and of course the CPT at ANL (United States). The success of the ISOLTRAP and CPT Penning trap mass spectrometers have contributed in part to an explosion of new Penning trap mass spectrometer facilities about to come online. These include JYFLTRAP (IGISOL, Finland) [16], SHIPTRAP (GSI, Germany) [17], LEBIT (MSU, United States) [18], TITAN (TRIUMF, Canada) [19], MAFFTRAP (FRM II, Germany) [20], and HITRAP (GSI, Germany) [21]. For more information on the up-and-coming Penning trap devices, see Ref. [22].

The CPT mass spectrometer, online at the ATLAS facility of ANL, was designed with the goal of achieving mass measurements with accuracies approaching 1 part per billion of the mass for weakly produced nuclides with half-lives as short as 50 ms. To meet the demands of an efficient, fast system which produces both precise and accurate mass measurements, the entire measurement apparatus consists of a wide variety of devices from the production target to the precision Penning trap itself. The absence, or malfunctioning, of any one of these devices puts a precise mass measurement in jeopardy. A description of the complex CPT apparatus can be found in Chapter 2 and Chapter 3, followed by our results for nuclides along the astrophysical rp-process, some of which had never been measured previously.

Chapter 2

Ion traps

High precision experiments require the accumulation of statistics and an extended observation time if possible. For the latter requirement, measurements of basic nuclear or atomic properties may be achieved by a suspension of the atoms in free space which is arguably most easily achieved by their manipulation using electric or magnetic fields or a combination of both. These fields require the atoms to be ionized, and the devices used to suspend them are known as ion traps.

2.1 Radio-frequency quadrupole ion traps

The first type of ion trap discussed here is one which confines ions via electric fields only. The required fields and the structures which provide these fields are presented below.

2.1.1 Ion confinement

The confinement of ions requires a restoring force $\vec{F}$ in each of the desired dimensions. In the simplistic one-dimensional case, the requirement is expressed mathematically as:

$$F_x = -k_x(x - x_o) \tag{2.1}$$

in which k_x is the restoring constant and x represents the distance along the one dimension from some central value x_o. In this manner, the force applied causes a particle with mass m to oscillate about the equilibrium position x_o with frequency $\omega = \sqrt{k_x/m}$ as can be seen from the solution to Eq. 2.1:

$$x = x_m \cos(\sqrt{k_x/m}\, t + \phi_o) + x_o. \tag{2.2}$$

Here, the constants of integration, determined from initial conditions, are x_m and ϕ_o. Under the influence of the force described by Eq. 2.1, the ion is restricted to move along the one dimension within positions $x_m + x_o$ and $x_m - x_o$. The position of the particle at time $t = 0$ is described by x_m, x_o, and ϕ_o.

If the particle has a charge q, then the presence of only an electric field $\vec{E}$ can provide the force described by Eq. 2.1:

$$F_x = qE_x = -k_x(x - x_o). \tag{2.3}$$

Since the potential V which describes such a field is determined via $\vec{E} = -\vec{\nabla}V$, then in the one dimensional case being considered:

$$V = \frac{k_x}{2q}(x - x_o)^2 + \varphi_o \tag{2.4}$$

with φ_o as an arbitrary constant potential. In the sections which follow, terms synonymous with φ_o and x_o are set to zero. The only consequence is that the confined ions move about a central value of $x = 0$ and in no way does this detract from the generality of the discussion.

Two dimensional confinement

A more applicable case of ion confinement involves restricting the ion motion in not one, but two dimensions. This requirement is realized with a potential of the form expressed in Eq. 2.4 generalized to two dimensions:

$$V = \lambda_x x^2 + \lambda_y y^2 \tag{2.5}$$

with $\lambda_x = \frac{k_x}{2q}$ in analogy to Eq. 2.4 and similarly for λ_y.

In a source free region of space, $\vec{\nabla} \cdot \vec{E} = 0$, and therefore:

$$\nabla^2 V = 0, \tag{2.6}$$

the well-known Laplace's equation. With the form of V from Eq. 2.5, the solution to Eq. 2.6 requires:

$$\lambda_x + \lambda_y = 0. \tag{2.7}$$

The trivial solution ($\lambda_x = \lambda_y = 0$) does not provide a restoring force. Instead, a solution to consider is:

$$\lambda_x = -\lambda_y \equiv \lambda. \tag{2.8}$$

This requirement, when combined with Eq. 2.5, shows that the potential,

$$V = \lambda(x^2 - y^2). \tag{2.9}$$

If $\frac{\varphi_o}{2}$ is chosen as the magnitude of the electric potential at coordinates $(x, y) = (r_o, 0)$ then $\lambda = \frac{\varphi_o}{2r_o^2}$. One option which provides the potential given in Eq. 2.9 are electrodes which lie on equipotential surfaces described by:

$$\frac{x^2}{r_o^2} - \frac{y^2}{r_o^2} = 1 \tag{2.10a}$$

at potential $\frac{\varphi_o}{2}$ and

$$\frac{x^2}{r_o^2} - \frac{y^2}{r_o^2} = -1 \tag{2.10b}$$

at potential $-\frac{\varphi_o}{2}$ as shown in Fig. 2.1. The above expressions describe two rectangular hyperboloids of opposite potential. The two hyperboloids are oriented perpendicular to each other since both are centered at $(x, y) = (0, 0)$ with one having vertices at $(x, y) = (\pm r_o, 0)$ and the other with vertices at $(x, y) = (0, \pm r_o)$. In a practical application, the hyperboloids are extended along the z-axis to create hyperbolic cylinders and the structure so formed is termed a "quadrupole mass filter" for reasons which will become clear.

With a potential of the form as expressed in Eq. 2.9 and shown in Fig. 2.2, the force exerted on the ions:

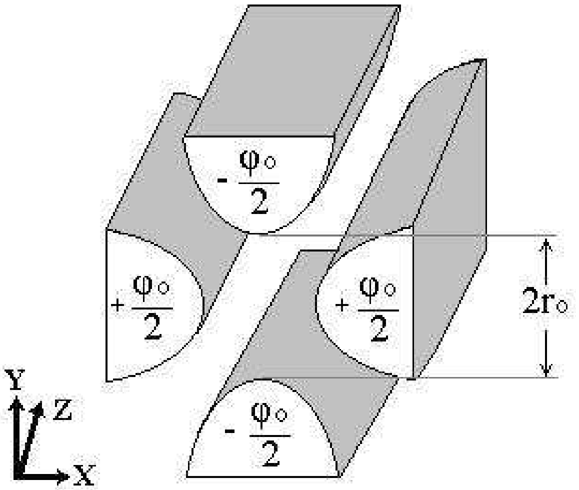

Figure 2.1: Rod structure which permits the confinement of ions in two dimensions.

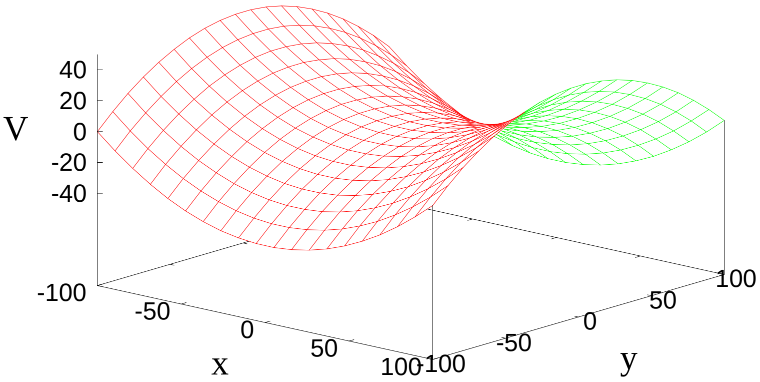

Figure 2.2: Plot of the “saddle” potential provided by Eq. 2.9 with $\lambda = 0.005$. Notice that ions are confined along the x-axis, but are repelled away from the origin along the y-axis.

$$\vec{F} = m(\ddot{x}\hat{x} + \ddot{y}\hat{y}) = q\vec{E} \tag{2.11}$$

$$= -q\vec{\nabla}V \tag{2.12}$$

$$= -\frac{q\varphi_o}{2r_o^2}(2x\hat{x} - 2y\hat{y}) \tag{2.13}$$

where $\frac{d^2x}{dt^2} \equiv \ddot{x}$ and $\hat{x}$ represents a unit vector pointing in the direction of the x-axis. The ion motion is therefore determined from the simultaneous solutions to the following equations of motion:

$$F_x = m\ddot{x} = -\frac{q\varphi_o}{r_o^2}x \tag{2.14a}$$

$$F_y = m\ddot{y} = \frac{q\varphi_o}{r_o^2}y. \tag{2.14b}$$

Careful examination of the above equations reveals that, although the ions are confined along the x-axis with simple harmonic motion characterized by frequency $\omega = \sqrt{\frac{q\varphi_o}{mr_o^2}}$, a particle along the y-axis experiences a force in a direction away from the origin which increases as the particle moves away from the origin. In other words, the ions are confined in one dimension, but not in both at the same time. What is required is a periodic potential which confines ions along one dimension for part of the time and confines in the other direction for the remainder of the time. The trick is to select a frequency of the oscillating potential which does not permit ions to escape along one dimension while confining in the other. Therefore, employing a requisite potential of the form:

$$\varphi_o = U_{dc} - V_{rf}\cos[\omega_{rf}(t - t_o)] \tag{2.15}$$

produces the following equations of motion when substituted into Eq. 2.14:

$$\ddot{x} + \frac{q}{mr_o^2}\{U_{dc} - V_{rf}\cos[\omega_{rf}(t - t_o)]\}x = 0 \tag{2.16a}$$

$$\ddot{y} - \frac{q}{mr_o^2}\{U_{dc} - V_{rf}\cos[\omega_{rf}(t - t_o)]\}y = 0 \tag{2.16b}$$

where t_o is the time when the ions first experience the alternating field.

With the substitution $\zeta = \omega t/2$, the above equations are transformed into the following:

$$\frac{d^2x}{d\zeta^2} + 4\frac{q}{m\omega^2 r_o^2}\{U_{dc} - V_{rf}\cos(2\zeta - 2\zeta_o)\}x = 0 \tag{2.17a}$$

$$\frac{d^2y}{d\zeta^2} - 4\frac{q}{m\omega^2 r_o^2}\{U_{dc} - V_{rf}\cos(2\zeta - 2\zeta_o)\}y = 0. \tag{2.17b}$$

If a and q are defined as:

$$a_x = -a_y = \frac{4qU_{dc}}{m\omega^2 r_o^2} \tag{2.18a}$$

$$q_x = -q_y = \frac{2qV_{rf}}{m\omega^2 r_o^2}, \tag{2.18b}$$

Eqs. 2.17 are reduced further to:

$$\frac{d^2x}{d\zeta^2} + \{a_x - 2q_x\cos(2\zeta - 2\zeta_o)\}x = 0 \tag{2.19a}$$

$$\frac{d^2y}{d\zeta^2} + \{a_y - 2q_y\cos(2\zeta - 2\zeta_o)\}y = 0. \tag{2.19b}$$

Both are of the form of the Mathieu equation with analytical solution [23]:

$$u(\zeta) = \alpha' e^{\mu\zeta} \sum_{n=-\infty}^{n=\infty} C_{2n} e^{2in\zeta} + \alpha'' e^{-\mu\zeta} \sum_{n=-\infty}^{n=\infty} C_{2n} e^{-2in\zeta} \tag{2.20}$$

with complex constant $\mu = \alpha + i\beta$. The integration constants are represented by α' and α'', but the constants C_{2n} and μ are dependent only on the values of a and q and not on the initial conditions. A necessary condition for stability (ie: u remains finite as ζ approaches infinity) is that $\alpha = 0$. Then Eq. 2.20 becomes:

$$u(\zeta) = \alpha' \sum_{n=-\infty}^{n=\infty} C_{2n} e^{(2n\pm\beta)i\zeta} + \alpha'' \sum_{n=-\infty}^{n=\infty} C_{2n} e^{-(2n\pm\beta)i\zeta}. \tag{2.21}$$

Even though $\alpha = 0$ is a necessary condition for stability, not all values of β yield stable solutions. In fact, stable solutions only result when β is not an integer. The integer values of β form the boundaries between stable and non-stable areas on the stability diagram as shown in Fig. 2.3. The lowest zone of stability (bounded by $\beta = 0$ and $\beta = 1$) is generally the only zone considered due to the geometrical constraints of the standard quadrupole spectrometers.

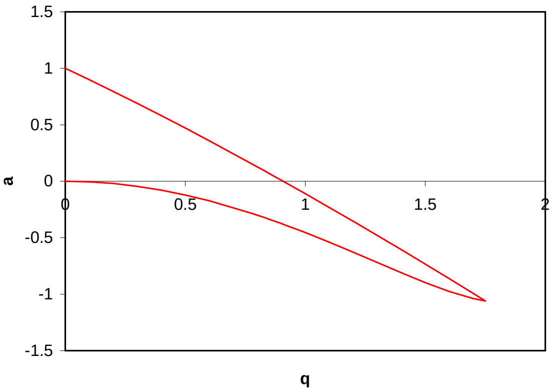

Figure 2.3: An approximate a-q stability diagram for the Mathieu equation for only one coordinate direction. Only the lowest zone of stability is shown, where values of a and q within the two lines produce stable ion trajectories for the particular coordinate.

Upon further examination of Eq. 2.21, one can see that the ion motions will have a frequency term of $(2n \pm \beta)\zeta$. With $\zeta = \omega t/2$, then, the frequency of motion, ω_n can be described by:

$$\omega_n = \frac{(2n \pm \beta)\omega}{2}. \tag{2.22}$$

Thus, the resulting motion of ions will generally have a low-frequency secular motion and a higher frequency micromotion as a result of Eq. 2.22, with the amplitudes of motion depending on the C_{2n} values, and thus on a and q.

For practical reasons, circular rods are often substituted for the hyperbolic cylinders. The radius of the rods is chosen to closely approximate the quadrupole potential given by Eq. 2.9. Empirical evidence from Ref. [24] showed a rod radius, $r = 1.148r_o$ provided the best approximation to the potential provided by hyperbolic cylinders. Semi-analytical calculations from Ref. [25] are comparable and suggest a rod radius, $r = 1.14511r_o$. Independent calculations published in Ref. [26] agree, and show that a refined rod radius of $1.1468r_o$ has little effect on the performance of the mass filter. However, subsequent analysis by Ref. [27] many years later disagreed with the method used by Ref. [26] and found the stability diagram, and hence the mass resolution achievable, for circular rods is affected unfavourably as compared with hyperbolic cylinders. Regardless, the quadrupole potential formed by hyperbolic cylinders can be approximated with circular rods with radii $\sim 1.146r_o$. The performance of the mass filter may be compromised, but if high mass resolution is not the objective, then circular rods provide a practical alternative.

Up to now, only a sinusoidal alternating potential has been considered. However, there is no reason not to try an alternating square-wave potential instead. Equation 2.35a becomes:

$$\frac{d^2r}{d\zeta^2} + (a_r + 2q_r)r = 0 \tag{2.23}$$

for $0 < \zeta < \theta$ and:

$$\frac{d^2r}{d\zeta^2} + (a_r - 2q_r)r = 0 \tag{2.24}$$

for $\theta < \zeta < \pi$ with similar equations for z. The above equations are forms of the Meissner equations which yield similar stability diagrams as the Mathieu equations. Of special mention is the fact that a departure of θ from $\pi/2$ is equivalent to the application of a mean DC potential, which results in greater mass resolution.

Three dimensional confinement

The previous discussion of two dimensional confinement where the ion motion is restricted in two dimensions can be extended to three dimensions. The practical application of two dimensional confinement is a mass filter where only ions of a selected mass pass through the length of the structure. In an ion trap, however, no ions pass through the structure. Instead, ions of a certain mass are confined while the others are lost to the trap.

The requirement for suspending ions in all three dimensions is a potential of the form:

$$V = \lambda_x x^2 + \lambda_y y^2 + \lambda_z z^2. \tag{2.25}$$

The solution to Laplace's equation, therefore, demands:

$$\lambda_x + \lambda_y + \lambda_z = 0, \tag{2.26}$$

in analogy to Eq. 2.7. Once again, the trivial solution ($\lambda_x = \lambda_y = \lambda_z = 0$) does not generate the required restoring force; whereas, a solution of the type:

$$\lambda_x = \lambda_y = -\left(\frac{1}{2}\right)\lambda_z \tag{2.27}$$

does. The potential resulting from this condition, with the caveat $\lambda = 1/2\lambda_z$, is of the form:

$$V = -\lambda(x^2 + y^2 - 2z^2), \tag{2.28}$$

or, in cylindrical coordinates:

$$V = -\lambda(r^2 - 2z^2). \tag{2.29}$$

With $\frac{\varphi_o}{2}$ being the magnitude of the electric potential at coordinates $(r, z) = (\pm r_o, 0)$, then $\lambda = -\frac{\varphi_o}{2r_o^2}$ which necessitates electrodes satisfying:

$$\frac{r^2}{r_o^2} - \frac{2z^2}{r_o^2} = 1 \tag{2.30a}$$

at potential $\frac{\varphi_o}{2}$ and

$$\frac{r^2}{r_o^2} - \frac{2z^2}{r_o^2} = -1 \tag{2.30b}$$

at potential $-\frac{\varphi_o}{2}$ to satisfy Eq. 2.29. The surfaces so created should be familiar (see Eq. 2.10). The structure formed is shown in Fig. 2.4. It consists of two endcap electrodes (satisfying Eq. 2.30b) which describe hyperboloids of revolution, and an intermediate ring electrode (from Eq. 2.30a) of hyperbolic cross-section. With r_o as the inner radius of the ring electrode, the distance between the endcap electrodes is $2z_o$ with the dimensional constraint $(r_o/z_o)^2 = 2$.

The potential inside the trap is quadrupole in nature. A voltage U_{dc} applied between the ring and endcaps will therefore confine the ions either radially or azimuthally, depending upon the sign of U_{dc}. To confine the ions in both directions, an alternating potential is required. The potential inside the trap V can then be expressed as:

$$V = \varphi_o\left(\frac{r^2 - 2z^2}{2r_o^2}\right) \tag{2.31}$$

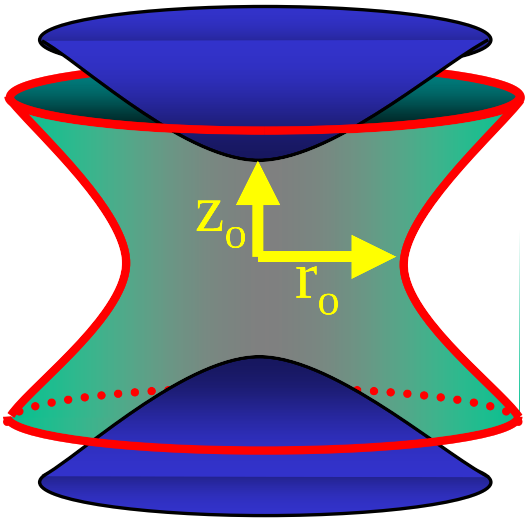

Figure 2.4: The three electrode structure of the ion trap (not to scale). An intermediate ring electrode (in green), which is transparent in the picture, is surrounded by two endcap electrodes (in blue).

with $\varphi_o = U_{dc} - V_{rf}\cos(\omega t)$. The resulting electric field can then be determined:

$$\vec{E} = -\vec{\nabla}\Phi = -\frac{U_{dc} - V_{rf}\cos(\omega t)}{2r_o^2}(2r\hat{r} - 4z\hat{z}). \tag{2.32}$$

Solving $\vec{F} = m\vec{a} = q\vec{E}$ produces the equations of motion:

$$m(\ddot{r} - r\dot{\phi}^2) = -\frac{q}{r_o^2}[U_{dc} - V_{rf}\cos(\omega t)]r \tag{2.33a}$$

$$m(2\dot{r}\dot{\phi} + r\ddot{\phi}) = 0 \tag{2.33b}$$

$$m\ddot{z} = \frac{2q}{r_o^2}[U_{dc} - V_{rf}\cos(\omega t)]z. \tag{2.33c}$$

Integration of Eq. 2.33b yields $mr^2\frac{d\phi}{dt}$ = constant, the equation which expresses conservation of angular momentum. As ions are injected into the trap with essentially only axial energy and no angular energy, the assumption $\frac{d\phi}{dt} = 0$ for all time is an appropriate approximation. Therefore, with $\dot{\phi}$=$\ddot{\phi}$=0, the above equations are simplified into two equations:

$$\ddot{r} + \frac{q}{mr_o^2}\,[U_{dc} - V_{rf}\cos(\omega t)]r = 0 \tag{2.34a}$$

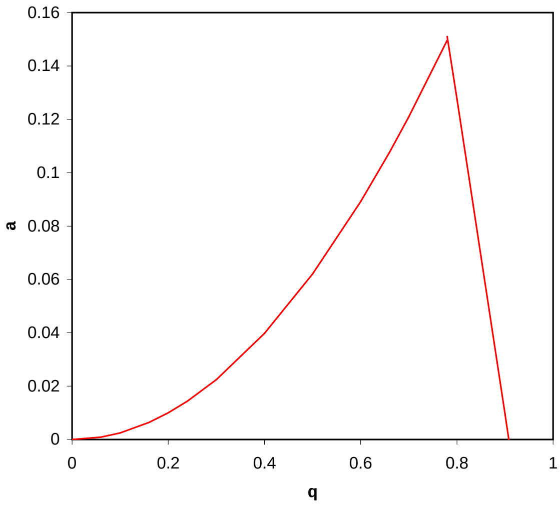

Figure 2.5: The a-q stability diagram for the Mathieu equation with both $\hat{r}$ and $\hat{z}$ coordinates considered. Within the two lines are the smallest, positive values of a and q for which ion trajectories are stable.

$$\ddot{z} - \frac{2q}{mr_o^2}\left[U_{dc} - V_{rf}\cos(\omega t)\right]z = 0. \tag{2.34b}$$

With the substitution $\zeta = \omega t/2$ as before, the above equations which represent the ion motion in a Paul trap become the Mathieu differential equations described by:

$$\frac{d^2r}{d\zeta^2} + (a_r - 2q_r\cos(2\zeta))r = 0 \tag{2.35a}$$

$$\frac{d^2z}{d\zeta^2} + (a_z - 2q_z\cos(2\zeta))z = 0 \tag{2.35b}$$

which yield stable solutions only for certain values of a's and q's where:

$$a_z = -2a_r = -\frac{8qU}{mr_o^2\omega^2} \tag{2.36a}$$

$$q_z = -2q_r = -\frac{4qV}{mr_o^2\omega^2}. \tag{2.36b}$$

A "stability" diagram for each coordinate can be generated by making a graph of a versus q. If the stability diagrams for all coordinates are superimposed, as has been done in generating Fig. 2.5, stable solutions are those (a,q) pairs which are common to all diagrams. Generally, one can choose the range of masses that are captured by carefully selecting values for a and q. However, if mass resolution is not the primary goal, then it is easier to set the DC potential U_{dc} to zero. Thus, with $a = 0$, values of q between 0 and 0.908 will yield stable solutions. For a given q, then, the trapping of a different mass requires the coincident change in the applied frequency as $\omega \propto \frac{1}{\sqrt{m}}$.

2.1.2 Buffer gas cooling

The discussion of radio-frequency quadrupole (RFQ) devices until now has assumed the residual pressure within the structure is negligible, but with the introduction of a buffer gas, such as helium, ions travelling through a quadrupole mass filter or confined within a Paul trap can be cooled. The energy loss mechanism results from the interactions of the ions with the induced dipole moment of the buffer gas atoms. Therefore the energy space which describes the ions entering such devices can be reduced to the temperature of the buffer gas.

For ions of low velocity, the effect of interactions with the buffer gas can be described in terms of a viscous drag force, F_d, which is proportional to the velocity of the ion as seen by the following:

$$\vec{F_d} = -\frac{q}{K}\vec{v}, \tag{2.37}$$

where q is the charge state of the ion and K is the mobility of the ion in the specific buffer gas used. The ion mobility is a measure of the drift velocity v_d in the direction of an externally applied electric field, E, such that:

$$\vec{v_d} = K\vec{E}. \tag{2.38}$$

Intuitively, the ion mobility should depend on the gas density since the drift velocity of the ions will depend upon the time between collisions with the buffer gas, and as the time between collisions is inversely proportional to the gas density, so will be the ion mobility. Indeed, ion mobilities can be scaled from standard temperature and pressure conditions (stp) by noting [28]:

$$K_o = K\frac{p}{p_{stp}}\frac{T_{stp}}{T}. \tag{2.39}$$

Many values for this normalized form of the ion mobility are tabulated in Ref. [29].

The introduction of a buffer gas modifies the equations of motion. Take the mass filter for instance. Equation 2.16 is adjusted for the drag force expressed in Eq. 2.37:

$$\ddot{x} + \frac{q}{mK}\dot{x} + \frac{q}{mr_o^2}\{U_{dc} - V_{rf}\cos[\omega_{rf}(t - t_o)]\}x = 0 \tag{2.40a}$$

$$\ddot{y} + \frac{q}{mK}\dot{y} - \frac{q}{mr_o^2}\{U_{dc} - V_{rf}\cos[\omega_{rf}(t - t_o)]\}y = 0 \tag{2.40b}$$

$$\ddot{z} + \frac{q}{mK}\dot{z} - qE = 0. \tag{2.40c}$$

The latter equation arises from the additional electric field used to guide the ions along the mass filter and remains independent of the transverse motion. The other two equations, however, remain coupled and the solutions become complex versions of the regular Mathieu equations [23]. This situation is analogous to the complex solutions which describe damped simple harmonic motion. In summary, the net effect of this additional drag is a mass selective filter with collisional cooling.

2.2 Penning traps

The Paul trap is an excellent tool for confining ions to a small region of space. Although it can be used as a crude mass spectrometer if appropriate values of the parameters a and q as defined by Eq. 2.36 are selected, precise measurements are difficult to obtain due to the unavailability of precision voltage sources. Superconducting magnets, on the other hand, do produce extremely uniform and stable *magnetic* fields. Precise mass spectrometry can therefore be performed by determining the cyclotron frequency of ions within such a magnetic field using a different type of ion trap, the Penning trap.

2.2.1 Ion confinement

An ion of mass m, subjected only to a homogeneous magnetic field of magnitude B, undergoes cyclotron motion, at frequency:

$$\omega_c = \frac{qB}{m}, \tag{2.41}$$

where q is the charge of the ion. In this manner, the ions are confined radially but are free to escape along the axis of the magnetic field. The addition of an axially harmonic potential of magnitude V provides axial confinement. The derivation of the electrode structure is similar to that of the Paul trap. With a potential of the form given by Eq. 2.29, a potential difference of V_o as defined by:

$$V_o = V(r = 0, z_o) - V(r_o, z = 0) = \lambda(2z_o^2 + r_o^2) \tag{2.42}$$

determines the constant λ:

$$\lambda = \frac{V_o}{2z_o^2 + r_o^2}. \tag{2.43}$$

In most literature, the potential within the Penning trap is expressed as:

$$V = \frac{V_o}{2d^2}\left(z^2 - \frac{r^2}{2}\right), \tag{2.44}$$

where, from Eq. 2.43,

$$d = \sqrt{\frac{1}{2}\left(z_o^2 + \frac{r_o^2}{2}\right)} \tag{2.45}$$

and is referred to as the characteristic trap dimension. The axial harmonic potential can therefore be produced by three electrodes along equipotential surfaces: two endcap electrodes defined by:

$$1 = \left(\frac{z}{z_o}\right)^2 - \left(\frac{r}{\sqrt{2}z_o}\right)^2 \tag{2.46}$$

which describe hyperboloids of revolution and an intermediate ring electrode:

$$-1 = \left(\frac{z}{r_o/\sqrt{2}}\right)^2 - \left(\frac{r}{r_o}\right)^2 \tag{2.47}$$

which has a hyperbolic cross section. V_o therefore represents the difference in potential between the endcap electrode and ring electrode. With the superposition of the magnetic and electric fields so described, ions within a Penning trap are confined, or trapped, in free space.

2.2.2 Ion motion

As the motion of ions in a Penning trap is described in detail in Ref. [30], only a synopsis is provided here. The intent of the following discussion is to give a basic understanding of the ion motion within a Penning trap which will provide the framework for further discussion relevant to this work.

The electric field $\vec{E}$ produced by the quadrupole potential defined by Eq. 2.44 can be described in cartesian coordinates as:

$$\vec{E} = -\vec{\nabla} V = \frac{V_o}{2d^2}(x\hat{x} + y\hat{y} - 2z\hat{z}). \tag{2.48}$$

The equations of motion are obtained by solving for the Lorentz force:

$$\vec{F} = m\vec{a} = q(\vec{E} + \vec{v} \times \vec{B}). \tag{2.49}$$

With position vector $\vec{R} = x\hat{x} + y\hat{y} + z\hat{z}$, Eq. 2.49 becomes:

$$m(\ddot{x}\hat{x} + \ddot{y}\hat{y} + \ddot{z}\hat{z}) = q\{(\frac{V_o}{2d^2})(x\hat{x} + y\hat{y} - 2z\hat{z}) + B(\dot{y}\hat{x} - \dot{x}\hat{y})\}, \tag{2.50}$$

in which an analytical solution requires the simultaneous solving of the following three differential equations:

$$\ddot{x} = \frac{qV_o}{2md^2}x + \frac{qB}{m}\dot{y} \tag{2.51a}$$

$$\ddot{y} = \frac{qV_o}{2md^2}y - \frac{qB}{m}\dot{x} \tag{2.51b}$$

$$\ddot{z} = -\frac{qV_o}{md^2}z. \tag{2.51c}$$

Equation 2.51c is decoupled from the others and expresses the axial motion of the ions as simple harmonic motion with frequency:

$$\omega_z = \sqrt{\frac{qV_o}{md^2}}. \tag{2.52}$$

With the substitutions of Eq. 2.52 and Eq. 2.41, Eqs. 2.51 become:

$$\ddot{x} = \frac{\omega_z^2}{2}x + \omega_c\dot{y} \tag{2.53a}$$

$$\ddot{y} = \frac{\omega_z^2}{2} y - \omega_c \dot{x} \tag{2.53b}$$

$$\ddot{z} = -\omega_z^2 z. \tag{2.53c}$$

The first two equations can be reduced to one equation with the substitution $u = x + iy$:

$$\ddot{u} + i\omega_c \dot{u} - \frac{\omega_z^2}{2} u = 0, \tag{2.54}$$

where the solution requires a solution to both the real and imaginary parts. Now with the introduction of the differential operator $D = d/dt$, Eq. 2.54 becomes:

$$[D^2 + i\omega_c D - \frac{\omega_z^2}{2}] u = 0. \tag{2.55}$$

The solution to the quadratic equation is:

$$D = \frac{-i\omega_c \pm i\sqrt{\omega_c^2 - 2\omega_z^2}}{2} \tag{2.56}$$

and therefore, with the substitution:

$$\omega_+ = \frac{\omega_c}{2}\left(1 + \sqrt{1 - 2\frac{\omega_z^2}{\omega_c^2}}\right); \quad \omega_- = \frac{\omega_c}{2}\left(1 - \sqrt{1 - 2\frac{\omega_z^2}{\omega_c^2}}\right), \tag{2.57}$$

Eq. 2.55 can be transformed into:

$$[D + i\omega_+][D + i\omega_-] u = 0. \tag{2.58}$$

Note the frequency relations:

$$\omega_+ \omega_- = \frac{\omega_z^2}{2} \tag{2.59}$$

and

$$\omega_+ + \omega_- = \omega_c \tag{2.60}$$

which can be obtained by comparing Eq. 2.58 and Eq. 2.55. The latter equation is important since a measurement of the sum of the two radial eigenfrequencies of motion is equivalent to a determination of the cyclotron frequency which, in turn, can be used to obtain precise mass measurements. The procedure used to extract the cyclotron frequency is the subject of Section 2.2.3.

Each factor in Eq. 2.58 represents a first-order differential equation:

$$[D + i\omega_\pm]u = \frac{du}{dt} + i\omega_\pm u = 0 \tag{2.61}$$

which has a solution:

$$u = u_\pm e^{-i\omega_\pm t}. \tag{2.62}$$

The general solution will therefore consist of the sum of both of these solutions:

$$u = u_+ e^{-i\omega_+ t} + u_- e^{-i\omega_- t}. \tag{2.63}$$

Once this has been transformed back into cartesian coordinates:

$$x = r_+ \cos(\omega_+ t - \phi_+) + r_- \cos(\omega_- t - \phi_-) \tag{2.64a}$$

$$y = -r_+ \sin(\omega_+ t - \phi_+) - r_- \sin(\omega_- t - \phi_-) \tag{2.64b}$$

with the relation $u_\pm = r_\pm e^{i\phi_\pm}$.

An ion confined in the Penning trap therefore undergoes three eigenfrequencies of motion. One is the axial harmonic motion at frequency ω_z. The resulting electric field in the radial direction, combined with the magnetic field, causes the original cyclotron motion to be split into two other eigenfrequencies of radial motion, ω_+ (reduced cyclotron frequency) and ω_- (magnetron frequency), related to ω_c by their sum. Since ω_c depends only on the constant magnetic field of the trap, precise mass measurements can be obtained by a determination of the cyclotron frequency. However, since the cyclotron frequency is not a natural motion of ions confined in a Penning trap, the trick is to find some way of obtaining it. Equation 2.60 provides a hint.

2.2.3 Driving the ion motion

Since ω_c is not an eigenfrequency of motion, it needs to be determined by alternate methods. To allow this, the ring electrode of the Penning trap is divided into four quadrants to enable the application of azimuthally oscillating dipole or quadrupole potentials superimposed on the static trapping potentials.

Dipole excitation

An azimuthal time-varying potential described by:

$$\Phi_d = U_d \cos(\omega_d t - \phi_d) x \tag{2.65}$$

provides a dipole field:

$$\vec{E} = -\vec{\nabla}\Phi_d = -U_d \cos(\omega_d t - \phi_d)\hat{x}, \tag{2.66}$$

where ω_d and ϕ_d are the frequency and phase of the applied sinusoidal waveform. With Eq. 2.54 modified to account for the addition of the dipole field:

$$\ddot{u} + i\omega_c \dot{u} - \frac{\omega_z^2}{2} u = -k_d \cos(\omega_d t - \phi_d) \tag{2.67}$$

where

$$k_d = \frac{q}{m} U_d. \tag{2.68}$$

The solutions to the radial equations of motion can be found to be:

$$x = \rho_-(t)\cos(\omega_- t - \phi_-) + \rho_+(t)\cos(\omega_+ t - \phi_+) \tag{2.69a}$$

$$y = -\rho_-(t)\sin(\omega_- t - \phi_-) - \rho_+(t)\sin(\omega_+ t - \phi_+) \tag{2.69b}$$

where now the amplitudes of motion are time varying functions as opposed to the scenario when no radio-frequency field was applied. (Compare with Eq. 2.64).

Ions subjected to a dipole excitation absorb energy resonantly when the driving frequency $\omega_d = \omega_+$ or ω_-. In this situation, and with the additional assumption that the phase shift $(\phi_d - \phi_\pm)$ corresponds to $3\pi/2$ for excitations at ω_+ and $\pi/2$ for excitations at ω_-, the time varying amplitudes simplify to:

$$\rho_\pm(t) = \rho_\pm(0) + \frac{k_o}{2(\omega_+ - \omega_-)}\, t \tag{2.70}$$

which depends upon the amplitude of the driving field, $U_{d'}$, and the duration of the excitation. The ω_+ excitation is highly mass selective and can be used to remove unwanted isotopes by increasing the radius of the ions' orbit until they are lost from the trap. The ω_- is only weakly dependent on the mass of the ion and is used to establish the initial orbital radius for the desired ions.

Quadrupole excitation

An azimuthal potential described by:

$$\Phi_q = -\frac{V_{rf}}{2a^2}\cos(\omega_q t - \phi_q)(xy) \tag{2.71}$$

provides a quadrupole field:

$$\vec{E} = \frac{V_{rf}}{2a^2}\cos(\omega_q t - \phi_q)(y\hat{x} + x\hat{y}) \tag{2.72}$$

with ω_q and ϕ_q representing the frequency and phase of the applied sinusoidal waveform. Once again, the form of Eq. 2.54 remains essentially the same except for the inclusion of the applied quadrupole field and the solutions to the radial equations of motion have the same general form as given in Eq. 2.69, but now the time-varying amplitudes are more complicated. If $\rho^o_\pm$ symbolizes the initial radius of the reduced cyclotron (+) and magnetron (-) motion, then from Ref. [31], the radius at some time t later is given by:

$$\rho_\pm(t) = \left\{\rho^o_\pm \cos(\omega_B t) \mp \frac{1}{2}\frac{\rho^o_\pm[i(\omega_{rf} - \omega_c)] + \rho^o_\mp k^o_\pm}{\omega_B}\sin(\omega_B t)\right\} e^{[i\frac{1}{2}(\omega_{rf}-\omega_c)t]} \tag{2.73}$$

with:

$$\omega_B = \frac{1}{2}\sqrt{(\omega_{rf} - \omega_c)^2 + (k_o)^2} \tag{2.74}$$

and

$$k^o_\pm = k_o e^{\pm i\Delta\phi} = \left(\frac{V_{rf}}{2a^2}\frac{q}{m}\frac{1}{\omega_+ - \omega_-}\right) e^{\pm i\Delta\phi}, \tag{2.75}$$

where the term in brackets is the expression for k_o. The total radial kinetic energy, E_r, gained by the trapped ions depends upon both the magnetron and reduced cyclotron motion such that:

$$E_r = \frac{1}{2}m[(\rho_+\omega_+)^2 + (\rho_-\omega_-)^2]. \tag{2.76}$$

If the ions are prepared to have no initial reduced cyclotron motion, ie: $\rho^o_+ = 0$, then with $\rho^o_- \equiv \rho_o$:

$$\rho^2_+(t) = \frac{1}{4}(\rho_o)^2(k^o_+)^2\ \frac{\sin^2(\omega_B t)}{\omega^2_B}. \tag{2.77}$$

Similarly, under the same initial conditions,

$$\rho_{-}^{2}(t) = (\rho_o)^2 \left[\cos^2(\omega_B t) + \frac{1}{4}(\omega_{rf} - \omega_c)^2 \, \frac{\sin^2(\omega_B t)}{\omega_B^2}\right]. \tag{2.78}$$

Therefore, with Eqs. 2.77 and 2.78 substituted into Eq. 2.76,

$$E_r = \frac{1}{2}m\left\{\frac{1}{4}(\rho_o)^2(k_o)^2\omega_{+}^{2} \, \frac{\sin^2(\omega_B t)}{\omega_B^2} + (\rho_o)^2\omega_{-}^{2}\left[\cos^2(\omega_B t) + \frac{1}{4}(\omega_{rf} - \omega_c)^2 \, \frac{\sin^2(\omega_B t)}{\omega_B^2}\right]\right\} \tag{2.79}$$

in which the identity $(k_{+}^{o})^2 = (k_{+}^{o})^*(k_{+}^{o}) = k_o^2$ obtained from Eq. 2.75 was used.

Note what happens if the excitation frequency is equal to the cyclotron frequency. Then, with $\omega_B = \frac{1}{2}k_o$, Eq. 2.79 becomes:

$$E_r = \frac{1}{2}m(\rho_o)^2\left\{\omega_{+}^{2}\sin^2\left(\frac{1}{2}k_o t\right) + \omega_{-}^{2}\cos^2\left(\frac{1}{2}k_o t\right)\right\}. \tag{2.80}$$

Therefore, under the assumed condition that the initial radial motion of the ions confined in the Penning trap is only that of magnetron motion, then from Eq. 2.80 this initial motion is converted completely into a reduced cyclotron motion when:

$$\frac{1}{2}k_o t = \frac{\pi}{2}. \tag{2.81}$$

Shown in Fig. 2.6 is an example of the energy gain profile resulting from a full conversion between the magnetron and reduced cyclotron motions. If we denote the "conversion" time as t_{conv}, then the condition given by Eq. 2.81 can be expressed as:

$$t_{conv} = \frac{\pi}{k_o} = \pi\left(\frac{2a^2}{V_{rf}}\frac{m}{q}\right)(\omega_{+} - \omega_{-}). \tag{2.82}$$

Since $\omega_{-} \ll \omega_{+} \approx \omega_c$, the above expression can be approximated as:

$$t_{conv} = \frac{\pi}{k_o} = \pi\frac{2a^2B}{V_{rf}}. \tag{2.83}$$

Thus, a longer conversion time is possible with a coincident reduction in the applied RF voltage. Is there an advantage to do this? The short answer is yes. The longer answer follows.

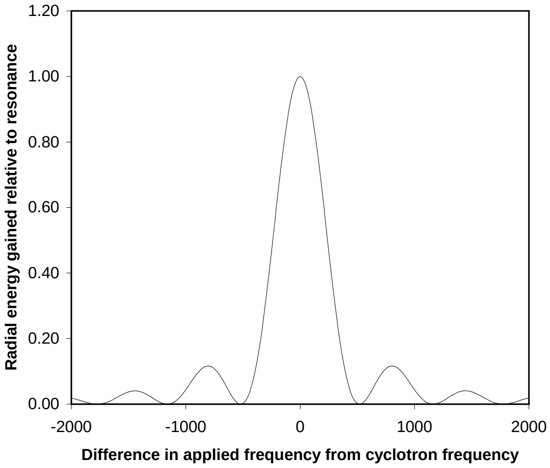

Figure 2.6: An example of the energy gain profile is shown and assumes a complete conversion from an initially pure magnetron motion to a reduced cyclotron motion. The plotted energy is normalized to the energy gained when the ions are driven resonantly at the cyclotron frequency.

Under the assumption that $\omega_+ \gg \omega_-$, then Eq. 2.79 can be reexpressed as:

$$E_r \sim \frac{1}{8} m(\rho_o)^2 (k_o)^2 \omega_+^2 \; \frac{\sin^2(\omega_B t)}{\omega_B^2}. \tag{2.84}$$

Furthermore, if the conversion time given above is used, then:

$$E_r \sim \frac{1}{8} m(\rho_o)^2 \pi^2 \omega_+^2 \; \frac{\sin^2\left(\frac{\omega_B \pi}{k_o}\right)}{\left(\frac{\omega_B \pi}{k_o}\right)^2}. \tag{2.85}$$

Given a spectrum of the energy versus the applied frequency of the quadrupole field, the resolution of this spectrum is a comparison of the full frequency width at half the maximum energy amplitude (FWHM). The FWHM is easily found from the frequency positions at half the full energy amplitude. At these positions, $\omega_{rf} = \omega_c \pm w/2$ where w represents the FWHM. If $\omega_B|_h$ is the value for ω_B at the half maximum positions:

$$\frac{\frac{1}{2}E_r}{E_r} = \frac{\frac{\sin^2(\omega_B|_h \frac{\pi}{k_o})}{\omega_B|_h^2 (\frac{\pi}{k_o})^2}}{\frac{\sin^2(\omega_B \frac{\pi}{k_o})}{\omega_B^2 (\frac{\pi}{k_o})^2}}. \tag{2.86}$$

Since $\omega_B = \frac{1}{2}k_o$ at resonance (ie: when $\omega_{rf} = \omega_c$), then the above equation becomes:

$$\frac{1}{2} = \frac{\frac{\sin^2(\omega_B|_h \frac{\pi}{k_o})}{\omega_B|_h^2 (\frac{\pi}{k_o})^2}}{\frac{1}{(\frac{\pi}{2})^2}}. \tag{2.87}$$

The solution is therefore:

$$\omega_B|_h \frac{\pi}{k_o} = \frac{1}{2}\pi\sqrt{\left(\frac{w}{2k_o}\right)^2 + 1} \simeq 2.01 \ . \tag{2.88}$$

With the substitution $k_o = \pi/t_{conv}$:

$$w \simeq \frac{0.8}{t_{conv}}\text{Hz}. \tag{2.89}$$

In summary, if the initial reduced cyclotron motion is assumed to be negligible, the energy spectrum generated from a frequency scan about the cyclotron frequency has a FWHM which is inversely proportional to the conversion time; however, this is only true if a full conversion from the magnetron motion to reduced cyclotron motion is achieved at the resonant cyclotron frequency. A higher resolution can therefore be achieved if the ions in the trap are subjected to longer excitations of the quadrupole field with appropriate amplitude. (See Eq. 2.83.) Since the energy gain at the resonant cyclotron frequency is significant and a high resolution is possible, precise mass measurements are conceivable. The method to measure the energy gain is discussed in the next section.

2.2.4 The TOF effect

The effect of resonantly exciting the trapped ions at their eigenfrequencies is now clear – the ions gain radial energy. This section will describe the method used to detect the energy gain and determine empirically the values for the eigenfrequencies.

Once the ions in the Penning trap have been exposed to an azimuthal dipole or quadrupole field at a particular frequency, the ions can be characterized by their magnetic moment, $\vec{\mu}$, where:

$$\vec{\mu}(\omega_{rf}) = \frac{E(\omega_{rf})}{B_o}\hat{z}, \tag{2.90}$$

with $E(\omega_{rf})$ representing the radial energy gained during the excitation and B_o is the value of the magnetic field within the volume occupied by the trapped ions.

After the ions are ejected from the Penning trap, the magnetic moment of the ions interacts with the magnetic field gradient outside the trap which results in a force in the longitudinal direction as demonstrated:

$$\vec{F} = -\vec{\nabla}(\vec{\mu}(\omega_{rf}) \cdot \vec{B}) \Rightarrow -\mu(\omega_{rf})\frac{\partial B}{\partial z}\hat{z}. \tag{2.91}$$

The effect of the interaction is to convert the radial energy gained from the excitation to longitudinal energy. The measurement of this effect is performed using the established time-of-flight (TOF) technique [32] in which a multichannel scaler records the amount of time it takes for the ions to reach a microchannel plate (MCP) detector after they are ejected from the Penning trap. The time to arrive at the detector at a position z from the trap center at z_o can be determined with:

$$t(\omega_{RF}) = \int_{z_o}^{z} \sqrt{\frac{m}{2(E_o - qV(z) - \mu(\omega_{rf})B(z))}}\, dz \tag{2.92}$$

which includes the initial axial energy of the ions while in the Penning trap, E_o, and the longitudinal energy gained by the ions while they travel through the electrostatic potential of the drift tube electrodes that guide the ions to the detector.

The time-of-flight technique is a destructive one; each measurement cycle requires a new ion bunch. To determine the frequency at which the ions gain the most energy, each ion bunch is subjected to a slightly different excitation frequency. Since the radial energy gained from the excitation is converted into axial energy, those ions which have gained radial energy at the resonant frequency reach the detector sooner than ions which have been exposed to other excitation frequencies. Therefore, with the average arrival time of the ions at the MCP detector plotted as a function of the excitation frequency (as shown in Fig. 2.7), the resonant frequency is obtained by determining the minimum in the spectrum. In the case of a dipole excitation, the resonant frequency corresponds to the reduced cyclotron motion of an ion species. (A dipole excitation at the magnetron frequency does not impart sufficient energy to observe a noticeable minimum in the time-of-flight spectra). When an azimuthal

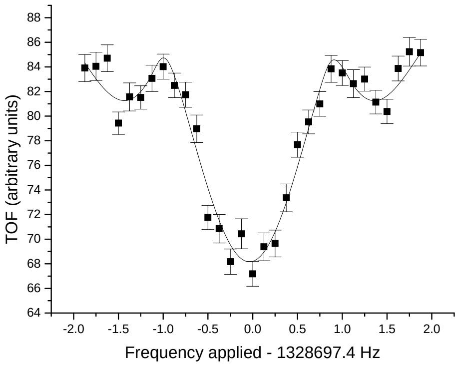

Figure 2.7: Time-of-flight spectra. Plotted is the average arrival time of the ions at the MCP detector as a function of the excitation frequency. Sample data is shown along with the expected lineshape.

quadrupole field excitation is applied, the minimum in the time-of-flight spectra corresponds to the true cyclotron frequency.

2.2.5 Effect of introducing a buffer gas

The introduction of a buffer gas into a Penning trap can result in a mass selective cooling process. The description is similar to that of a buffer gas in the Paul trap (see Section 2.1.2) such that a viscous drag force, $\vec{F_d} = -\delta \cdot m \cdot \vec{v}$, is added to the equations of motion with:

$$\delta = \frac{q}{m}\frac{1}{K}. \tag{2.93}$$

The resulting equations of motion are somewhat complicated, and a rigorous derivation can be seen in Ref. [31].

With only the static electric and magnetic fields used to confine the ions in the Penning trap, the amplitudes of the radial magnetron motion (ρ_+) and reduced cyclotron motion (ρ_-) are affected by the buffer gas such that:

$$\rho^{\pm}(t) = \rho^{\pm}(0)\mathrm{e}^{\alpha_{\pm} t} \tag{2.94}$$

where:

$$\alpha_{\pm} = \mp\delta\frac{\omega_{\pm}}{\omega_{+} - \omega_{-}}. \tag{2.95}$$

Therefore, with the presence of a buffer gas and the absence of any driving electric field, the amplitude of the reduced cyclotron motion decreases while the amplitude of the magnetron motion increases.

The application of an azimuthal quadrupole field couples the magnetron and reduced cyclotron motions, despite the presence of a buffer gas. However, the cooling of the ion motions results in a different effect. If, for example, all ions in the trap have only magnetron motion initially, the application of the quadrupole field can completely convert the magnetron motion of a selected ion species to the reduced cyclotron motion. These ions are then recentered from collisional cooling with the buffer gas, while the orbital radius of all remaining ions continues to grow. The result is a mass selective cooling process which can be used to remove contaminant ions quickly and efficiently.

Recentering the desired ion species as quickly as possible while simultaneously achieving high mass resolution corresponds to $k_o = \frac{\delta}{\omega_+ - \omega_-}\, \omega_c$ [31]. This, in turn, requires a quadrupole field excitation with an amplitude:

$$V_{rf} \approx 2a^2 \delta B. \tag{2.96}$$

The presence of a buffer gas in the Penning trap can therefore be used to remove contaminant ions. Higher mass resolution can be achieved with lower buffer gas pressures, but only at the expense of longer cooling times.

2.2.6 Methods to characterize Penning trap performance

To characterize the performance of the Penning trap mass spectrometer, a quantitative description is necessary. In this section, three of these quantities will be provided, namely the resolving power P, the resolution R, and the mass precision, $\delta m/m$.

The resolving power of a Penning trap mass spectrometer is defined as the ability to differentiate masses. Mathematically, this definition is described as:

$$P = \frac{m}{\Delta m} \tag{2.97}$$

where Δm is equivalent to the line width (FWHM). Similarly, the term resolution is also used to describe the capability of the mass instrument in resolving masses and is equal to the inverse of the resolving power such that:

$$R = \frac{\Delta m}{m}. \tag{2.98}$$

For Penning trap mass spectrometers which determine the mass of the trapped ions through a measurement of their cyclotron frequency, the mass precision is easily obtained with Eq. 2.41. Under the assumptions that the charge state and strength of the magnetic field are well known, the relative uncertainty in the mass:

$$\frac{\delta m}{m} = \frac{\delta \omega_c}{\omega_c} \tag{2.99}$$

depends upon the precision of the cyclotron frequency measurement. For each mass measurement, the underlying physics motivation dictates the mass precision required, which in turn, determines how well the cyclotron frequency must be measured.

Chapter 3

Apparatus

Precise mass measurements made with the CPT require sufficient yields of low-energy ions with minimal contamination. Since the objective of the CPT is to make measurements of short-lived, rare isotopes, the injection system must be efficient and take minimal time in preparing the ion samples. The CPT apparatus at ANL consists of a variety of devices to meet these requirements. First, a brief description of the entire apparatus as shown in Fig. 3.1 is provided.

To study the astrophysical rp-process, desired nuclides are created in fusion-evaporation reactions between targets on a rotating wheel and heavy-ion beams from the ATLAS facility at ANL. The nuclides produced in the reaction are focused and separated from the primary beam with a combination of a magnetic triplet, a velocity filter, and an Enge split-pole magnetic spectrograph [33]. A degrader, positioned at the focal plane of the spectrograph, reduces the energy of the ions before they enter a gas catcher [34] where the ions are thermalized with helium gas. The ions are extracted from the gas catcher via a combination of gas flow and electric fields and are guided through an ion cooler towards an isotope separator as the helium is pumped away. Before entering the isotope separator, the ions are accumulated within a small trapping potential and are periodically ejected, converting the continuous ion beam into a pulsed ion beam. The ion bunches are then captured in the isotope separator, a gas-filled Penning trap ($B \sim 1$ T), where they are subjected to a mass selective cool-

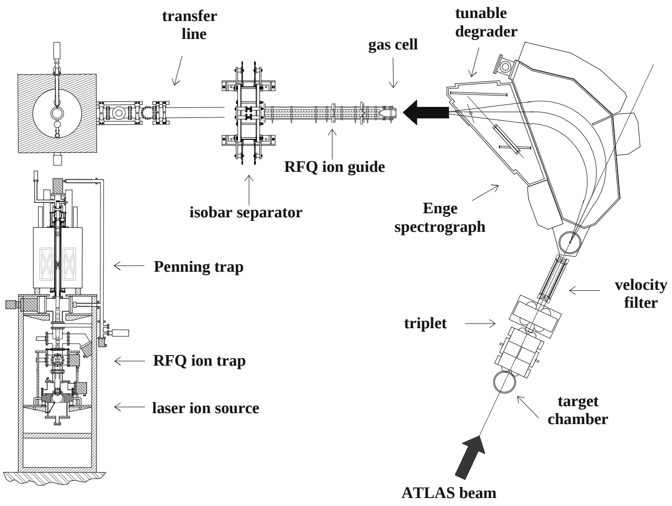

Figure 3.1: An overview of the CPT apparatus. The schematic which occupies the rightmost portion of the figure is a bird's-eye view of the beam elements from the target to the CPT transfer line. At the bottom left of the figure, the schematic shows a side view of the final stages of the ion path, including the linear RFQ trap and the precision Penning trap.

ing process [35] before being transferred efficiently to a linear RF quadrupole ion trap with standard ion optics. During transport, a fast voltage pulse, applied to one of the beam transport elements, efficiently suppresses isotopes outside a restricted range of masses before being transmitted to the RFQ. The RFQ is used to accumulate several bunches of ions and cool the ions prior to injection into the precision Penning trap ($B \sim 5.9$ T) for the mass measurement.

A detailed description of each component of the apparatus along the ion flight path is given. The beam elements are collected into three categories: production, collection and separation, and measurement. After these descriptions, a typical measurement cycle will be provided followed by the techniques used to tune the system during a typical experiment and a brief description of the software and hardware used to acquire the data.

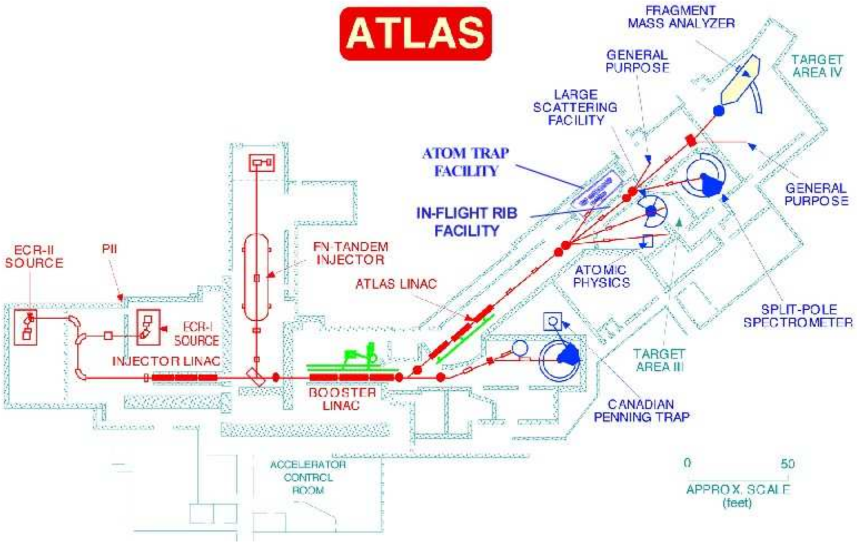

Figure 3.2: The ATLAS facility at ANL.

3.1 Production

The first step in the procedure of making mass measurements is the production of the desired nuclides. All of the rp-process nuclides reported here were created with the combination of ion beams from ATLAS and targets, both of stable elements. This section will provide the necessary details of these devices.

3.1.1 ATLAS

The **A**rgonne **T**andem **L**inac **A**ccelerator **S**ystem (ATLAS) facility shown in Fig. 3.2 was the first superconducting accelerator in the world to accelerate particles heavier than an electron. When ATLAS was first constructed, a cesium sputter ion source was the sole source of ions. Negative ions from the ion source are injected into a 9 MV Van de Graaff tandem accelerator which raises the energy of the ions in two stages: first, the negative ions are accelerated towards the terminal at which point a carbon foil stripper converts the negative ions into positive ions; the ions are then repelled from the terminal and exit the tandem. This method of providing ions was limited to ions with A<82 until 1992, when the **P**ositive **I**on **I**njector (PII) was built and expanded the range of ions accelerated up to uranium. Two ion sources of the ECR (**E**lectron **C**yclotron **R**esonance) type now exist to inject positive ions into PII. Within an ECR source, the element to be accelerated is introduced in vapour form into a microwave-induced plasma. Confined by magnetic fields, atoms of the element are ionized as they collide with electrons within the plasma. The ions then emerge from the ion source with a charge state distribution, but only one particular charge state is selected for acceleration. For experiments requiring an ion beam with high energy, one of the higher charge states is chosen. If high beam intensity is a requirement, then the most abundantly produced charge state is used. Upon exiting the ECR source at about 0.5% of the speed of light, or about 0.005c, the continuous beam is bunched before being injected into the PII linac which consists of 18 superconducting resonators to accelerate the ions to 0.06c. The niobium superconducting resonators were developed at ANL and accelerated an ion beam for the first time in 1978. Each resonator is a resonant cavity which can provide strong RF fields used to accelerate the ions across gaps between drift tubes internal to the cavities. With an accelerating potential of up to 800,000 volts across each resonator, a total potential of 12 MV is achieved through the PII.

Regardless of the source of ions, either from the PII linac or Tandem accelerator, further acceleration is achieved through the 20 MV 'Booster' linac which consists of 24 more superconducting resonators. At the low energy end of the Booster linac, a beam sweeper permits a periodic removal of the beam via the application of high voltage on sweeper electrodes, similar to the deflection pulse used in the CPT apparatus which will be described later. The period and duty cycle of the sweeper pulse can be varied and can be driven by an external signal as may be provided by an experimenter. This mode of operation is useful for experiments with time sensitive detection systems or for avoiding reactions on target frames during a change of targets such as is the case with the rotating target wheel of the CPT. After the Booster linac, the ion beam can be directed towards the CPT or around a 40° bend and through an additional

18 resonators in the 20 MV ATLAS linac to provide ions with velocities approaching 0.15c which are required for other experiments. Overall, ATLAS provides beams of stable nuclides from hydrogen to uranium with energies on the order of 17 MeV per nucleon for lithium and 8 MeV per nucleon for uranium.

3.1.2 Tuning the beam

For all experiments performed with the CPT, measurements of ground state masses (and the occasional isomeric states) are performed. However, most nuclides of interest created online have small production cross-sections ($\sim$ 1-10 mbarn). Therefore, the CPT demands a high intensity beam with an energy just slightly higher than the Coulomb barrier to maximize the production of the desired nuclides. The capable ATLAS staff are responsible for delivering such a beam on target. Generally, for CPT experiments, the most abundant charge state produced by the ECR source is chosen and the various ATLAS components are optimized to provide a well focussed beam spot on target with high efficiency. Initially, the ATLAS operators meet these requirements by monitoring Faraday cups, which measure beam current, and scanners, which show the beam profile, at many positions along the beam path. Once beam is delivered to the target, the experimenters can monitor the beam current, but the ATLAS operators can still watch for changes in the beam profile which may indicate problems with the delivery of beam.

3.1.3 The target

Production of the desired nuclides is accomplished with a target wheel (as seen in Fig. 3.3) in conjunction with ion beams from the ATLAS facility. Located approximately 3 meters upstream from the Enge spectrograph, the target wheel consists of 16 individual targets at the edge of the wheel's 6" radius. As opposed to a single target which was originally used, the target wheel can withstand higher beam intensities. In fact, online tests of this target wheel have shown that 1 mg/cm^2 ^{12}C targets can easily

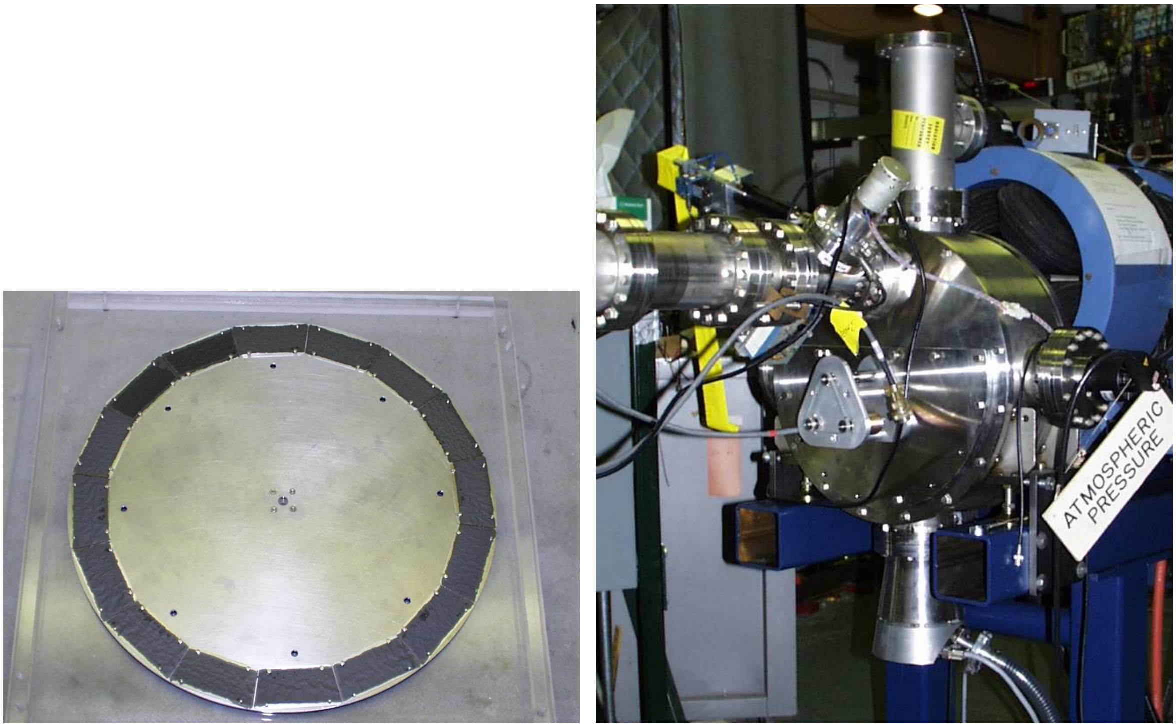

Figure 3.3: On the left is a picture of the production target wheel showing 16 carbon targets at the outer diameter of the wheel. On the right is a picture of the vacuum housing for the rotating target wheel. The beam from ATLAS enters from the left and strikes the target in the upper section of the cylindrical vacuum chamber before entering the magnetic quadrupoles (in blue).

withstand 100 particle nanoamps (pnA) of ^{58}Ni for the duration of a run, typically four days.

The target wheel, an externally powered motor, and an encoder to monitor the wheel's position all have gears which are linked together with a chain. Therefore, assuming the gears of the target wheel and encoder are firmly connected to their respective shafts, any change, or slippage, in the rotation of the wheel will be reflected accurately by the encoder. Under normal operation, the wheel rotates at about 1000 revolutions per minute while the position of the wheel is continually monitored by a CAMAC module. The module can be programmed to issue a signal to the ATLAS beam sweeper which deflects the beam at prescribed positions of the wheel thereby preventing the ion beam from hitting the 'spokes' between targets or specific targets themselves. Currently, one entire revolution of the wheel represents a change of 1024 units in the counter of the CAMAC module. Each 'spoke' is given a conservative width of 6 units, leaving 58 units for each target.

3.1.4 Fusion-evaporation reactions

The nuclides studied in this thesis were produced through fusion-evaporation reactions between heavy ions beams from the ATLAS facility and targets of stable nuclei. Specific combinations of beam and target nuclei are chosen which have the highest expected yield for the desired nuclides. Programs such as PACE [36] are used to assist in the selection of beam and target nuclei, in addition to a determination of the incident beam energy which maximizes production. During a reaction, the incident beam nuclei amalgamates with the target nuclei forming a compound nucleus. As the nucleons of the incident particles undergo collisions with the target nucleons, the initial kinetic energy of the beam particles, in addition to the binding energy released during the reaction, is shared between all nucleons of the two nuclei. The excess energy of the beam/target system yields a small probability of a nucleon gaining enough energy to be released, or evaporated from the system. If a higher incident beam energy is used, more nucleons are evaporated from the beam/target combination. The initial momentum of the compound nucleus together with the recoils from each of the evaporated particles results in the reaction products emerging from the target in a cone. Focussing elements are needed to collect these nuclides and these required elements are described in the next section.

3.2 Collection and separation

Once the nuclides of interest have been produced, the next process involves the transfer of ions with the requisite ion properties to the precision Penning trap. The ions must be bunched with a minimal energy spread and free of contaminant ions. The beam elements which are described below serve at least one purpose in providing the necessary ion properties quickly and efficiently.

3.2.1 Magnetic quadrupole triplet

Downstream immediately following the target wheel lies a magnetic triplet to focus the recoil products into the Enge spectrograph. If no focussing elements existed, the cone of reaction products emanating from the target would result in poor efficiency. Originally, a single target was positioned at the entrance of the Enge spectrograph, but many reaction products were suspected never to have entered the Enge and many of those that did were thought to hit or scatter off of the poles of the magnet. To increase the efficiency, the target position was moved approximately 3 meters upstream to its current position to accommodate the insertion of a magnetic triplet and velocity filter.

A single magnetic quadrupole field by itself with a field axis along the z-axis can focus along one direction, say the x-axis, while defocussing along the y-axis. To focus along both the $\hat{x}$ and $\hat{y}$ directions, at least two magnetic quadrupoles are required, but the focal points of such a doublet system are different, resulting in astigmatic focussing. A combination of three magnetic quadrupoles results in much

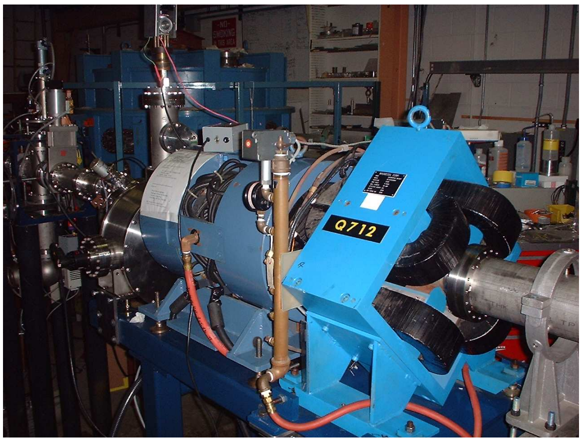

Figure 3.4: The magnetic quadrupole triplet. Reaction products which emerge from the target on the left travel through a combination of a doublet, then a singlet, before entering the velocity filter off to the right.

better stigmatic focussing properties compared with the magnetic doublet.

The magnetic triplet in the CPT system shown in Fig. 3.4 is composed of a doublet from Alpha Scientific on loan from Stony Brook University, and a singlet from Magnecoil Corporation. The lenses are separated by 16 inches with the first lens 12.3 inches from the target and the last lens is 51.8 inches from the old target position at the entrance of the Enge spectrograph. Vertical focussing is provided by the first and third lens while the center lens provides horizontal focussing. In other words, if each lens were to act alone, the first and third lens would produce horizontal lines at the old target position, while the second lens would produce a vertical line. The combination of the three lenses yields a spot at the entrance of the Enge spectrograph, or image location, with twice the size of the object spot at the target wheel. Each magnet is water cooled and has an independent current supply. The magnetic triplet can focus ions which emerge from the target within 3° of the beam axis, and the net result is an increase in the number of recoil products entering the Enge spectrograph by about a factor of three.

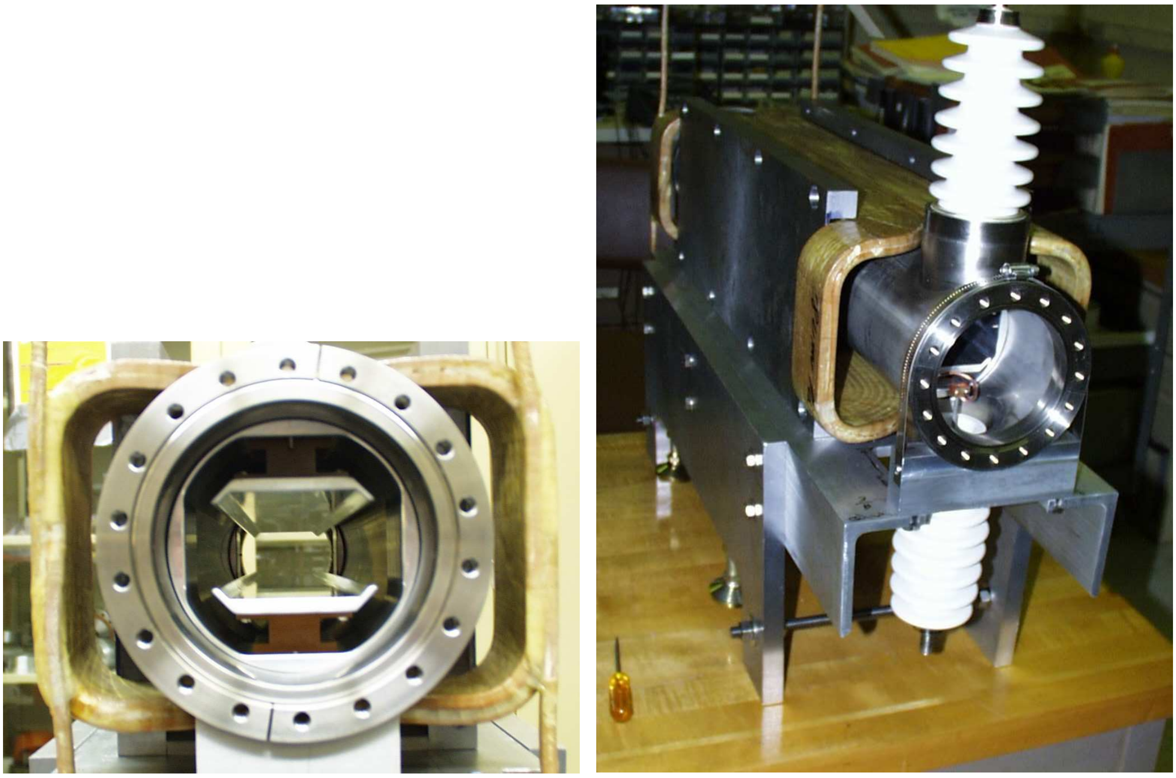

Figure 3.5: The velocity filter. A view through the velocity filter is shown on the left, and an external view of the device is shown on the right.

3.2.2 Velocity filter

Following the magnetic triplet is a velocity filter, shown in Fig. 3.5, whose purpose is to separate the recoil product of interest from the primary beam. The electric field of the velocity filter is provided by two 70 cm long parallel plate electrodes separated by 5 cm. A potential difference of 100 kV can be applied across the plates. The magnetic field of the velocity filter, which is perpendicular to the electric field, is provided by a 'box' magnet with 40 turns of hollow copper tubing. Fields of up to 1500 Gauss can be obtained with up to 300 A applied through the water-cooled coils. The appropriate balance of electric, E, and magnetic, B, field strengths will allow ions of a particular velocity v to traverse the 70-cm length of the filter unhindered as $v = E/B$. The rejection of ions with other velocities is determined by the dispersion of the device which can be increased by raising the strengths of the two fields while maintaining

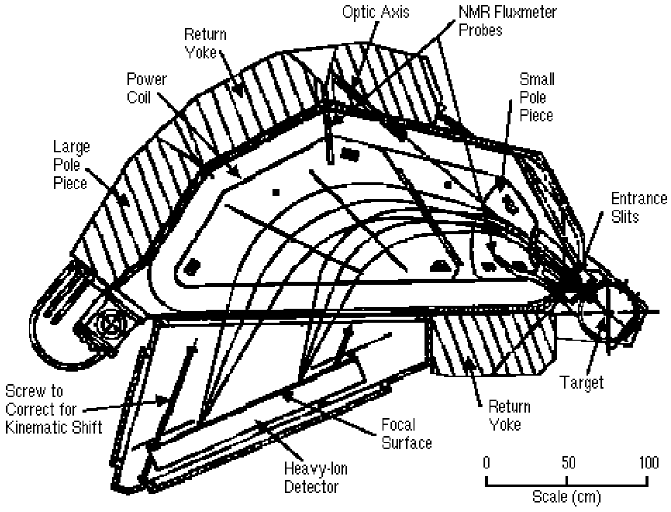

Figure 3.6: The Enge split-pole spectrograph.

the ratio. For our purpose, a deflection of the primary beam by about 0.6 cm over the 70-cm length of the filter is sufficient to prevent the beam from entering the Enge spectrograph. Through online tests of the velocity filter, we have successfully suppressed the primary beam by five orders of magnitude while transferring the recoil products through to the Enge spectrograph.

3.2.3 Enge spectrograph

The Enge spectrograph [33] shown in Fig. 3.6 is of the split-pole type, so-called because the two magnetic dipoles are enclosed within a single coil. The split between the poles permits second-order double focussing over a wide range of momenta. In other words, stigmatic focussing is achieved and the expression which describes image aberrations contains vanishing terms of second order in the angles of acceptance. For a field setting, B_{Enge}, ions will be focussed onto the focal plane with a bending radius ρ according to the charge state and momentum of the ions such that:

$$B_{Enge}\,\rho = \frac{p}{q}. \tag{3.1}$$

For purposes of the CPT apparatus, the Enge spectrograph serves to separate the nuclides which enter the spectrograph, thereby minimizing the number of undesired nuclides which enter the gas catcher. Only those nuclides which have a bending radius of 72 cm will arrive at the gas catcher. Since the nuclides entering the spectrograph have multiple charge states, the efficiency of collecting ions of one species is low (on the order of 20% for ions with Z $\sim$ 30) because the different charge states focussed onto the focal plane are separated by distances significant enough to permit only one charge state of the desired ion species entering the gas catcher. The situation somewhat improves for ions with low Z, as the distribution of charge states is limited to only a few charge states. If a gas, such as nitrogen, is introduced into the Enge spectrograph at low pressures, the ions entering the spectrograph undergo atomic collisions with the gas and exchange electrons in the process. The trajectory of such ions over their entire path length can be described by ions with a mean charge state, $< q >$. According to Ref. [37], the mean charge state can be approximated with:

$$< q > \quad \propto \; v \, \mathrm{Z}^{\gamma} \tag{3.2}$$

with $\gamma \sim 0.45$. Therefore, the magnetic rigidity, $B_{Enge}\ \rho$, can be expressed as:

$$B_{Enge}\ \rho = \frac{p}{< q >} \propto \frac{m}{\mathrm{Z}^{\gamma}} \tag{3.3}$$

which is independent of the velocity. The main advantage of a gas-filled Enge spectrograph, therefore, is the ability to separate isobars. Attempts were made to operate the Enge spectrograph of the CPT apparatus in gas-filled mode, but our experience has shown that the efficiency of this process is less than the efficiency of collecting only one charge state with the Enge spectrograph in vacuum mode. The reasons for the additional loss of efficiency are not completely understood. Therefore, since an efficient system is a priority for measurements of weakly-produced isotopes, the gas-filled mode was abandoned for the more efficient vacuum mode for all experiments reported here.

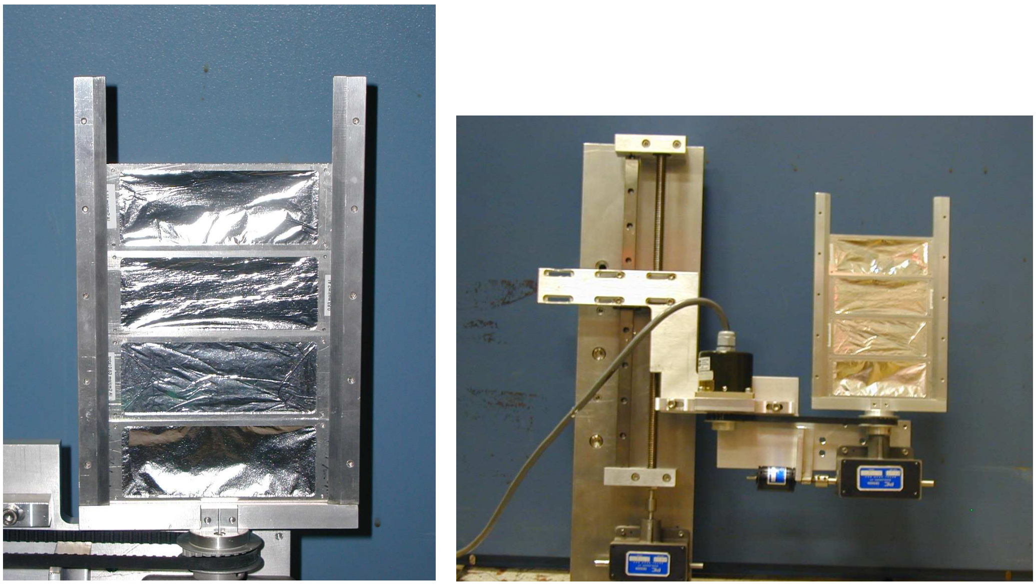

Figure 3.7: The picture on the left shows the degrader structure with four different thicknesses of aluminum foil. On the right is a picture of the degrader assembly, including the drive just below the degrader which rotates the degrader and the drive at the bottom left which changes the vertical position of the degrader ladder.

3.2.4 Degrader

Ion samples of low energy and minimal energy spread are required for a precise mass measurement. ATLAS beam energies are chosen to maximize production of the desired species, but the resulting energy of the desired species after they emerge from the target remains on the order of a few MeV/u. The gas catcher described in the next section is excellent at compressing the intrinsic energy spread of the ion beam, but the gas catcher cannot efficiently cool ions with energies greater than about 3 MeV. The reduction of ion beam energy to ~ 3 MeV is accomplished by the degrader which is positioned near the focal plane of the Enge spectrograph in front of the gas catcher.

The degrader, shown in Fig. 3.7, is a ladder-like structure with the spaces between the ‘rungs’ occupied by foils of aluminum of different thicknesses. There exist five such rungs, with one rung (the top rung) having no foil. The foils occupying the remaining spaces are chosen to yield a range of stopping power for the desired nuclides for each

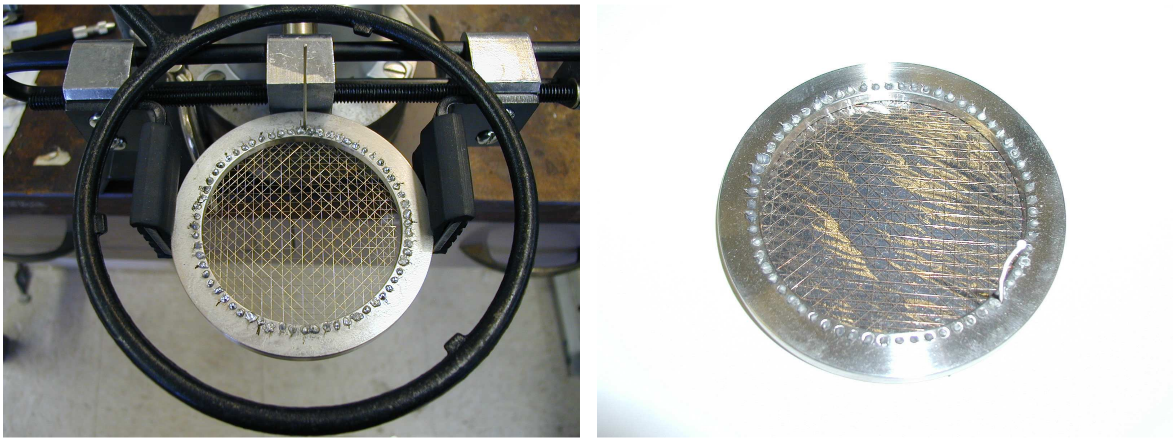

Figure 3.8: Gas catcher window. The picture on the left shows the window frame including the wire grid. Along the inner diameter of the frame are the welds which hold the wire grid in place. The cell window on the right includes the HAVAR® foil.

experiment. The four foils of different thicknesses permit an almost continuous range of stopping power as the ladder structure can be rotated.

3.2.5 Gas catcher

The basic concept of the gas catcher developed at ANL [34] is to provide low-energy ion beams by thermalizing incoming ions in high-purity helium gas. The gas catcher provides an efficient means of transforming multi-charged ions with MeV energy spreads to singly- or doubly-charged ions with energies less than 1 eV. To accomplish this feat, the gas catcher has three essential parts: a thin metal window, a cylindrical volume containing the gas, and an extraction nozzle, all of which are described below. Due to its success, the gas catcher has become a key ingredient for future radioactive beam facilities such as the **R**are **I**sotope **A**ccelerator (RIA).

The cell window is a 1.9 mg/cm^2 HAVAR® foil mounted on a stainless steel frame and reinforced by a 90% transmission gold-plated tungsten wire grid (see Fig. 3.8.) To maintain the ultra high vacuum (UHV) standards of the gas catcher system, the window is sealed to the gas catcher with indium. Although the fundamental purpose of the foil is to separate the vacuum in the Enge spectrograph from the gas catcher volume, the foil must also permit the desired ions to enter the gas catcher.

The 10.5”-long cylindrical volume of the gas catcher has an inner radius of 3” and is fed purified helium through a leak valve to maintain a pressure of approximately 150 Torr within the gas catcher volume. The helium gas is constantly being replaced since vacuum pumps connected to the first section of the ion cooler remove gas through the extraction nozzle of the gas catcher. Purification of the gas is realized with a two-step process. First, the helium passes through an activated charcoal filter cooled with liquid nitrogen to remove any molecular contamination. The gas is further purified with a commercial Mono Torr® purifier from SAES Pure Gas, Inc. to remove any leftover molecular contamination. All gas lines are made of stainless steel and all connections are of the VCR® type. The complete purification process transforms the initially 99.995% pure helium gas (as indicated by the manufacturer) to sub ppb purity.

Ions entering the gas catcher volume lose energy from colliding, and subsequently ionizing, the room-temperature helium gas. Each ion which enters the gas catcher with 3 MeV on average creates 3 MeV / 40 eV = 7.5×10^4 ion-electron pairs, an overwhelming number. (The average energy lost to create one helium ion-electron pair is $\sim$ 40 eV.) Hydrocarbons normally present in vacuum systems can be ionized by the helium ions through charge-exchange reactions. At low energies, the desired ions can interact with these contaminant ions, either becoming neutral or perhaps a molecule in the process, thereby reducing the extraction efficiency. The gas flow alone is insufficient in removing the ions quickly enough to prevent the charge-exchange reactions of the desired ions with the molecular contaminants. Electric fields are required.

To prevent the desired ions from neutralizing or forming molecules, an electric field along the length of the gas catcher guides the ions to the extraction nozzle more quickly than gas flow alone. The voltage gradient is generated with the application of a DC voltage at opposite ends of a resistor chain which links adjacent electrodes. Typical voltages are shown in Table 3.1. In total, 12 cylindrical electrodes of equal

Table 3.1: The DC voltages (in volts) applied on the gas catcher . The gas catcher is divided into two parts, the cylinder and the nozzle, by the 'middle' electrode. A voltage gradient along the length of the gas catcher guides the ions from the window to the extraction nozzle and is established when DC voltages are applied at the beginning and end of each division.

Cylinder		Middle	Nozzle	
Start	End		Start	End
140	59	55	51	10

dimensions form the length of the gas catcher. The amount of time it takes for the ions to be extracted is on the order of 10 ms, but can be decreased with stronger electric fields. However, an arbitrary high voltage gradient is impossible since large potential differences between electrodes spaced so closely together can create discharges with the presence of helium gas. These discharges create many ions which disturb the applied field and render the gas catcher inefficient.

A combination of gas flow and DC fields can remove ions quickly from the gas catcher, but rather inefficiently. An increase in efficiency is achieved with the extraction cone, whereby RF fields applied on the cone electrodes generate an RF 'wall' which repels the ions and keeps them from hitting the electrodes. The extraction cone consists of seventy-six 0.017"-thick specially designed parallel plates separated by 0.020" with mica insulators. The unique shape of the plates, as seen in Fig. 3.9, was chosen to minimize the capacitance between the plates and therefore minimize the RF power required to drive the structure. The inner diameter of the plates decreases uniformly from the 3" inner radius of the cylindrical volume to the final plate which is 0.063" in diameter. The RF applied to the gas catcher cone is achieved with a combination of commercial and homemade devices. First, the waveform is generated with an Stanford Research Systems (SRS) DS 345 function generator and the signal is then amplified with a broadband Electronic Navigation Industries (ENI) 240L RF power amplifier. The amplified signal drives the primary coil of a toroidal transformer. The secondary coil is center-tapped, providing both phases of the waveform. Each phase

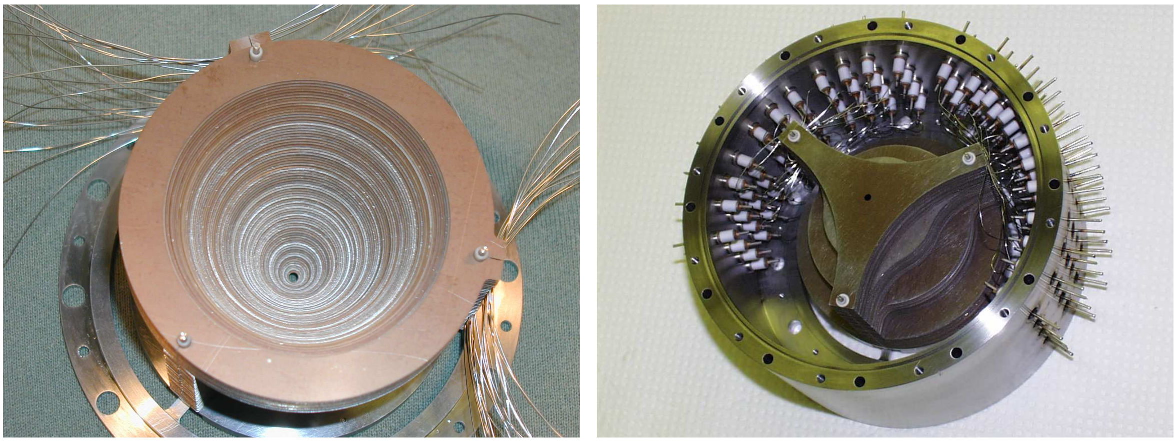

Figure 3.9: Gas catcher extraction cone. The picture on the right is the reverse view of the picture on the left and includes the housing which provides support for and connections to the electrodes.

of the output waveform is then capacitively coupled to every other cone electrode of the gas catcher. The DC supplies which provide the voltage gradient across the cone are inductively connected at the ends of each of the two resistor chains which connect plates of identical phase. The extraction efficiency, defined as the percentage of thermalized ions which are extracted from the gas catcher, is typically 45% for ions with A $\gtrsim$ 40 but decreases for lighter ions. The difficulty in extracting light ions is directly related to the problems associated with applying the required high RF frequencies, but progress has been made recently in preparing for measurements of ^{14}O. The extraction efficiency also depends upon the number of ion-electron pairs created per cm^3 per second, and justifies the installation of the velocity filter, as it reduces the amount of primary beam particles entering the gas catcher. Interestingly, not all ions are extracted in the 1+ charge state. Since some nuclides have a second ionization potential which is less than the first ionization potential of helium ($\sim$ 24 eV), certain nuclides can emerge from the gas catcher in 2+, or even 3+, charge states. To date, no 3+ charge states have been observed, but many ions of the 2+ charge state have been extracted from the gas catcher and transferred to the precision Penning trap.

The gas catcher is a novel device which can provide low-energy cooled ion beams of short-lived isotopes to many diverse experiments. After the ions enter the gas catcher and are thermalized in the high-purity helium gas volume, the combination of electric fields and gas flow permits both a fast and efficient extraction of ions, even with a high intensity of ions entering the device. However, a delicate balancing act between the electric fields and gas flow is required. For example, if higher gas pressures are used to increase the stopping power of the ions within the gas catcher, the RF power applied on the cone must increase since the mobility of the ions decreases with increased pressure. Furthermore, with higher gas pressures and stronger RF fields, a greater DC gradient along the length of the cell is needed to prevent the ions from neutralizing or forming molecules, yet not so strong as to overcome the repulsive RF field. One would normally like to operate at high pressures, but electrical discharges limit the maximum applied fields. In addition, a vacuum system must be able to handle the increased pressure, and since most experiments require the ion beam to be free of residual gas, the helium gas extracted along with the desired ions must be removed. Transferring ions to the experimental apparatus while removing the helium gas is the subject of the next section.

3.2.6 Ion guide and cooler

Mass measurements performed in the precision Penning trap require ion bunches free of residual gas. Since the gas catcher thermalizes ions with high pressures of helium gas, the function of the ion cooler is to efficiently transfer the ions from the gas catcher to a high vacuum regime. The ion guide itself consists of a vacuum chamber separated into three sections by apertures. The vacuum pumps attached to each section of the ion cooler are capable of handling the gas flow and are listed in Table 3.2 along with the pressures realized.

Within each section is a RFQ mass filter composed of four parallel segmented rods as shown in Fig. 3.10. Each rod describes a cylinder with 0.75" diameter and the center-to-center distance between each pair of rods is 1.40". The rods are divided into 0.78"-long segments and each segment is attached to a Mycalex® insulating ceramic

Table 3.2: The vacuum system of the ion cooler. Listed are the vacuum pumps, their pumping speeds, and the background pressures within each section as read by conventional thermocouple and ion gauges. The pressures listed here are with a helium load of ∼ 150 Torr in the gas catcher.

Section	Vacuum pump	Pumping speed l/s (N_2)	Background pressure Torr
I	Osaka Vacuum, Ltd.; Model TS443BW	500	0.55
II	Alcatel; Model ATP 150	140	0.22
III	Leybold; Model Turbovac 361	400	10^{-4}

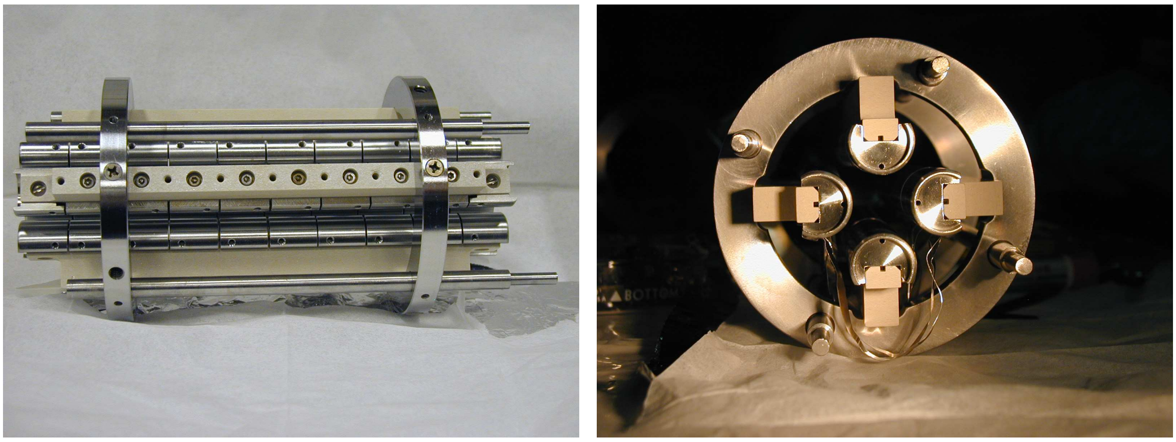

Figure 3.10: One of the RFQ mass filter sections of the ion cooler. A side view is shown on the left and an edge-on view is shown on the right.

Table 3.3: The typical DC voltages (in volts) applied on the ion cooler . These voltages effectively provide a voltage gradient along the rod structure to guide the ions from the gas catcher to the isotope separator. The label DC1 refers to the applied voltage at the beginning of the rod structure in the specified section, and DC2 is applied at the end of the structure. The apertures, or nozzles, between each section are also biased. For Section III, the trap is established by the potentials on the last three segments, namely S1, S2, and S3.

Section I			Section II			Section III					
DC1	DC2	Nozzle_{12}	DC1	DC2	Nozzle_{23}	DC1	DC2	S1	S2	S3	Last nozzle
6	27	6	3.5	2.8	1.5	-0.8	-1.5	-2.5	-5.0	-2.5	7.0

furnishing a 0.020” gap between each segment. Overall, each rod in the first RFQ section consists of 8 segments, the second section contains rods with 10 segments, and each rod in the third section has 25 segments. The ceramic pieces which hold the segments in position are attached to circular rings keeping the distance between rods fixed. Centering rods connect the rings to plates which are bolted to the vacuum chamber. Attached to the plates between the sections are the conical nozzles which have a small open area to provide differential pumping throughout the ion cooler. The aperture at the end of the first section is 2 mm in diameter, the second section also has an aperture of 2 mm in diameter, and the last section has a 6 mm-diameter aperture. When appropriate DC voltages from a homemade 20-channel supply are applied to the beginning and end of each rod structure within each section, a voltage gradient, created by resistor chains which connect adjacent segments, guides the ions from the gas catcher to the isotope separator. However, only those ions which are confined with the appropriate RF frequencies are transferred to the isotope separator, and since any helium ions which enter the RFQ structures are very light, they are usually not confined and are consequently pumped out. Typical DC voltages applied to the ion cooler, including the apertures, are shown in Table 3.3. More details regarding the nozzle structure and the electronics responsible for applying the various voltages can be found in Ref. [38] and Ref. [39].

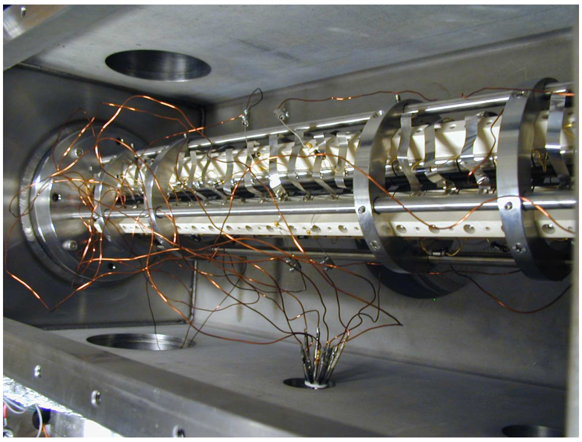

Figure 3.11: The third linear RFQ section installed in the ion cooler.

Linear Paul trap

Shown in Fig. 3.11 is the third RFQ section of the ion cooler. The last three rod segments of this section form a linear Paul trap. As shown in Table 3.3, the first and third sections are held at identical potentials while the center segment is lower in voltage, forming an approximate harmonic potential along the ion beam axis. The linear trap, in combination with the residual helium gas, accumulates and collisionally cools the ions. Once the isotope separator is ready to accept an ion bunch, the ions are ejected from the linear trap with the application of voltage pulses of +30 V, -4 V, and -15 V on S1, S3, and the last nozzle respectively.

3.2.7 Isotope separator

Precise mass measurements require ion samples free of contamination as discussed in Sec. 4.1.2. The process of thermalizing, and later extracting, the ions creates a copious amount of contaminant ions. The high mass resolution obtained with Penning traps make them an ideal device for the reduction of contaminant ions.

At the heart of the isotope separator is a cylindrical Penning trap, consisting of nine electrodes as shown in Fig. 3.12 to provide the electrostatic DC potential which confines the ions along the magnetic field axis. Of these nine electrodes, the

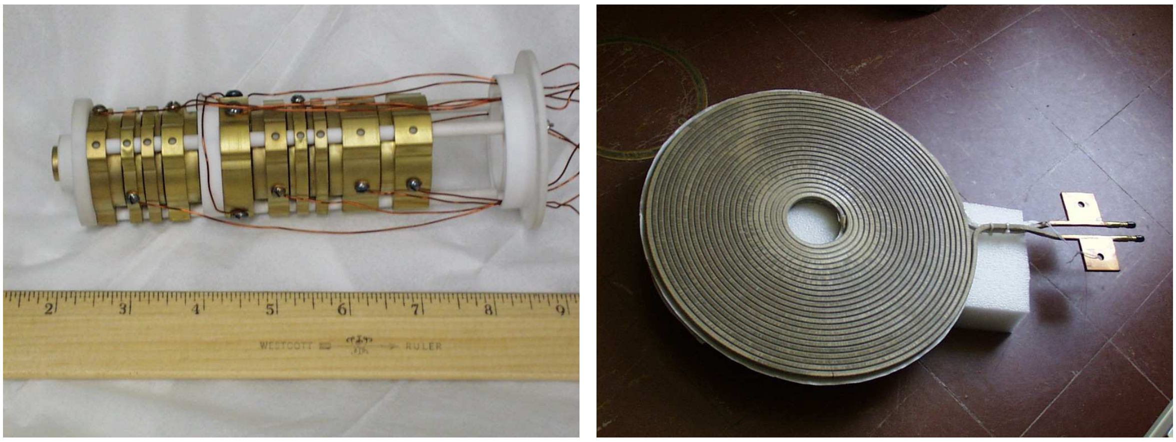

Figure 3.12: The picture on the left displays the Penning trap electrode structure which is used for the isotope separator. The picture on the right shows one of the coils which forms the solenoid for the isotope separator.

central seven electrodes are symmetric about the axial center of the trap. Starting with the second electrode, referred to as IS2, the lengths of each 1.225”-diameter cylindrical electrode along the trap are 0.254” (IS2), 0.254” (IS3), 0.478” (IS4), 0.688” (IS5), 0.478” (IS6), 0.254” (IS7), and 0.254” (IS8). A fourth RFQ mass filter section, schematically shown in Fig. 3.13, exists immediately following the last nozzle to guide the ions from the ion cooler into the high homogeneity field region of the isotope separator. The 0.322”-diameter circular rods are segmented into eight 0.600”-long pieces with a spacing of 0.030” between each segment, and each opposing pair of rods are separated by a center-to-center distance of 0.648”.

Installation of the isotope separator immediately after the ion cooler provided severe space constraints on the design of the device as the ion cooler was already in close proximity to the wall. Normally, to meet the requirements of a homogeneous field with normally conducting coils, a long solenoid is used. Due to the space limitations, a shorter, more compact, solenoid was constructed. Overall, the 1-Tesla magnetic field is produced with 250 A of current running through eight water-cooled coils, one of which is shown in Fig. 3.12. Circular steel end plates and a tubular outer shell provide the housing for the pancake coils. A brass tube inserted through the inner diameter of the solenoid gives support to the coils and is mounted to the end plates.

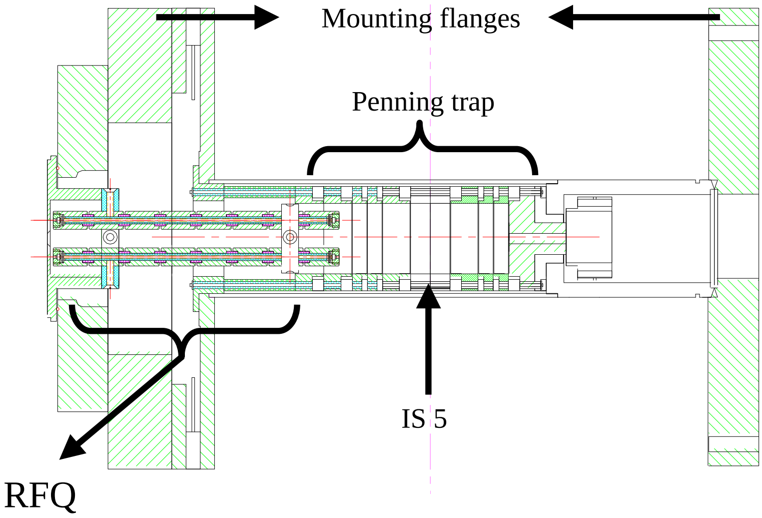

Figure 3.13: A schematic of the isotope separator showing both the RFQ structure and the electrodes which form the Penning trap. The central electrode of the isotope separator, IS5, is identified.

Two steel concentric rings within the bore of the magnet provide tunable elements used to flatten the field in the critical trapping volume. Pairs of pancake coils are staggered such that the water and electrical connections emerge from the outer tube at 90 degrees with respect to each other. Due to the natural resistance of the coils, a 10 kW current supply is required to drive the coils with 250 A. However, a long-term drift of the field is found in correlation with the observed heating of the steel housing. In addition, as the bore is in thermal contact with the end plates, it outgasses as the temperature of the end plates rise. Therefore, to minimize outgassing and the field drift, water is flowed through the coils to keep the steel, and especially the bore, cool. However, the standard water pressure available was found to be inadequate, so a water pump which increased the water pressure on the inlet side from 70 psi to 250 psi was installed.

Ion capture in the isotope separator

Capturing the ions in the isotope separator requires the voltages applied to S3 of the linear trap, the last nozzle, and electrodes IS1, IS2, and IS3 of the isotope separator

Table 3.4: The typical DC voltages (in volts) applied on the nine isotope separator (IS) electrodes. Ions from the ion cooler are captured into the isotope separator with the voltages specified by ‘Capture’. During the mass selection process, the ‘Excitation’ voltages are used. Finally, the ions are ejected with the voltages specified by ‘Eject’. The values highlighted in red are to emphasize the differences between the ‘Capture’ and ‘Eject’ modes from the ‘Excitation’ mode.

	IS1	IS2	IS3	IS4	IS5	IS6	IS7	IS8	IS9
Capture	-10	-10	-8	-6	-8	-6	-1	1	15
Excitation	1	1	-1	-6	-8	-6	-1	1	15
Eject	1	1	-1	80	-8	-80	-100	-100	-250

to be momentarily decreased, establishing a voltage gradient to guide the ions into the isotope separator. The duration of this “pulse” is dependent upon the time of flight, and therefore mass, of the desired ions such that the length of the pulse must allow sufficient time for the desired ions to enter the trap, but not too long so that they deflect back out through the entrance aperture. Typical voltages used to capture an ion bunch are shown in Table 3.4.

Mass selective cooling process

The size of the apertures in the last nozzle of the ion cooler and the IS9 electrode were chosen to provide a residual buffer gas pressure of $\sim 10^{-4}$ Torr inside the isotope separator necessary for the mass selective cooling process. No additional gas is introduced. The quadrupole field excitation at the cyclotron frequency of the desired ions is achieved with a waveform from a SRS DS345 function generator applied to the split central electrode of the Penning trap. For field durations of 400 ms, an amplitude of 0.05 V (as read by the function generator) yields a resolving power, $m/\Delta m \sim 1000$ at A = 100 u.

Ejection of ions from the isotope separator

If the mass selective cooling process is complete and the next ion trap (the linear Paul trap immediately preceding the precision Penning trap) is ready to accept ions, the ions from the isotope separator are ejected through the aperture in the IS9 electrode of the isotope separator with pulses of a positive voltage on the IS4 and a negative voltage on IS6, IS7, IS8, and IS9 electrodes. Typical voltages used to eject ions from the isotope separator are shown in Table 3.4.

3.2.8 Deflection pulse

Even with the resolving power provided by the isotope separator, small amounts of contaminants still persist in the ejected ion pulse. A fast deflection pulse, applied to the beam transport system, effectively suppresses the transmission of isotopes outside a restricted range of masses. This pulse is applied to an electrode structure composed of 1-inch square plates which are situated at the entrance of the last 90° bend. These plates are oriented to form a cube with two opposite ends missing to permit the beam to pass through it. Three of the plates are biased at the drift tube potential, while the other plate, the "deflection plate" is biased with a DC potential large enough to deflect all incoming ions away from the entrance of the 90° bend. An additional plate at the entrance of the deflection pulse is used to shield this DC voltage from penetrating into the drift tube structure. In this manner, the incoming ions do not experience the change in potential until their arrival at the deflection plate. Once they enter the structure through the 1 cm-diameter aperture, the ions are deflected unless the voltage on the deflection plate is sufficiently close to the nominal drift tube potential. The deflection pulse itself is generated with MOSFET switches which can switch quickly between two different voltages, one of which is at ground potential [40]. The pulse, with adjustable amplitude, width, and timing, is AC coupled to the deflection plate. The amplitude is chosen such that the nominal drift tube potential is restored for the appropriate length of time to allow the desired ions to pass through unhindered. Typical parameters which characterize the deflection pulse are shown in Table 3.5.

Table 3.5: Deflection pulse parameters. The electrode normally sits at the DC potential with a pulse of specified amplitude and width to permit a desired isotope to pass through to the entrance of the last 90° bend. The timing of the beginning of the pulse is with respect to the beginning of the ejection pulse of the isotope separator.

DC	Pulse amplitude	Pulse width[1]	Timing[1]
-1810 V	370 V	0.8 μs	69.7 μs

[1] For A=100 u.

3.2.9 Linear Paul trap

An integral part of the CPT apparatus is a linear RFQ ion trap, or linear Paul trap. Its purpose is to efficiently capture, cool, and accumulate ions before their transfer to the precision Penning trap. Cooling the ions is important for accurate mass measurements (see Sec. 3.3.1), while an accumulation of the ions provides a storage mechanism during each mass measurement cycle (see Sec. 3.4.1). Overall, the linear Paul trap essentially acts as a buffer, providing ions for the Penning trap with consistent properties independent of their initial properties upon injection into the linear Paul trap. Therefore, any modifications or problems which may occur with the rest of the system prior to the linear Paul trap does not affect the accuracy of the mass measurements conducted in the precision Penning trap.

Originally, the Paul trap was a three-electrode structure consisting of two endcap electrodes with an intermediate ring electrode [41]. In the fall of 2001, it was replaced by the linear Paul trap shown in Fig. 3.14, whereby the original ring electrode was replaced by two pairs of segmented parallel rods identical to the linear Paul trap in the ion cooler. The entire Paul trap assembly consists of the segmented rods with segments S1, S2, and S3 as labelled in Fig. 3.14, a deceleration electrode below the trap and an endcap electrode above. The circular rods are 0.75" in diameter, are 0.78" long, and each pair of rods are separated by 0.65". Apertures of 0.2" in diameter in the deceleration and endcap electrodes enable ions to be injected into and ejected from the trap. A lens above the trap structure focusses the ejected ions through two

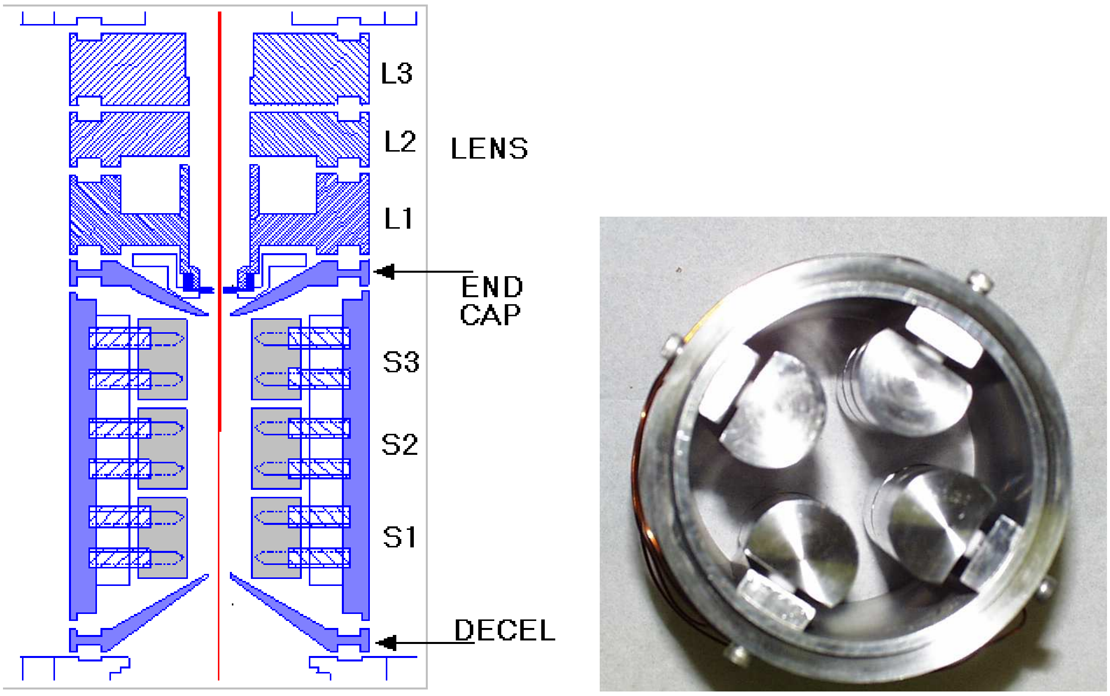

Figure 3.14: A schematic of the linear Paul trap is shown on the left. All electrodes are shown in either solid or hatched blue, except for the rod segments which are in grey. On the right is a picture of the rod structure mounted within its cylindrical housing.

more apertures to align them along the magnetic field axis of the Penning trap.

In comparison with the previously used three-electrode structure, the linear Paul trap is much more efficient and is much easier to operate. For example, the RF applied to the ring electrode of the original Paul trap results in a time-varying force along the longitudinal axis, or the axis in which the ions are injected and subsequently ejected. Ions must therefore be injected carefully into the Paul trap by synchronizing the injection with the RF applied. However, the RF applied to the rods of the new linear trap creates no such time-varying force along the longitudinal axis, and therefore the RF-phase criterion is not critical. The typical efficiency to collect, cool, and accumulate ions with the original Paul trap was 15%, whereas we routinely get 80% or better with the new linear Paul trap.

Ion capture in the Paul trap

The velocity of the ions approaching the Paul trap is reduced before they enter through the small aperture in the deceleration electrode. To capture the ions, the voltage on the deceleration and S1 electrodes is lowered for a certain time which is mass dependent. The duration of this “capture pulse” is chosen so that the ions are given enough time to enter the trap, but not so long so that they deflect back out through the entrance aperture. Since one of the purposes of the linear trap is to accumulate ions, the voltage drop applied on the deceleration and S1 electrodes is limited to about 9 V. If the voltage drop was any larger, the accumulated ions could leak out. Typical voltages used to capture an ion bunch are shown in Table 3.6.

Storage and accumulation

Once inside the Paul trap, the ions lose any excess energy due to collisional cooling with He buffer gas. In this manner, many successive ion pulses can be captured and thus ions will accumulate in the Paul trap while mass measurements are being made in the Penning trap. Helium gas at room temperature is fed through the cylindrical

Table 3.6: The DC voltages applied to the linear Paul trap during the capture, cooling, and ejection of ions. The values highlighted in red are to emphasize the differences between the ‘Capture’ and ‘Ejection’ modes from the ‘Cooling’ mode.

	Voltage applied		
Electrode	Capture	Cooling	Ejection
Deceleration	-15	12	12
S1	-10	-1	60
S2	-11	-11	-11
S3	-1	-1	-60
Endcap	16	16	-60

housing into the trap to maintain a pressure of 10^{-4} to 10^{-5} Torr in the trap volume. The number of ions captured increases with the number of ion bunches captured, until the space charge built up by the charged ions interferes with the confining potential of the trap at which point ions are lost and a saturation effect is observed.

Ejection of ions from the Paul trap

Once the Penning trap is ready to accept ions, the ions from the Paul trap are ejected through the aperture in the endcap by applying a positive voltage on the S1 and a negative voltage on both the S3 and endcap electrodes. Typical voltages used to eject ions from the linear Paul trap are shown in Table 3.6. Due to the spatial extent of the ion cloud inside the trap, the ions will all experience a slightly different potential upon ejection. This leads to a spread in energy of the ejected ions. Due to the conservation of phase space, any method used to decrease the energy spread, say by decreasing the ejection voltage amplitude, will result in a larger time spread. Since both the time spread and energy spread can affect the efficiency and accuracy of the mass measurement process in the Penning trap, decreasing the spatial extent of the ion cloud is required. Although the system currently uses He gas at room temperature to cool the ions, preparations are currently underway to cryogenically cool the He gas.

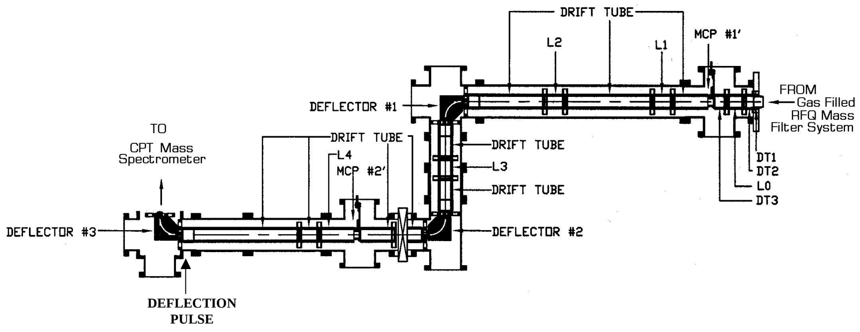

Figure 3.15: Schematic of the beam transport line between the isotope separator and the last 90° bend.

3.2.10 Beam transport

Standard ion optics are used to transfer the ions from the isotope separator to the precision Penning trap. As shown in Fig. 3.15 and Fig. 3.16, a number of 90° bends, Einzel lenses, and steerers are used in the beamline. All Einzel lenses, labelled as Lx in Fig. 3.15 where 'x' is an integer value, are cylindrical structures consisting of three segments. Generally, the central segment is operated at a higher potential than the surrounding two electrodes which are held at drift tube potential. Einzel lenses are used to focus the ion beam, and the steerers, or quads, are used to steer the beam. A set of steerers are located just before the first detector station (MCP 1′) and immediately after each 90° bend. Each set consists of 1"-square plates, identical to the deflection plate electrodes, and are operated in pairs to guide, or direct, the ion beam. The quads are similar to the steerers, but are constructed of a cylindrical electrode which is split into four pieces along the length of the cylinder. Five diagnostic stations, labelled MCP 1′, MCP 2′, MCP 1, MCP 3, and MCP 4 in Fig. 3.15 and Fig. 3.16, consist of microchannel plate detectors used to assist the tuning of steerers/quads and lenses in the system. Silicon surface barrier detectors are also mounted on the same feedthroughs as MCP 1′, MCP 2′, and MCP 3, identified as Si 1′, Si 2′, and Si 3 respectively, to monitor the transmission of β activity.

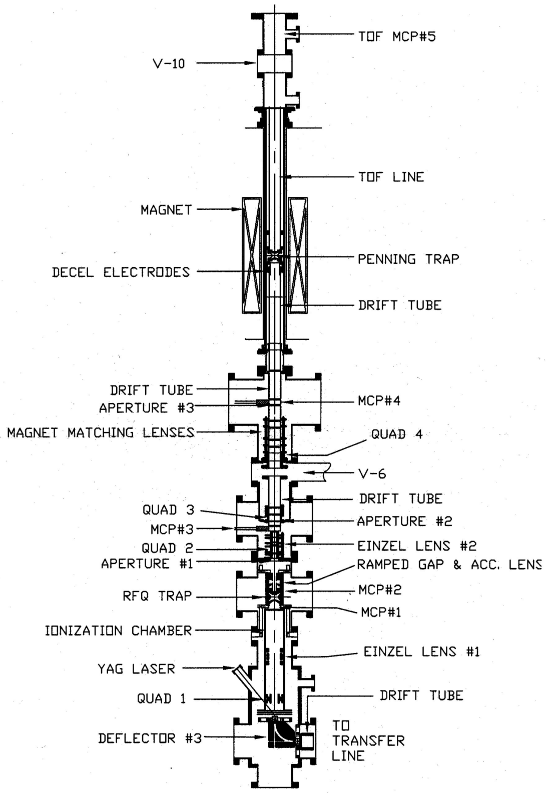

Figure 3.16: Schematic of the Penning trap apparatus after the last 90° bend.

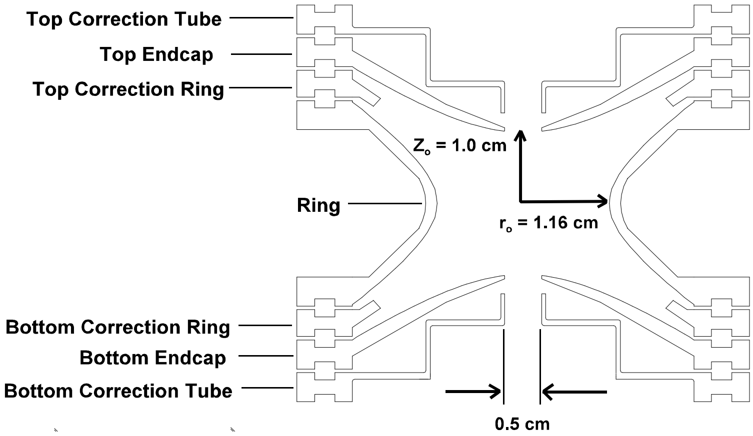

Figure 3.17: Shown are the electrodes which construct the precision Penning trap.

3.3 Measurement

The main purpose of the devices discussed up to this point is for the preparation and delivery of desired isotopes to the precision Penning trap. Once the ion samples are injected into the Penning trap, the measurement process is comparatively simple, involving only the Penning trap, time-of-flight assembly and a microchannel plate (MCP) detector. In this section, the Penning trap will be described along with the manner in which measurements are made.

3.3.1 Penning trap

The precision Penning trap, shown schematically in Fig. 3.17, is a compensated hyperbolic trap with dimensions $r_o = 1.16$ cm and $z_o = 1.00$ cm. The ring electrode is split axially into four equal parts to enable the application of dipole and quadrupole fields. These four electrodes are separated by endcaps on either side of the ring electrodes by correction ring electrodes, so named since they compensate for electric field anharmonicities created by the truncated split ring electrode. Correction tube electrodes are situated on the outside of the trap and correct for electric field imperfections caused by apertures in the endcap electrodes. In total, ten electrodes compose the Penning trap itself. An additional two electrodes below the Penning

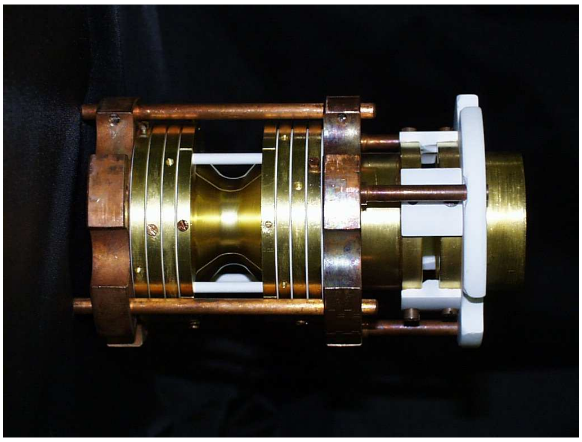

Figure 3.18: Picture of the Canadian Penning trap. The two deceleration electrodes are at the right of the main trap.

trap form deceleration electrodes, whose purpose is to slow down the incoming ion bunches. Each electrode is isolated from every other electrode with insulators made of Macor®. A picture of the Penning trap is shown in Fig. 3.18.

To minimize the systematic effects as discussed in Sec. 4.1.2, all materials within the vacuum chamber in the vicinity of the Penning trap have good vacuum properties, low magnetic susceptibility and the electrodes have excellent electrical characteristics. For example, the ten Penning trap electrodes, the two deceleration electrodes, and the first drift tube electrode above the Penning trap are composed of gold-plated oxygen-free high-purity copper (OFHC). Since copper has low magnetic susceptibility and is a good electrical conductor, it is clearly a good choice of material for the various electrodes. The effect of gold plating the Penning trap electrodes is to improve their electrical properties by reducing patch effects, in which static charge builds up on a surface and distorts the electric field. The entire structure sits within the bore of a 5.9 Tesla superconducting magnet in which the vacuum chamber itself is constructed of molybdenum, a material of low magnetic susceptibility. Maintaining a $\sim 10^{-9}$ Torr vacuum in the Penning trap region is accomplished primarily with a cryogenic pump below and a turbomolecular pump above the trap structure. Only materials with ultra high vacuum properties, such as stainless steel, OFHC, molybdenum, and Macor®, are used to construct all electrodes and support structures within the Penning trap vacuum chamber.

The axial harmonic potential is established by applying appropriate voltages to the Penning trap. The voltages are selected by adjusting potentiometers which control the input to APEX01 op-amps. Stable reference voltages which set the range of allowed voltages are provided by two precision Kenwood PD56-6AD regulated DC power supplies. All AC voltages, including the RF excitations and the pulses used to capture and eject ions in/from the Penning trap, are capacitively coupled to the electrodes.

Ion capture in the precision Penning trap

One important difference between this precision Penning trap and all other traps used in the apparatus is that no residual gas is present to decrease the energy of the incoming ions. Therefore, the capture of incoming ion bunches is achieved solely through the application of appropriate electric fields. In this case, pulses are coupled capacitively to momentarily reduce the electrostatic potential applied on the top deceleration electrode, bottom correction tube, and bottom endcap. Once the ions are successfully captured, the applied pulse ends and the electrostatic potentials are returned to their nominal values to form a harmonic potential. The magnitude of the pulse applied to each electrode is chosen to establish a gradual increase of the axial DC gradient towards the trap center. The width of the capture pulse must be carefully chosen. Ions cannot be located near the bottom electrodes while they are returned to their nominal potential, otherwise as the electrodes reestablish the axial harmonic potential, the ions will receive an energy gain. Instead, the capture pulse ends while the ion bunch is positioned near the upper electrodes. In this manner, the width of the capture pulse, t_c, is usually on the order of one half of the time period, T_z of the harmonic axial oscillation, ie: $t_c \sim \frac{1}{2}T_z$.

Evaporation of high-energy ions

If ions within the captured ion bunch have an intrinsic energy spread, they are prone to experience different magnetic fields due to their varying axial amplitudes which compromises high precision measurements. The energy spread can be reduced by selectively eliminating the high energy ions. All that will remain are the low energy ions which rest at the bottom of the trap's harmonic potential and the ions will therefore probe a much smaller extent of the magnetic field as they undergo small oscillations about the trap center. Even with ion bunches of a well defined energy, in the case of improperly captured ions the magnetic field probed by the ions is significant and can affect the resulting precision. The method employed to eliminate the high energy ions in this work was to reduce the potential of the upper correction tube by approximately 10 V for 500 μs. Once the ions, through their axial oscillation, approach the upper endcap, the ones with high energy "leak" out. This process essentially evaporates away the undesired ions. Another approach, as described in Ref. [39] is to raise the potential of the ring electrode momentarily. In either case, the extent to which the electrode potential is changed depends upon the desired precision and accuracy.

Removal of unwanted contaminants

Systematic effects are caused by the simultaneous presence of both desired and undesired ions. Minimizing these effects requires the removal of the unwanted ions before any excitation is performed on the desired ions. Three different methods have been used to remove undesired ions. All methods utilize the technique of removing ions with the application of a dipole field at the mass sensitive ω_+ frequency.

The first procedure used is one which applies a dipole field at the ω_+ frequency with an amplitude and duration sufficient to remove the ions from trap. Since ω_+ is mass sensitive, each ion species to be removed requires a unique frequency. The frequencies are applied sequentially, with equal duration and amplitude which are chosen to remove all contaminant ions without disturbing the ions whose mass is to be determined. (See Sec. 3.4.2). The second method used is a scan, or sweep, through a set of frequencies. The process is similar to the first method, but the dipole frequencies of the contaminant ions do not have to be identified. Instead, all ions which have a resonance within the frequency range will be removed, and only the reduced cyclotron frequency of the desired ions needs to be identified so that a notch, or gap, in the applied frequencies can be inserted. The third process used is similar to the first, but the frequencies are applied simultaneously, not sequentially. With a summing amplifier to provide the simultaneous application of all desired frequencies, this method minimizes the amount of time needed to remove contaminant ions but it requires more function generators since each function generator provides only one dipole frequency. However, one big advantage is that the amplitude and duration of each frequency can be individually controlled. Although the three methods are listed in somewhat of a historical order with a perceived increase in advantage with each new method, some experiments used a combination of methods.

Establishing the initial orbital motion

Precise mass measurements are obtained with the CPT via a conversion of an initially pure magnetron motion to one of a reduced cyclotron motion. An accurate mass measurement is made by comparing the cyclotron frequency obtained for a desired ion to that of a reference ion which requires that the amplitudes of the initial magnetron motion be consistent to ensure the magnetic field volume probed by both the reference and unknown masses are identical. Once the previous procedures are complete, the remaining ions are exposed to a dipole field at the magnetron frequency which establishes a well defined initial orbital radius. The radius of the ω_- motion can be selected with a proper choice of the amplitude and duration of an applied dipole field. Since ω_- is mass insensitive, all ions in the trap will respond similarly. Typically, the magnetron radius is established with a 1570 kHz sinusoidal waveform of 0.016 V in amplitude for a duration of 40 ms.

Conversion via the cyclotron frequency

After the magnetron motion has been established, a complete conversion to the reduced cyclotron motion occurs when a quadrupole field excitation at the cyclotron frequency is applied. The parameters of the quadrupole field are dictated by the desired precision. As seen from Eq. 2.89, a higher resolution is achieved when the trapped ions are exposed to the quadrupole field for longer durations. Furthermore, for a given duration, a particular amplitude of the applied waveform as determined from Eq. 2.83 will provide a complete conversion between the reduced cyclotron and magnetron motions. Since the sinusoidal waveforms which generate the quadrupole field first pass through a variety of electronics which attenuate higher frequencies, the amplitude of the waveform generated by the function generator must be adjusted to compensate for the loss in power through the various electronics. Due to this effect, the amplitude of the applied quadrupole field is tuned before each experiment to ensure a full conversion between the eigenmotions is accomplished. See Sec. 3.4.2 for more details.

Time-of-flight section

Once the application of the quadrupole field is complete, the ions are ejected from the Penning trap and are guided along the magnetic field axis through a series of drift tube electrodes until they reach the final MCP detector. These electrodes, shown schematically in Fig. 3.19, form the time-of-flight section. The first such electrode, labelled as TOF A in Fig. 3.19, is necessarily long to permit a complete conversion of the radial energy gained by ions in the trap to axial energy. Similar to the Penning trap electrodes, TOF A is constructed of gold-plated OFHC. The electrodes from TOF B to TOF F are made of OFHC but are not gold-plated, and the other electrodes, which include TOF H, TOF I, and the stress rings, are constructed of stainless

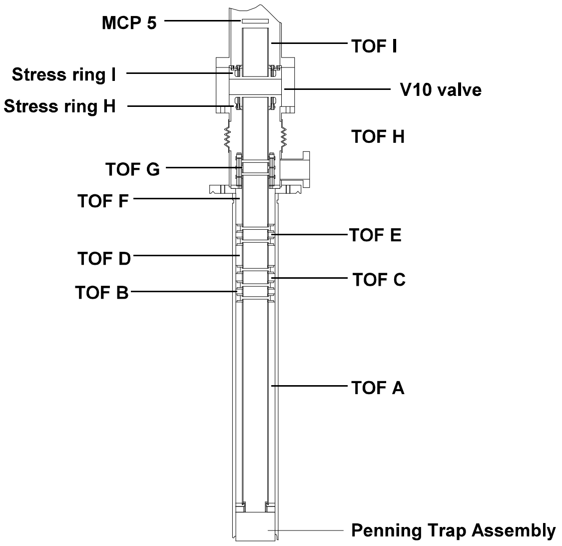

Figure 3.19: Schematic of the time-of-flight assembly which guides the ions from the Penning trap to the final MCP detector.

steel. The entire assembly, including the Penning trap, is mounted together with rods attached with set screws to centering rings which simultaneously set the spacing and alignment of the electrodes. The centering rings, in addition to the molybdenum vacuum tube, are machined with high tolerance. If any slight misalignment exists between one TOF electrode and another, the centering rings would not be parallel and the assembly would not slide easily into the vacuum tube. This tight fit ensures the initial alignment [42] between the electric field and the magnetic field is maintained.

Microchannel plate detector

The impact of the ions on the MCP detector comprises the final part of the mass measurement process. Two microchannel plates arranged in a chevron configuration together with an anode form the detector as shown in Fig. 3.20. The electron multiplication, or signal gain, is achieved with a potential difference of $\sim$ 975 volts applied across each plate. An additional acceleration to the anode which serves to collect the electrons is achieved with a potential difference of $\sim$ 50 V between the second microchannel plate and the anode. Both plates have an active area of 40 mm with 10 μm-diameter channels separated (center-to-center spacing) by 12 μm.

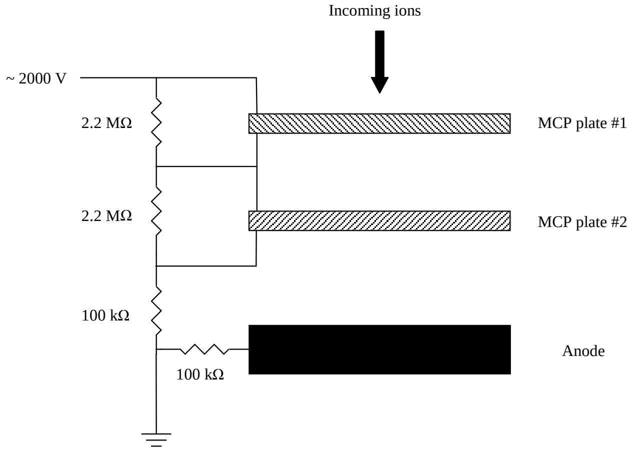

Figure 3.20: Configuration of the MCP detector.

The channels are oriented at angles of 8° and the length to diameter ratio is 46:1. Electrons collected on the anode generate a signal which is then processed according to the description given in Sec. 3.4.3. Based solely on the amount of surface area occupied by channels, the maximum efficiency expected is $\sim 50\%$.

3.4 Operation

Due to the complexity of the CPT apparatus, the process to transfer the desired ions from their production to final detection, in addition to the mass measurement process itself, is quite involved. Many devices are required to ensure a fast, efficient transfer of ions while simultaneously minimizing sources of systematic uncertainties.

3.4.1 Measurement cycle

The mass measurement process with the CPT requires ions to be transferred from their production to their ultimate destination, the final TOF detector. First, the ions produced in the target are delivered to the ion buncher as essentially a continuous beam. After the ions are bunched, they are transferred from one ion trap to another and are stopped at four positions: the ion buncher, the isotope separator, the linear RFQ trap, and finally the precision Penning trap. A set of conditions must exist

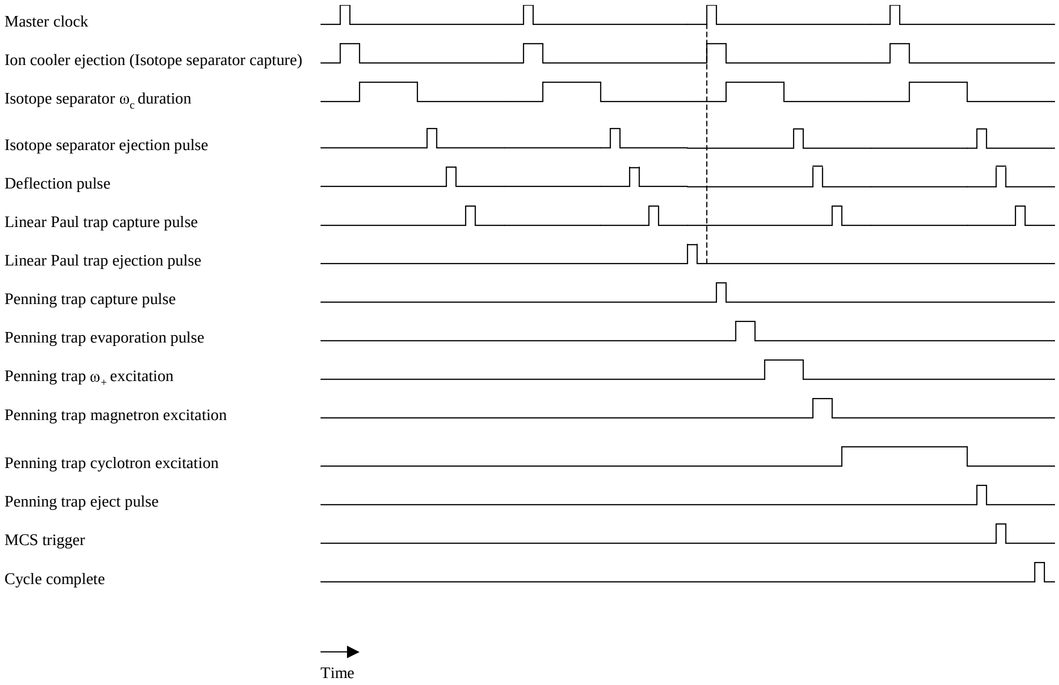

Figure 3.21: Timing diagram (pulse widths not to scale) describing the sequence of events involved in the making of precise mass measurements with the CPT. Notice that, in this case, two ion bunches are accumulated in the linear Paul trap before they are transferred to the Penning trap, and they can be accumulated while the Penning trap is used to make a mass measurement.

before the ions can be ejected from each stopping position. At each stopping position, however, a series of events occurs including the capture of ions into the ion trap and their processing within the trap. This sequence of events, as shown in Fig. 3.21, and their prerequisite conditions establishes a cycle of events which will be described in this section.

The first location where ions are stopped in the CPT system is the ion buncher situated at the end of the ion cooler. Although the ion beam from the ion cooler is continuously injected into the buncher, the ions cannot be ejected from the buncher until the isotope separator is ready to accept them. Since the isotope separator currently processes only one ion bunch at a time, and doesn't accumulate multiple ion bunches, ions can only be injected into the isotope separator after the previous ion bunch held in the separator is ejected. The beginning of the capture pulse occurs simultaneously with the ejection pulse of the ion buncher. However, the duration of the capture pulse is selected based on the time of flight of the desired mass. If the pulse is too short, the ions of the desired mass do not enter; if the pulse is too long, the ions which enter the trap may reflect back out due to the voltages applied at the end of the isotope separator. Once an ion bunch is successfully captured, the mass selection process takes place. At this time, a quadrupole field is applied on the ring electrode for a preset duration. The mass resolved ion bunch is then ready to be ejected from the isotope separator.

A master clock is used to set the ejection rate of the ion buncher. Since the ion buncher can only eject ions as fast as the isotope separator can accept them, the clock is set at a rate just slightly less than the isotope separator rate. At the beginning of each clock cycle, the ejection pulse from the ion buncher is delayed by an amount such that this amount, when added together with the duration of the quadrupole field applied in the isotope separator, is roughly equal to the clock cycle duration.

The linear RFQ trap can accumulate multiple ion bunches and will accept a new ion bunch from the isotope separator when three conditions have been satisfied. First, the previous ion bunch injected into the linear trap must have had sufficient time to cool the ions. With typical pressures of 10^{-4} to 10^{-5} Torr of helium buffer gas, the ions are cooled within 10 milliseconds. Second, the CPT user can select the number of ion bunches to be accumulated in the linear trap. Normally, the number of ion bunches accumulated is set such that the time to accumulate the total number of multiple bunches is just slightly less than the time period of the Penning trap sequence of events. However, since precision mass measurements depends upon the number of ions trapped in the Penning trap (see Section 4.1.2), the number of accumulated bunches can be decreased if more than enough ions have been accumulated. The last condition to be realized is somewhat obvious. Ions cannot enter the linear trap if it is in the process of ejecting the ions. If all three of the above conditions have been met, the linear trap is ready to accept ions from the isotope separator.

Once the ions are ejected from the isotope separator, their transfer is time insensitive until they arrive at the deflection pulse. Here, the start of the pulse is essentially determined by the time of arrival of the desired ions. Since fast MOSFETs are used to switch between the two DC values, the effective delay in the application of the pulse in negligible. The duration of the pulse is primarily set by the time it takes the desired ions to traverse the device. Since the deflection is performed by a one-inch square plate, an ion with A=100 takes approximately 470 ns to travel through the device. As the A=100 ions arrive at the deflection pulse in roughly 70 μs after they are ejected from the isotope separator, the mass resolution of the device is about 0.6 u. After the successful transmission of the ions through the deflection pulse, the ions next encounter the RFQ linear trap.

Two pulses are applied to the linear RFQ trap to capture the ions coming from the isotope separator. One pulse is applied to the deceleration electrode and the other pulse is applied to the first segment of the linear trap. Since the linear trap can accumulate ions, the pulses are not applied until the new bunch of ions have arrived, thereby preventing the already cooled ions in the trap from leaking out. The duration of the capture pulse is determined by the dimensions of the trap, in a similar fashion as the isotope separator. The pulse must be sufficiently long for the ions to enter the trap, yet not as long as for the ions to reflect back out. Once the ions are successfully trapped, they are cooled for a period of time no shorter than 10 ms, and after a preset number of ion bunches have been accumulated, the ions in the linear trap are ready to be ejected.

The next stop for the ions is the precision Penning trap. There are two conditions which must be met before ions can be injected into the Penning trap. First, the previous ion bunch must have already been ejected from the trap, and the second condition is that the linear RFQ trap must have accumulated all the preset number of bunches. The timing of the capture pulse applied to the Penning trap electrodes is arguably more critical than any other timing involved in the CPT apparatus, since an improper timing not only decreases the number of ions captured, but also introduces systematic effects as described in Sec. 4.1.2. For this very reason, the beginning of the capture pulse is not applied until the ion bunch has arrived at the Penning trap, and the duration of the pulse is set to ensure the energy of the ion bunch is not disturbed. Once the ions are trapped, a sequence of events occurs in the measurement process. First, the evaporation pulse is applied which lasts for approximately 500 μs. Next, the contaminant ions are removed with a dipole excitation at the ω_+ frequencies of the undesired ions. The duration of the dipole frequency for each contaminant ion to be removed depends upon the resolution desired. If the contaminant ion is resonant at a dipole frequency close to that of the desired ion, then a higher resolution, and therefore a longer duration of the applied dipole field, is required to prevent the disturbance of the desired ion. Once all the contaminant ions are removed, a dipole excitation at the ω_- frequency is applied, followed by the application of the quadrupole field. All the excitations, from the evaporation pulse to the quadrupole field, are applied one after another with a delay of about 1 ms between each excitation. Following the quadrupole excitation, the ions are ejected from the trap and travel to the MCP detector. Once the ion signal has been recorded by the computerized acquisition system, the computer then sends a signal to signify that the Penning trap measurement cycle is complete, and a new ion bunch can be loaded into the Penning trap.

3.4.2 Tuning

The tuning of the CPT serves to prepare the apparatus in the making of mass measurements of both high precision and accuracy. The following procedure outlines the steps necessary to meet these objectives. The motivation driving the procedure is discussed later in Ch. 4.

Transfer of ions from production to the Penning trap

The first element of the CPT apparatus to be tuned is the rotating target wheel. At first, the position of the spokes in the target wheel are determined with the aid of a scintillator at the entrance of the Enge spectrometer. To avoid the burning of the scintillator, less than 1 electrical nanoamp (enA) of primary beam current is used. With the velocity filter turned off, and the triplet set to approximate settings for the primary beam, a focussed spot will be observed on the scintillator when the ion beam passes through the target. While the wheel is slowly moved by hand, the beam spot will occasionally vanish. At these positions, the beam is striking the spokes of the wheel. These positions, as indicated by a counter, can then be programmed in the CAMAC module which controls the signal sent to the ATLAS beam sweeper. Once the positions have been set, the target wheel can rotate under the power provided by an external power supply and the ATLAS beam will be absent at the target wheel location while a spoke is in the beam path.

The magnetic triplet constitutes the next phase of tuning. The settings for the triplet are first approximated by scaling the magnetic field, which changes almost linearly with the applied current, with the momentum to charge ratio using tuned settings from previous experiments as calibration values. Estimates for the ion momentum are calculated after considering the difference between the initial beam energy, E_{beam}, as measured by the ATLAS operators and the energy loss, E_{loss}, of the ions during their passage through the target. With the energy loss obtained from SRIM-2003 (**S**topping and **R**ange of **I**ons in **M**atter) simulations [43, 44], and the most abundant charge state, q_{max}, determined from code used by ATLAS which determines the charge state distribution of a beam incident upon thin stripper foils, the magnetic field strength of each quadrupole magnet is scaled by noting:

$$B \propto \frac{\sqrt{m(E_{beam} - E_{loss})}}{q_{max}}. \tag{3.4}$$

While the beam spot is still observable on the scintillator, the current of each individual magnetic quadrupole is then more finely tuned to obtain the best focussed spot possible.

Once the scintillator was removed, a PPAC (**P**arallel-**P**late **A**valanche **C**ounter) detector positioned at the focal plane of the Enge spectrograph was quite often used in the first experiments to obtain both spatial and temporal characteristics of the particles entering the spectrograph. This information was deemed to be useful to observe the effect of a gas-filled Enge spectrograph in collecting multiple charge states at the entrance of the gas catcher. As the pressure of the gas inside the spectrograph is varied, and sometimes as the composition of the gas itself is changed, the focus and separation of the desired recoil products from the incident beam could be optimized. However, due to our difficulties in discerning information from the Enge in gas-filled mode with the cases we studied, the gas-filled mode was abandoned for the more easily understood, but usually less efficient, vacuum mode. Since the PPAC detector is not necessary to diagnose the vacuum mode of the Enge spectrograph, and its presence in the spectrograph only increases the energy loss of the ions as they travel through the detector, the PPAC had been removed for future experiments.

Most often the next detector used to diagnose the quality of tuning is the gas catcher itself. The ion current on the cone electrodes is monitored by connecting together the DC inputs of the cone to a picoammeter. (The gas catcher cone RF voltage is first removed so that the small ion current created by ionization of the gas inside the gas catcher can be observed). Most ions lose about 3 MeV within the gas catcher through ionization of the helium buffer gas. Since 40 eV is required in the gas on average to remove the outermost electron from a helium atom, approximately 10^5 electron/ion pairs are created for every ion which enters the gas catcher. The positive ions created are guided to the cone via the voltage gradient along the cylinder of the gas catcher. We therefore expect to detect about 125 enA on the gas catcher cone for every ppA (particle picoampere) of ions entering the gas catcher. To avoid discharges from occurring inside the gas catcher, we normally limit the number of particles entering the gas catcher to 100 ppA or so. Using the gas catcher in this manner, it is used to indicate the number of particles entering the gas catcher.

While the magnetic triplet is still set to focus the primary beam into the Enge spectrograph, the rigidity of the beam is determined as the ionization detected by the gas catcher cone is monitored as a function of the current through the coils of the Enge magnet. If a change in the magnetic field of the Enge results in an increase of current on the gas catcher cone, then more ions must have been focussed into the gas catcher. The rigidity of the beam determined in this manner should be comparable to expectations. If not, then either the ATLAS beam energy, the calculated energy loss through the target, or the charge state distribution is not as predicted.

The effect of the velocity filter can be seen as either the scintillator or the ionization in the gas catcher is monitored for a particular beam charge state. If the results from previous experiments are used as calibration parameters, the electric field to magnetic field ratio of the velocity filter, $\frac{E}{B}$, or equivalently the ratio of the voltage applied on the plates to the current through the coils, scales as the velocity of the ion to traverse the filter undeflected. Since the velocity of the primary beam particles may be quite high, the dispersion of the velocity filter may have to be reduced to operate within the output ranges of the voltage and current supplies. This can be accomplished by decreasing the field strengths while maintaining their ratio. At this stage, the settings of the velocity filter are adjusted only to ensure the beam spot is still centered, and can be verified either by monitoring the scintillator or by maximizing the ionization produced in the gas catcher.

Diagnostic stations further downstream require β activity to effectively tune the rest of the system. Therefore, settings for the triplet, velocity filter, and Enge spectrograph, which have until now been tuned for the primary beam, are scaled for a β-unstable nuclide which is produced in quantities sufficient to enable further refinement of the tuned settings. If the ionization in the gas catcher is monitored while the current through the coils of the Enge spectrograph is adjusted, a hint of the activity may be observed. However, the ionization due to activity may be much smaller than the ionization produced by the scattered beam such that, even after the dispersion of the velocity filter is increased, no sign of activity may be observed. Sometimes, a clear indication of activity transported to the gas catcher isn't realized until the activity is seen at detectors further downstream.

The next diagnostic station is not until after the isotope separator. Here, the detector station, denoted as $1'$, consists of both a MCP and silicon surface barrier (Si) detector. Usually, as a first quick test, the isotope separator is set to fly the ions through to MCP $1'$ just to ensure that ions can reach the detector. Next, the β activity is monitored on Si $1'$ while the effective degrader thickness is adjusted. A complete tune of the degrader is conducted by scanning the Enge field settings for each selected degrader thickness since both are sensitive to the incident ion energy. Next, the parameters of the gas catcher and ion cooler are adjusted. For the most part, the DC voltages do not have to be tuned, except for perhaps those applied to the gas catcher. Only the RF frequencies applied to the different sections in the ion cooler have to adjusted to optimize the transmission of the desired mass. As a first guess, the frequencies applied are scaled by the square root of the mass from a previous tuning; the transmission of ions with A=25 requires the frequencies of the ion cooler to be twice that for A=100 ions. Sometimes the application of the desired frequency results in a lot of feedback, or reflected power, into the amplifier. In these cases, the voltage of the applied waveform is adjusted instead of the frequency, with the voltage scaling as $1/m$. Overall, observing the results of the tuning on Si $1'$ is cumbersome for long-lived activity, so tuning to the Si detectors is performed with short-lived nuclides.

Once the ion cooler RF voltages, the gas catcher DC settings, and the degrader are tuned to maximize the activity seen at Si $1'$, the isotope separator can be set to capture the ions from the ion cooler. At this time, the ions are kept in the isotope separator for about 10 ms which is sufficient to cool the ions, but not long enough for the ions to be lost inside the trap. The capture efficiency is verified by comparing the amount of activity seen at Si $1'$ with these settings to the amount seen when the isotope separator is set to fly the ions through to Si $1'$. If the efficiency is low, the timing of the capture pulse could be the culprit. The end of the capture pulse applied to the isotope separator electrodes is scaled from a previous tuning by the square root of the mass; the timing for ions with A=25 is two times less than for A=100 ions. Further tuning can be carried out at the next detector station.

The beam is transported to the detector station labelled as $2'$, which contains both a MCP detector and Si detector. Normally, the MCP detector is first used to diagnose the tuning of the voltages applied to the steerers and lenses between detector stations $1'$ and $2'$. Since the settings are not expected to significantly change with time, only a fine tuning to maximize the signal area on the MCP is necessary. At this point, the transmission between $1'$ and $2'$ is checked by comparing the signal detected on Si $1'$ to that on Si $2'$. Since the Si detectors have identical active areas and the foil in front of the detector is positioned at an identical distance from the active area, the solid angle acceptance of each detector is roughly the same. In addition, the thicknesses of the detectors are identical, so the efficiencies of the two detectors are also similar under the assumption that the same bias voltage is used for both detectors.

The isotope separator is ready to be tested in a mass selective cooling mode. Ions of the desired mass are first identified at MCP $2'$ by their time of flight to the detector. Initially, the duration of the applied quadrupole field is set to a moderate value of about 100 ms. The cyclotron frequency is scaled as m^{-1} from a previous tuning, and since the pressure of the helium buffer gas is essentially immutable, the voltage of the applied quadrupole field scales as the charge to mass ratio of the desired ions. With the isotope separator set at low resolution, the intensity at each mass number, as detected by the MCP, is dominated by the most abundant species which is typically that of a molecule. As the cyclotron frequency of one mass, or molecule, is selected, the signal area on the MCP increases for that particular mass. To get a higher mass resolution and a better determination of the cyclotron frequency, longer excitation times are required.

Once a mass resolving power of at least m is achieved, the amount of activity at m u is determined at Si $2'$. At this stage, the most abundant species of mass m which β decays is tuned by refining the settings of the triplet, velocity filter, Enge spectrograph, degrader, and isotope separator. The parameters are not expected to change significantly, but as the amount of activity for a particular mass increases, smaller effects are noticeable.

The transfer of the ions to the next detector, MCP 1, can be tuned by adjusting the various steerers and lenses while the deflection pulse is off. 'Off' in this case means that all electrodes which form the deflection pulse are at drift tube potential. Then, as MCP 1 is monitored, the DC potential of the deflection pulse is adjusted until no ions are detected. Once the deflection pulse is turned on, a wide pulse width allows the pulse amplitude to be adjusted until all the ions previously seen at MCP 1 are detected once again. The pulse width is then adjusted to permit only the desired mass to be transferred to MCP 1. Normally, the voltages applied to the deflection pulse have already been set, and the timing of the pulse itself is the only parameter to be adjusted and is scaled as the square root of the mass. Once the pulse is applied, some steering and focussing may be necessary once again. Since a Si detector does not exist on the same feedthrough as MCP 1, a measurement of activity is postponed until the next detector station.

Maximizing the signal at MCP 3 is the next step in the tuning process. Once the timings of the capture pulses applied to both the deceleration and S1 electrode have been scaled for the desired mass number, ie: $m = \mathrm{A}$ u, fine adjustments of these parameters can be made while the change in the signal at MCP 3 is observed. A further increase in the transmission to MCP 3 is sometimes achieved after the tuning of steerers and lenses. If the deflection pulse is set to permit the transmission of only one particular mass, the amount of β activity at such mass can be measured at

Si 3. To assure the detected activity represents ions successfully captured and ejected from the linear trap, the ejection pulse can be removed. If any amount of activity is detected at Si 3 while the ejection pulse is removed, then the capture of the ions is not done properly. Some adjustments to the capture pulse timing or the potentials of the trap itself may be necessary.

The combination of the isotope separator and deflection pulse allows a measure of activity at Si 3 as a function of mass number which could not be achieved as precisely with the other Si detectors. Because of this, a final refinement of the parameters for the triplet, velocity filter, Enge, degrader, gas catcher, ion cooler, and isotope separator is made to maximize the transfer of ions with mass $m = \mathrm{A}$ u. At this point, the parameters have been set for the most abundant isobars detected at Si 3. The efficient transfer of a particular nuclide is then achieved by scaling all the previously tuned parameters for any differences from the most abundant nuclide tuned to Si 3. Generally, little change is required unless the desired nuclide which emerges from the target has a different charge state from the most abundant isobar tuned to Si 3. Sometimes, small adjustments to the degrader thickness are required as different elements lose different amounts of energy through the target and degrader.

In summary, an efficient transfer of ions from the target to the Penning trap requires careful tuning. Once the settings have been established for a particular nuclide, the devices can be scaled for transfer of the desired ions: the magnet settings for the triplet and Enge scale as p/q; the parameters for the velocity filter scale with the velocity; the frequencies used to confine the ions in the cooler scale as the square root of the mass; the capture pulse timings of all traps, including the deflection pulse timing, also scale as the square root of the mass; and the amplitude of the quadrupole field in the isotope separator scales with the cyclotron frequency ($\propto q/m$) of the ions.

Tuning the trap

The precision Penning trap is both mechanically and electronically stable such that very few changes are required from one experiment to another. However, for the most precise and accurate measurements, a number of procedural steps in preparation for the measurement are necessary. Most of the steps outlined in this section can be performed prior to an online experiment given a source of ions, but the following discussion assumes the Penning trap needs to be tuned online.

A full conversion from an initially pure magnetron motion to a reduced cyclotron motion results in the most precise and accurate measurements. Therefore, ions injected into the Penning trap must not have any initial cyclotron motion which requires that the ions must be carefully steered and focussed into the Penning trap. If the Penning trap is set to fly the ions through to the final MCP detector, the number of ions with little, if any, cyclotron motion can be determined. The voltage of the upper endcap and correction tube can be raised to provide an obstacle, or stopping potential, for ions with cyclotron motion. Since energy is conserved, and all the ions ejected from the linear trap have essentially the same energy, those ions with some energy in the form of cyclotron motion will have less axial energy to surpass the stopping potential. For a given stopping potential, the steerers and lenses are adjusted to maximize the number of ions detected at the MCP. The voltage of the stopping potential is increased, and the steerers and lenses are adjusted again. Maximizing the signal at the MCP detector by adjusting the steerers and lenses ensures the ions are injected along the central axis of the magnetic field, and will therefore yield ions with little cyclotron energy.

The next step is the capturing of the ions. With capture pulse timings from other experiments taken as reference values, both the beginning and end of the pulse are scaled as the square root of the mass. Further refinement of the pulse timing is obtained as the properties of the TOF spectra are observed as a function of the capture pulse timing (see Sec. 4.1.2).

The parameters for both the evaporation pulse and the magnetron excitation do not require any tuning. Although the magnetron motion is relatively mass insensitive, the parameters which describe a magnetron excitation for ions of one mass may need to be changed if ions of a widely different mass are used. Sometimes ions are lost if the amplitude (or time) of the magnetron excitation is too large. If ions are lost, then the amplitude of the excitation is decreased.

Removal of contaminant ions is important for accurate mass measurements. The tuning of the reduced cyclotron motion involves the determination of three parameters: the duration, amplitude, and frequency of the excitation. A good first approximation for the frequency of each contaminant ion is obtained from the difference between the cyclotron (which is inversely proportional to the mass) and magnetron (which is relatively mass insensitive) frequencies. A more precise determination of each frequency is obtained by determining the position of the minima in a TOF spectra, identical to the procedure of determining the cyclotron frequency but generated with a dipole excitation instead. The duration and amplitude of the excitation is chosen to satisfy the desired precision. When the reduced cyclotron frequencies are used to remove contaminant ions, the duration of the dipole excitation should be as short as possible with enough power to remove as many contaminant ions as possible. However, the resolution of the applied dipole field should be sufficiently high so as not to disturb the ions whose mass is to be measured. A complete study of the reduced cyclotron motion therefore requires a measurement of the number of ions removed and the influence of the excitation on an ion species of similar mass. The first step in this study is to identify the reduced cyclotron frequency of a contaminant ion which is closest to the reduced cyclotron frequency of the ion species whose mass is to be measured. The difference in frequency, $\Delta\nu$, determines the required resolution. Second, the dipole frequency of the most abundant contaminant ion, ν, is applied with a duration estimated to meet the required resolution. The number of ions removed as a function of the excitation amplitude is recorded, which is more easily conducted with an initially pure sample of ions in the trap. Eventually, an amplitude is reached in which no more ions are removed. This amplitude would be the ideal amplitude to remove contaminant ions from the trap unless results from the third test suggest otherwise. The third test involves the application of a dipole excitation with similar duration at a frequency ν' whose difference from the dominant ion species is identical to the frequency difference determined earlier, ie: $\nu' = \nu - \Delta\nu$. Measurements of the TOF baseline of the dominant ion species are noted as a function of the excitation amplitude. As the amplitude increases, the TOF baseline will eventually decrease since the ions gain energy from the excitation due to the decrease in resolution. The last two steps are repeated for other durations until parameters are found which will remove contaminant ions yet leave the desired ions undisturbed.

Tuning the correction electrodes (both correction tube and correction ring electrodes) is achieved by monitoring the TOF spectra generated from dipole excitations at the reduced cyclotron frequency of some particular ion species. Dipole excitations at the reduced cyclotron frequency are used since a TOF effect can be observed and the dipole excitations are much more sensitive to the electric potential than the quadrupole excitations are. Although the voltages required for the correction electrodes can be approximated by tuning with short dipole field durations, a more precise tuning is achieved with longer excitations. In any case, the capture pulse timing, evaporation pulse, and removal of all contaminant ions should all be tuned and applied prior to the application of the dipole field excitation.

Once the parameters for the removal of contaminant ions are determined, the only remaining parameters to determine are those which describe the quadrupole excitation. For a given excitation time, the amplitude of the applied quadrupole field is selected to ensure a complete conversion between the magnetron and reduced cyclotron motion when the frequency of the applied excitation is the cyclotron frequency of the trapped ions. The depth of the main peak in the TOF spectra will be greatest when the correct amplitude is chosen. A quick test to ensure the appropriate excitation amplitude was determined is to double the hypothesized amplitude and verify that the main peak disappears; a symmetric double-peaked structure will appear.

3.4.3 Software and cycling hardware

No modern instrument is operated without a combination of hardware and software to acquire data, perform basic calculations, and display the results of the processed data. The CPT is no exception. Optimizing the performance of the CPT requires some processing of the data with instant feedback, without the experimenters first having to analyze data off-line. An instant display of the acquired data also maximizes the use of valuable beamtime as problems can be detected as they arise. Computer automation of a system like the CPT is also faster, and minimizes human error which inevitably occurs for complex apparatuses requiring multiple or frequent adjustments. All of the aforementioned conditions were considered when the computer software used to control the CPT was designed. The resulting automation of the CPT system is fast and accurate, and ensures an efficient collection of data with minimal human error. A description of the CPT software in terms of its ability to acquire data, conduct simple analysis, and display the results is discussed in this section. In addition, the hardware specialized to control each measurement cycle will also be presented.

Acquisition

The portion of the CPT software used to acquire data can be divided into three parts. The first part involves the loading of parameters to the hardware devices. The cycle of events constitutes the second part. Extraction and storage of the data describes the third part. All three parts are critical and are described below.

Different terms are used to describe the cycling process. One injection, and subsequent ejection, of ions from the Penning trap is defined as a ‘point’. A series of such points, each point corresponding to a particular frequency of the electric field applied to the Penning trap, constitutes a span of frequencies referred to as a ‘scan’. An arbitrary number of scans can be analyzed together, forming a ‘group’. The entire collection of data which is recorded in one data set is defined as a ‘run’. A typical run consists of 31 points per scan, and many scans are taken until the desired statistics are accumulated.

The sequence of events during each ‘point’ or ‘scan’ is controlled with the combination of hardware and software such that the conditions from Sec. 3.4.1 are satisfied. Acquisition parameters, including those which describe the field excitations in the Penning trap and the precision timing required to capture and eject ion bunches in/from the various traps, are not changed during a measurement run, but they are often adjusted between runs and during the tuning process described in Sec. 3.4.2. To simplify the loading of the parameters to the multitude of devices, the user only needs to load into the acquisition program one control file which contains all commonly adjusted parameters. One window of such a control file is shown in Fig. 3.22. Currently, the user can change any number of parameters within the file, but upon loading the parameter file into the program, all hardware devices are reloaded and not just the devices with modified parameters. The control file should also be stored along with the generated data, but this option will not be implemented until the next version of the software.

The CPT software is used to program the cycling hardware which applies the actual voltages to the various devices. All waveforms applied to the precision Penning trap are provided by SRS DS340 or SRS DS345 function generators, but the one used to apply a quadrupole field scan deserves special mention. It contains an ovenized AT-cut oscillator to increase the frequency stability of the generator to better than 1 ppb per day and its 10 MHz clock is used as a reference timebase for the other generators which provide the magnetron and reduced cyclotron frequencies. In addition, the output of the generators which provide the dipole and quadrupole field excitations are processed through two more modules. One module, termed the phase splitter,

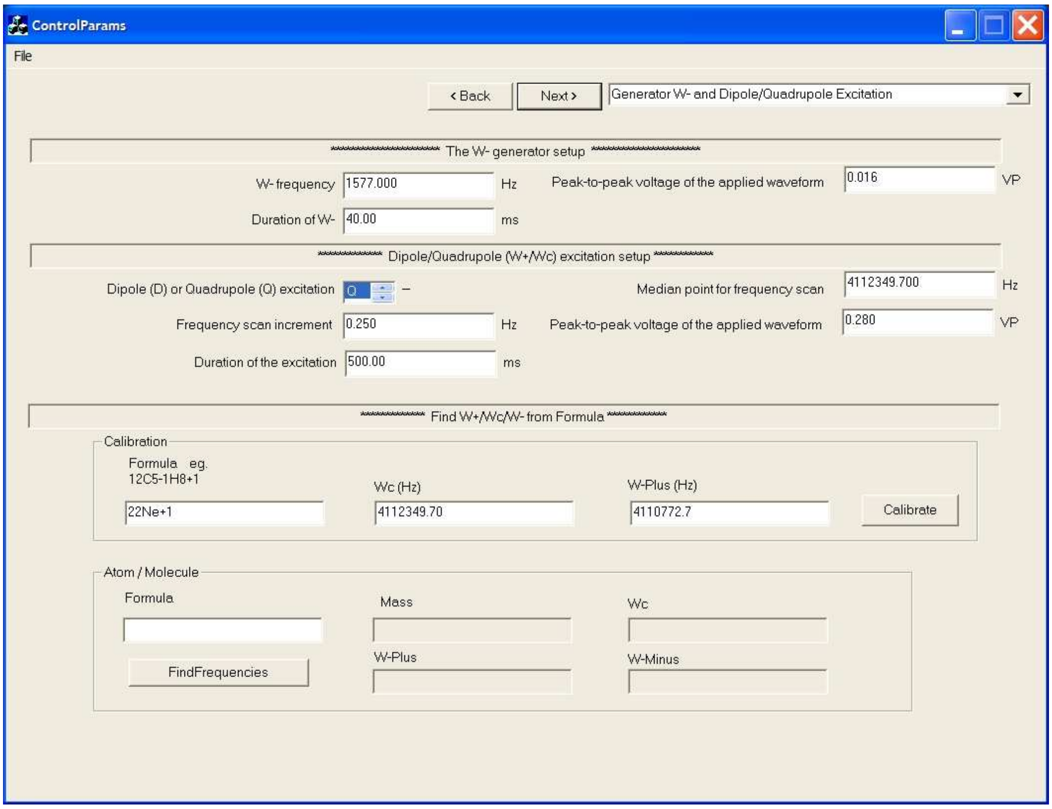

Generator W- and Dipole/Quadrupole Excitation

The W- generator setup

W- frequency 1577.000 Hz

Peak-to-peak voltage of the applied waveform 0.016 VP

Duration of W- 40.00 ms

Dipole/Quadrupole (W+/Wc) excitation setup

Dipole (D) or Quadrupole (Q) excitation Q –

Median point for frequency scan 4112349.700 Hz

Frequency scan increment 0.250 Hz

Peak-to-peak voltage of the applied waveform 0.280 VP

Duration of the excitation 500.00 ms

Find W+/Wc/W- from Formula

22Ne+1

Wc (Hz) 4112349.70

W-Plus (Hz) 4110772.7

Figure 3.22: One window of the interface used to control the cycling parameters.

provides an additional waveform with equal amplitude but 180° difference in phase. The other module applies the appropriate phase to each ring segment of the Penning trap, for both dipole and quadrupole excitations. Precision timings, such as those required for the capture pulses applied to the linear trap and Penning trap, are controlled by Data Design Corporation DG11A Digital Delay Generators which have 10 ns resolution. The durations of the field excitations applied to the Penning trap, which do not require the same magnitude of precision, are controlled by Jorway 221 Timing and Sequence modules which have 10 μs resolution. Other timing sequences, such as that required for the deflection pulse, are currently controlled by Phillips 394 Quad Gate and Delay Generators, but efforts are underway to automate these timings as well.

As ions strike the MCP detector, the generated signal is first amplified, then digitized, and subsequently sent to the LeCroy 3521A multi channel scalar (MCS) module. Upon a trigger signal, the MCS counts the number of signals (ions) it receives in the first channel until the MCS is instructed to advance to the next channel, at which point it counts the number of signals it receives in the second channel, and so forth. The channel advance rate is determined by a ÷N counter fed by a 1 MHz clock. Typically, the counter is selected to be a ÷4 counter, which dictates that the channel advance rate is 250 kHz. In this case, the dwell time for each channel is 4 μs. A total of 256 channels, representing a time-of-flight window of 1.024 ms, is recorded and is stored in a LeCroy 8206A Memory Module. After each scan, the data recorded and stored for each point within the scan is transferred to the computer for further analysis.

Analysis

The raw data downloaded to the computer at the end of each scan is stored in the software as a two-dimensional array with each entry representing the number of ions detected for a specific MCS channel (or equivalently, time) and point (or equivalently, excitation frequency). At this time, the software does some preliminary analysis by sorting the acquired data into four additional arrays, or tables, determined by the number of ions detected for each point. The tables are then used to generate spectra which are displayed as described on p. 94. TOF spectra are generated from the tables in which the average MCS channel number (or equivalently, time of flight) for each excitation frequency and its standard deviation are calculated and are updated at the end of each scan.

Different functions are available to fit the various spectra. The software used online offers a choice of two functions: the Gaussian and Sinc functions. The software used off-line to analyze the data currently has a selection of three fiting functions: the Gaussian and Sinc functions in common with the online program, and a modified Sinc function which more accurately represents the expected theoretical lineshape of the TOF spectra. Each fitting function has a number of free parameters used to generate a fit and the off-line program allows any or all of these parameters to be fixed at values chosen by the user.

The Gaussian function exists for historical reasons and was used to provide a first order estimate of the resonant frequencies. Four parameters are used to describe the fit: the baseline, b; the amplitude, a, which is the difference between the baseline and the minimum in the spectra; the frequency, μ, corresponding to the minimum in the spectra; and the full width at half the maximum amplitude (FWHM), Γ. These parameters are used to describe the Gaussian function, P_G, defined as:

$$P_G = b - a \cdot \exp\left[-\left(\frac{x-\mu}{0.6006\Gamma}\right)^2\right] \tag{3.5}$$

for excitation frequencies, x. This function should be familiar once it is realized the standard deviation σ is related to the FWHM ($\Gamma = 2.354\sigma$).

The Sinc function, P_S, is the most commonly used function during online accumulation of data. Four parameters, identical in description to the Gaussian function, are used to generate a fit as described by:

$$P_S = b - a \cdot \left| \frac{\sin[(x-\mu)(3.79/\Gamma)]}{(x-\mu)(3.79/\Gamma)} \right| . \tag{3.6}$$

This function more closely resembles the observed time of flight as it is based upon the radial energy gain expressed in Eq. 2.84, but neglects the k_o^2 term in ω_B. The factor of 3.79 was chosen to allow Γ to represent the true FWHM of the function.

The third generation of fitting functions is the modified Sinc function, P_{MS}, described by:

$$P_{MS} = b - a \cdot \left\{ \frac{\left| \sin\left[(0.89/2\Gamma)\sqrt{4\pi^2(x-\mu)^2 + (c\pi\Gamma/0.89)^2} \right] \right|}{(0.89/\pi\Gamma)\sqrt{4\pi^2(x-\mu)^2 + (c\pi\Gamma/0.89)^2}} \right\}, \tag{3.7}$$

whereby the Sinc function was changed to better reflect the energy gain profile expressed by Eq. 2.84, including the k_o^2 term in ω_B. The extra parameter, c, was introduced to account for cases when a full conversion between the magnetron and reduced cyclotron motions was not properly executed. As such, $k_o = \frac{c\pi}{t_{conv}}$ where $c = 1$ for a complete conversion.

A comparison of all three generations of fitting functions was made after fitting a subset of data used in Ref. [39]. The maximum difference in the frequency ratios determined from this data set was 23 ppb, but the uncertainty in the ratios were 53 ppb, 28 ppb, and 28 ppb for the Gaussian, Sinc, and modified Sinc functions respectively. The fitting functions therefore give similar results, but those produced with the Sinc and modified Sinc functions yield smaller uncertainties. For all data reported in this thesis, the modified Sinc function was used and any possible systematic effects resulting from the fits were checked periodically by comparing mass ratios of established well-known masses.

Display

A windows interface, as seen in Fig. 3.23, is used to control the acquisition and display results of the acquired data. As data is downloaded to the computer, the display is

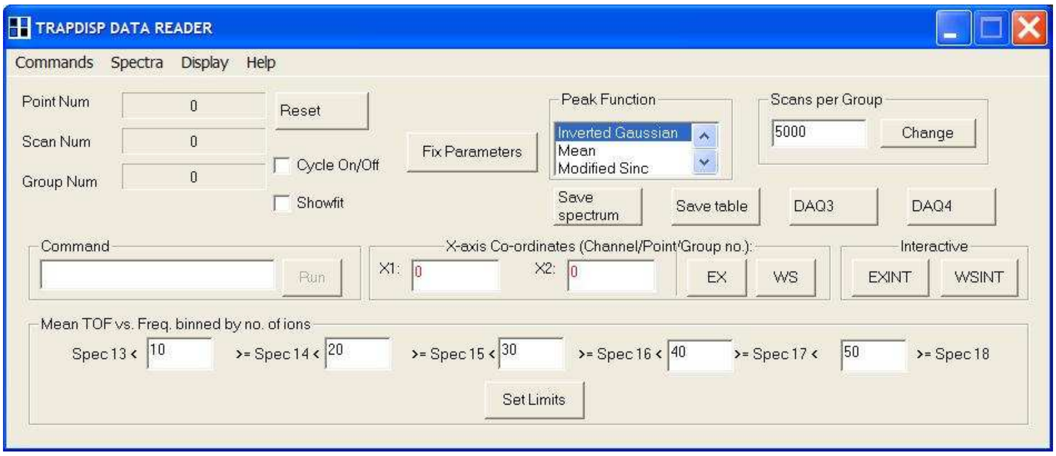
TRAPDISP DATA READER

Point Num 0

Scan Num 0

Group Num 0

☐ Cycle On/Off

☐ Showfit

Peak Function: Inverted Gaussian

Scans per Group: 5000

X-axis Co-ordinates (Channel/Point/Group no.): X1: 0 X2: 0

Mean TOF vs. Freq. binned by no. of ions

Spec 13 < 10 >= Spec 14 < 20 >= Spec 15 < 30 >= Spec 16 < 40 >= Spec 17 < 50 >= Spec 18

Figure 3.23: A picture of the CPT software interface.

constantly updated and the user has a wide selection of graphs and histograms to view. Presently, eleven spectra are available and are summarized in Table 3.7.

Table 3.7: Various spectra are available to monitor the collection of data. Listed are the eleven spectra currently in use. Most of the spectra can be classified in two groups: MCS spectra, and TOF spectra. The MCS spectra are graphs with the number of detected ions plotted as a function of the MCS channel in which they were detected. The TOF spectra display graphically the average time of flight as a function of excitation frequency.

Spectra	Purpose
1	Accumulated MCS spectra for an entire run.
2	The MCS spectra for the current point.
3	The TOF spectra for the current group and is updated at the end of each scan.
4	The TOF spectra for the current run and is updated at the end of each group.
5	Total number of ions for four consecutive points as a function of every fourth point.
6	The total number of ions accumulated for the current group as a function of the excitation frequency.
7	The central frequencies for each group plotted during the run.
8	Not used.
9	The TOF spectra for the current group with data comprised of only those points with less than 40 ions detected.
10	The TOF spectra for the current group with data comprised of only those points with less than 80 ions detected.
11	The TOF spectra for the current group with data comprised of only those points with less than 120 ions detected.
12	The TOF spectra for the current group with data comprised of only those points with greater than 120 ions detected.

Chapter 4

Measurements and results

> *It is the mark of an educated mind to rest satisfied with the degree of precision which the nature of the subject admits and not to seek exactness where only an approximation is possible.*
>
> Aristotle (384 BC - 322 BC)

4.1 Precision versus accuracy

An optimum measurement of any kind, including a mass measurement, is one which is both precise and accurate. The precision of a measurement is obtained purely from statistics and is a measure of how well the result has been determined. Accuracy refers to how correct, or true, the measurement is. This section will describe the techniques used to obtain both precise and accurate measurements with the CPT mass spectrometer.

4.1.1 Maximizing precision

The success of most experiments depend, to a large extent, upon the degree of precision achieved. For CPT mass measurements, the mass precision as defined by Eq. 2.99 can be expressed as:

$$\frac{\delta m}{m} = \frac{m}{qB}\delta\omega_c. \tag{4.1}$$

An empirical formula has been suggested by Ref. [45] which relates the uncertainty in cyclotron frequency to the resolving power P and the number N of detected ions:

$$\delta\omega_c = \frac{C}{P\sqrt{N}} = \frac{C}{t_{RF}\sqrt{N}}, \tag{4.2}$$

in which C is a dimensionless constant but depends upon the function used to fit the resonance TOF spectra and the number of both the desired and contaminant ions. If Eq. 4.1 is combined with Eq. 4.2, the mass precision is then given by:

$$\frac{\delta m}{m} = \frac{m}{qB}\frac{C}{t_{RF}\sqrt{N}}. \tag{4.3}$$

As the strength of the magnetic field affects the mass precision which can be obtained, the strongest magnetic field which is both temporally stable and homogeneous within the ion trap volume is the best choice. Other ways to increase the precision are to use longer excitation times, use nuclides of higher charge states, improve the spectra and fitting function to decrease C, and obtain more statistics.

In the CPT apparatus, the ions are subjected to a buffer gas cooling before they are transferred to the Penning trap. The resulting charge state of the ions is therefore related to the difference in electron ionization energies between the nuclides and the buffer gas. With helium as the buffer gas, most nuclides will be left in a 1+ or 2+ charge state. Because the mass precision is affected by the charge state of the measured ions, it is partially determined by the interaction between the stopped ions and the gas.

The ultimate mass precision which can be achieved with the CPT depends upon the half-life of the nuclides studied and the total number of ions which are detected. For this reason, the apparatus must transfer short-lived, weakly-produced nuclides from their production to the Penning trap in an efficient and timely manner. If t_{total} is the total time permitted to make a mass measurement, then from Eq. 4.3, the precision achieved:

$$\frac{\delta m}{m} = \frac{m}{qB}\frac{C}{t_{RF}}\sqrt{\frac{t_{pp}}{n_{pp} \cdot t_{total}}} \tag{4.4}$$

with t_{pp} representing the time per point or measurement cycle, and n_{pp} is the number of ions detected per point. The time per point includes the time t_m to establish the magnetron motion, the time t_c to remove all contaminant ions in the precision Penning trap, and the time t_{RF} for the application of the quadrupole field. The number of ions at the end of each measurement cycle, then, can be determined with:

$$n_{pp} = \epsilon n_a e^{-\lambda(t_m + t_c + t_{RF})} \tag{4.5}$$

with n_a representing the number of ions injected into the Penning trap per cycle, ϵ is a factor to describe the efficiency of the measurement process, and λ represents the decay constant of the measured nuclides. (See Appendix C for background information regarding radioactive decay.) Assuming the ions of interest are produced at a constant rate R and are accumulated in the linear trap for the entire time during a measurement cycle, the number of ions accumulated:

$$n_a = \frac{R}{\lambda}[1 - e^{-\lambda(t_m + t_c + t_{RF})}] \tag{4.6}$$

from Eq. C.6. If the times for the application of the various excitation modes can be rewritten in terms of the decay constant such that:

$$\lambda(t_m + t_c) = a \tag{4.7a}$$

$$\lambda(t_{RF}) = b \tag{4.7b}$$

producing dimensionless parameters a and b, then after substituting Eqs. 4.6 and 4.5 into Eq. 4.4, the mass precision obtained can be expressed as:

$$\frac{\delta m}{m} = \frac{m}{qB} \frac{C}{\sqrt{\epsilon R}} \frac{\lambda}{\sqrt{t_{total}}} \left\{ \frac{1}{b} \sqrt{\frac{a+b}{[1 - e^{-(a+b)}]e^{-(a+b)}}} \right\}. \tag{4.8}$$

The dependence of the precision on the parameters a and b are shown graphically in Fig. 4.1. In the interest of better visualizing this dependence, the precision in Fig. 4.1 is defined as $\frac{m}{\delta m}$ which produces a smaller range of values compared with the definition previously adopted. Each curve shows how the precision depends upon b for particular values of a. One can easily see that the best precision is obtained when no time is spent for magnetron or reduced cyclotron excitations ($a = 0$). In this case, the optimum precision is achieved with $b \sim 1.4$ such that:

$$t_{RF} = \frac{b}{\lambda} = b \cdot \frac{t_{1/2}}{\ln(2)} \sim 2\ t_{1/2} \tag{4.9}$$

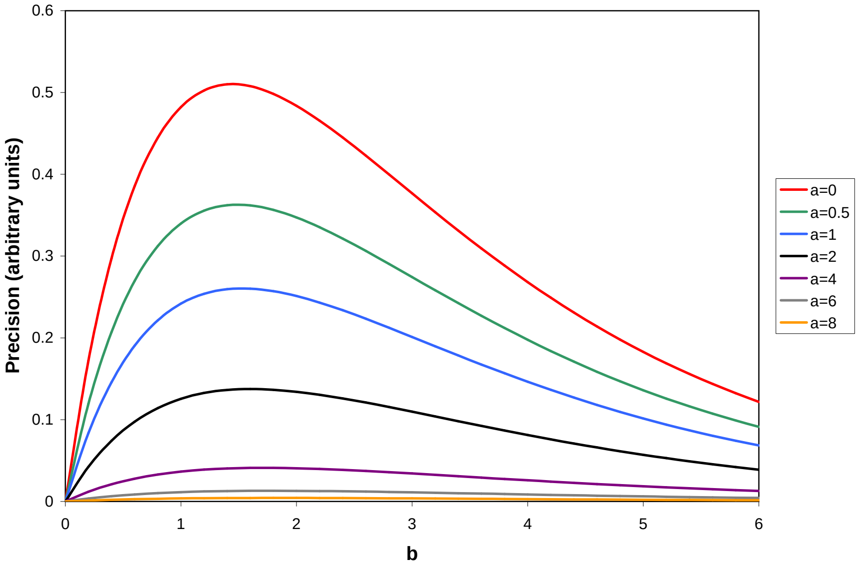

Figure 4.1: The mass precision as a function of the duration of the quadrupole excitation. For graphical purposes, the precision plotted here is inverse to the convention in the text (ie: precision $= \frac{m}{\delta m}$). The parameter b is defined by Eq. 4.7b. Each curve represents the change in the precision as a function of the parameter b for various values of a as defined by Eq. 4.7a.

from Eq. 4.7b. In the extreme situations when a lot of time is required to clean undesired nuclides from the precision Penning trap, the optimum precision is obtained with $b \sim 1.8$ which suggests $t_{RF} \sim 2.6\ t_{1/2}$. Therefore, the act of discarding undesired ions before they are injected into the Penning trap provides the best possible situation in obtaining the ultimate mass precision.

The above arguments are somewhat simplistic in that they suggest the optimum mass precision of a stable nuclide is obtained with the application of the quadrupole field for an infinitely long time. For practical reasons, obviously, such exposures are impossible. Furthermore, the contribution of systematic effects to the final mass uncertainty must also be considered. Our experience has shown that, for our present set up, field excitations of about two seconds provides the lowest mass uncertainty. Thus, for our purposes, Eq. 4.8 holds for nuclides with half-lives shorter than about one second. Even though all nuclides reported in this chapter have half-lives longer than one second, field excitations shorter than two seconds were generally used due to the effects discussed below.

The derivation of Eq. 4.8 was made under the assumption that 100% of the contaminant ions could be removed from the Penning trap without disturbing the ions of interest. In reality, the CPT never achieves this level of contaminant removal. Since the TOF depths of the cyclotron resonance spectra are affected by the simultaneous presence of contaminant ions with the desired ions, the mass precision will depend upon the efficiency of the cleaning process. In addition, the application of a dipole field to remove an ion species with a mass close to the dipole resonance of the desired ions can unwantedly give energy to the desired ions. The effect is a reduction in the TOF baseline which also decreases the mass precision obtained. Therefore, the act of removing the contaminant ions prior to their injection into the precision Penning trap is a primary objective of the CPT apparatus.

Overall, the optimum mass precision is obtained with highly-charged ions exposed to field excitations within a strong homogeneous magnetic field for durations equal to twice the ion's half-life, assuming any undesired ions are removed prior to their injection into the Penning trap. A Penning trap apparatus, now in construction at the TRIUMF facility, plans to take advantage of the gain in mass precision from highly charged ions by utilizing a charge state breeder (see Ref. [46] for a recent review on EBIS devices) to provide ions with higher charge states before they are injected into the precision Penning trap TITAN [19]. In this manner, as shown by Eq. 4.3, it is hoped that the precision in the mass currently achievable for nuclides with half-lives greater than 50 ms may be obtainable with nuclides having half-lives as short as a few milliseconds. Unfortunately, the loss of activity during the lengthy preparation of the ion samples may offset any gain in precision from using higher charge states. If this is true, then the TITAN approach may be viable only for longer-lived isotopes. Ultimately, however, the uncertainty in the mass is limited by the contributions of systematic effects which are discussed in the next section.

4.1.2 Minimizing systematic effects

Systematic effects also limit the accuracy of mass determinations. The magnitude of these effects are only determined after a careful series of measurements are made under similar conditions at various times. Certain effects, such as those resulting from the number of ions trapped in the Penning trap in each ion bunch, the number of undesired ions in each ion bunch, and the timing of the pulse used to capture the ion bunch, can be minimized during each measurement cycle. Other effects, such as the stability of the magnetic field, must be monitored over a longer period of time. In addition, systematic effects can arise from inherent defects in the construction of the apparatus. Only a summary of the various systematic effects will be presented here. More detail can be found in Refs. [30, 31, 47].

A discussion of the possible sources of systematic error (ion number, presence of contaminants, magnetic field stability, mass effects, capture pulse timing) will be provided. The results of these studies will be presented in the sections describing the measurements that were made, as tests of systematic effects were generally conducted during each set of measurements. However, in some cases, such as the effects stemming from the presence of contaminants or inaccurate capture pulse timing, the studies were performed on a series of measurements which will not be included in this thesis (fission source – contamination effects; ^{22}Mg – capture pulse timing). For these specific cases, the results of these tests will be presented in this section if necessary.

From Eq. 2.41, the mass of a specific ion not only requires a precise measurement of the cyclotron frequency of the desired ion, but also demands knowledge of the charge state of the ion and the strength of the magnetic field. The charge state of the ion is selected by an appropriate tuning of the capture pulse timing for each ion trap. Most of the ions studied here were produced most abundantly in a singly-ionized state. The strength of the magnetic field, is determined with a measurement of the cyclotron frequency of a well-known mass. Given a reference mass m_{ref} with cyclotron frequency $\omega_{c,ref}$ and charge state q_{ref}, the ratio of the unknown, but desired, mass m to the reference mass is expressed as:

$$\frac{m}{m_{ref}} = \frac{qB}{\omega_c}\frac{\omega_{c,ref}}{q_{ref}B} = \frac{q}{q_{ref}}\frac{\omega_{c,ref}}{\omega_c}. \tag{4.10}$$

The most precisely known masses are listed in [48] and include ^{14}N, ^{16}O, and ^{1}H. The nuclide ^{12}C, whose mass is defined as 12 u, would be the ideal reference to use except that most of the isotopes studied are much heavier than carbon and the large mass difference between the two could potentially introduce systematic effects as described later. Instead, the best calibrant masses to use are of molecules of similar mass to the desired ions with ^{14}N, ^{16}O, ^{1}H, and ^{12}C as constituents.

Due to the nature of the Penning trap, the cyclotron frequencies obtained are of ions, and not of neutral atoms. A determination of the final atomic mass of each isotope investigated therefore requires the addition of the mass(es) of the missing electron(s) and its(their) binding energy(ies). The electron mass of 511 keV contributes a significant portion to the atomic mass in comparison with the 10 keV mass precision typically obtained. However, the binding energy of an electron is on the order of 8 eV, which is negligible. Molecules, like C_5H_8, were often used to calibrate the strength of the magnetic field. The mass of these molecules was calculated by the addition of the constituent atoms, neglecting the $\sim$ 40 eV contribution from both the enthalpy of formation and the electron binding energy. In all measurements reported here, both the enthalpy of formation and the electron binding energies are considered negligible.

Deviations from the ideal Penning trap, including the truncation of the infinite hyperbolic electrodes, introduce systematic effects which are dependent upon the mass of the ion being investigated. The practical Penning trap must include slits in the central ring electrode to enable the application of azimuthally symmetric dipole and quadrupole fields. In addition, apertures in the endcap electrodes are necessary for ions to be injected into and ejected from the trap. All of these modifications introduce imperfections in the electric quadrupole field as defined in Eq. 2.44. The most significant contributions arise from the addition of octupole and dodecapole terms to the electric field. If the coefficients of these terms are C_4 and C_6 respectively, then the shift in the cyclotron frequency, $\Delta\omega_c$, resulting from these terms is given by:

$$\Delta\omega_c = \frac{\omega_+\omega_-}{\omega_+ - \omega_-}\left[\frac{3}{2}\frac{C_4}{d^2}(\rho_-^2 - \rho_+^2) + \frac{15}{4}\frac{C_6}{d^4}(\rho_z^2(\rho_-^2 - \rho_+^2) - (\rho_-^4 - \rho_+^4))\right], \qquad (4.11)$$

where ρ_-, ρ_+, and ρ_z are the amplitudes of the magnetron, reduced cyclotron, and axial motions respectively. Now with the frequency relations given by Eqs. 2.41, 2.52, and 2.59, the term outside the square brackets can be approximated such that:

$$\frac{\omega_+\omega_-}{\omega_+ - \omega_-} = \frac{\omega_z^2}{2}\frac{1}{\omega_c(1 - \frac{2\omega_-}{\omega_c})} \sim \frac{\omega_z^2}{2\omega_c} \sim \frac{V_o}{2d^2B} \qquad (4.12)$$

which means $\Delta\omega_c$ is essentially mass independent. The systematic shift in the cyclotron frequency can therefore be minimized with the application of small trapping potentials which reduces the amplitudes of the eigenmotions, or by using a trap with large characteristic dimension. Another option is to reduce the octupole and dodecapole terms. This possibility is realized by the addition of extra electrodes to the Penning trap. The octupole term is reduced by positioning extra ring electrodes, denoted correction ring electrodes, between the central ring and endcap electrodes. Minimizing the dodecapole term requires extra electrodes placed outside the trap and are called correction tube electrodes. They are placed in close proximity to the apertures in the endcap electrodes. Even if all these suggestions are followed, deviations from a pure quadrupole potential are still inevitable.

Another source of systematic effects stems from misalignments between the axis of the electrostatic trapping field and the magnetic field axis. This tilt of one axis with respect to the other results in a shift of the cyclotron frequency:

$$\Delta\omega_c \approx \frac{9}{4}\omega_- \sin^2\Theta, \qquad (4.13)$$

assuming the tilt angle $\Theta <<1$. For the CPT apparatus, the alignment is estimated to be better than 0.2 milliradians [42]. Similar to the systematic effects arising from electric field imperfections, a misalignment of the electric field axis with the magnetic field axis produces frequency shifts which are essentially mass independent.

Shifts in the cyclotron frequencies, including those which result from electric field imperfections or from misalignments between the electric field and magnetic field axes, produce systematic errors even when a well-known mass is used to calibrate the magnetic field. From Eq. 4.10, with $q_{ref} = q$ for simplicity, the mass of the desired ion can be expressed as:

$$m = m_{ref}\frac{\omega_{c,ref}}{\omega_c} = m_{ref}\frac{(\Delta + \omega'_{c,ref})}{(\Delta + \omega'_c)} \tag{4.14}$$

for mass independent shifts Δ in the measured cyclotron frequencies $\omega'_{c,ref}$ and ω'_c. Since $\Delta << \omega'_c$ (and $\Delta << \omega'_{c,ref}$) then:

$$m \sim m_{ref}\frac{\omega'_{c,ref}}{\omega'_c}\left(1 + \frac{\Delta}{\omega'_{c,ref}}\right)\left(1 - \frac{\Delta}{\omega'_c}\right) \tag{4.15}$$

and after some algebra, the systematic shift Δm of the mass m from the measured mass m' can be determined:

$$m \sim m_{ref}\frac{\omega'_{c,ref}}{\omega'_c}\left[1 + \frac{\Delta}{qB}(m_{ref} - m)\right] = m' + \Delta m. \tag{4.16}$$

Thus, the relative error in the measured mass,

$$\frac{\Delta m}{m'} = \frac{\Delta}{qB}(m_{ref} - m) \propto m_{ref} - m. \tag{4.17}$$

The conclusion drawn is that if a highly accurate measurement is desired, the reference mass should be chosen to be as close in mass as possible to the unknown mass.

Since precise mass measurements are obtained from cyclotron frequency determinations which, in turn, depend upon the magnetic field, any magnetic field inhomogeneities or fluctuations could potentially be a concern. Sources of magnetic field imperfections include the finite extent of the coils used to generate the field and the magnetic susceptibility of the materials used to construct the Penning trap and surrounding structures. If the magnetic field is a function of odd powers of the distance from the trap center, then no shift in the motional frequencies is observed [30] because the changes in the ion motion average to zero. Instead, the leading contribution to affect the cyclotron frequency is a hexapole term such that the magnetic field strength:

$$B = B_o[1 + \beta_{quad}(\rho_z^2 - \rho^2/2)] \tag{4.18}$$

with B_o representing the value of the field at the center of the trap. Here, β_{quad} expresses the strength of the quadrupole contribution. With the field described by Eq. 4.18, the cyclotron frequency will shift [15] by an amount:

$$\Delta\omega_c \sim \beta_{quad}\omega_c(\rho_z^2 - \rho^2). \tag{4.19}$$

The effects of such frequency shifts can be determined by substituting frequency, or equivalently mass, dependent shifts for the mass independent shifts in Eq. 4.14:

$$m = m_{ref}\frac{\omega_{c,ref}}{\omega_c} = m_{ref}\frac{(\Delta_{ref} + \omega'_{c,ref})}{(\Delta + \omega'_c)} \tag{4.20}$$

where $\Delta_{ref} \neq \Delta$. Given $\Delta_{ref} = A\ \omega'_{c,ref}$ and $\Delta = Z\ \omega'_c$, then:

$$m = m_{ref}\frac{\omega'_{c,ref}}{\omega'_c}\frac{(1 + A)}{(1 + Z)}. \tag{4.21}$$

Again, with $A \ll 1$ and $Z \ll 1$:

$$m \sim m_{ref}\frac{\omega'_{c,ref}}{\omega'_c}(1 + A - Z) = m' + \Delta m, \tag{4.22}$$

so that the relative error in mass,

$$\frac{\Delta m}{m'} = A - Z. \tag{4.23}$$

Therefore, if $A \sim Z$, the mass dependent shifts are negligible and the masses determined from measurements of the cyclotron frequencies will still be accurate. In the case of shifts resulting from a magnetic field as described by Eq. 4.18, this last statement is true only if the cyclotron frequencies used in the ratio were obtained from ions driven with similar amplitudes. Notwithstanding, the magnetic field inhomogeneity should be kept as small as possible to justify the assumption $A \ll 1$ and $Z \ll 1$. The last time the magnet for the CPT was checked for inhomogeneities was in February of 2001, at which time it was deemed necessary to re-shim the magnet. The results from this procedure are shown in Table 4.1. In the volume occupied by the trapped ions, the field is now approximately linear in all dimensions with a slope relative to the mean field of -2.5 $\times$ 10^{-7} cm^{-1} along the field axis (defined as the z-axis), -6.3 $\times$ 10^{-6} cm^{-1} along an axis perpendicular to the field axis (defined as the x-axis) and 11.0 $\times$ 10^{-7} cm^{-1} along the y-axis.

The method of using cyclotron frequency ratios to determine the masses of the desired nuclides naturally assumes that the magnetic field has not changed during any particular measurement or between the measurements of the reference and unknown masses. Monitoring of the magnetic field is therefore required. This is accomplished by measuring the cyclotron frequency of the reference mass interspersed with measurements of the desired ions. The magnetic field of the CPT magnet is extremely stable, and has been recently measured as having a decay rate of approximately 1.1 parts in 10^{10} per hour [49], consistent with earlier observations [39]. Corrections for the decay in the field are therefore only really necessary for measurements which require high precision.

The number of ions present in the trap during each quadrupole field excitation also influences the resonant cyclotron frequency. If more than one ion is present in the trap during the excitation, the additional Coulomb interaction between the ions needs to be taken into account. According to Ref. [50], if the ions simultaneously stored in the trap are identical in mass and charge state, then the space charge effect created by the collection of identical ions has no effect on the q/m center of mass motion. The ion cloud motion behaves indistinguishably from the motion of a single ion in the trap. However, shifts in the magnetron and reduced cyclotron frequencies have been noted to occur. As reported by Ref. [51], the observed ω_- and ω_+ frequency shifts offset each other such that the cyclotron frequency ($\omega_c = \omega_- + \omega_+$) was unaffected. The conclusion draw by Ref. [51] was that the source of the frequency

Table 4.1: Measurements (in Tesla) of the 6 Tesla magnetic field both along and perpendicular to the field axis. The top row of the table, labelled as "x", shows the radial distance in centimeters from the center of the Penning trap. The first column, labelled as "y", represents the radial distance in centimeters from the trap center in a direction perpendicular to the "x" axis. Within each cell are seven measurements of the magnetic field along the magnetic field axis, the "z" axis. The spacing between each measurement along the "z" axis is one centimeter so that each cell shows the measurements between -3 cm and 3 cm from the trap center along the field axis. For positions in which no measurements were made, the space is left blank.

y\x	-2	0	2
-2		5.8892930 5.8892383 5.8891995 5.8891574	
0	5.8891247 5.8890503 5.8890313 5.8889988	5.8890994 5.8891315 5.8891305 5.8891343 5.8891360 5.8891312 5.8891247	5.8892074 5.8892235 5.8892906 5.8893050
2		5.8889708 5.8890003 5.8890520 5.8890756	

shift was electrostatic in origin as the cyclotron frequency, which is independent of the electrostatic trapping fields, was unaltered. Furthermore, they suggested the shifts were due to the induced surface charge on the trap electrodes. Although they did not witness a number-dependent shift of the cyclotron frequency, the CPT collaboration has [41, 52]. As suggested in Ref. [47], these shifts may be the result of space charge effects. If the space charge is significant enough to force a number of ions into regions of magnetic field inhomogeneities, then the cyclotron frequency will appear to shift since the ions are subjected to a different magnetic field. To decrease space charge effects, only a small number of ions should be simultaneously present in the trap during any excitation, or the magnetic field imperfections should be reduced as much as possible. In addition, either a larger trap or reduced motional amplitudes should be used to minimize induced surface charge effects. The magnitude of the relative cyclotron frequency shifts previously observed with the CPT [41, 52] was $\sim$ -2×10^{-9} per detected ion. The results from Ref. [52] are shown in Fig. 4.2. A recent, more careful test [49] of the ion number effect which uses pure ion samples of ^{22}Ne showed a relative shift of $\sim +2 \times 10^{-9}$ per detected ion as shown in Fig. 4.3. Different possibilities could explain the change in the magnitude of the effect. The first tests were performed with large numbers of ions with an analysis which used large bin sizes. Now all new measurements, including the latter test, are conducted with ion samples containing only a few ions with smaller bin sizes. The decrease in ion counts and bin size from the latter tests offer a more precise determination of the ion number dependency with data which more reflects current mass measurement policy. Since a decrease in the ion count provides a reduction in space charge, the latter tests quite possibly put the ions in different magnetic fields. In addition, the Penning trap was physically removed for maintenance purposes at times between each series of tests. Each time the Penning trap was returned to the magnet bore, its repositioning was quite likely slightly different from its original position. If a space charge effect is responsible for forcing the ion cloud to experience different

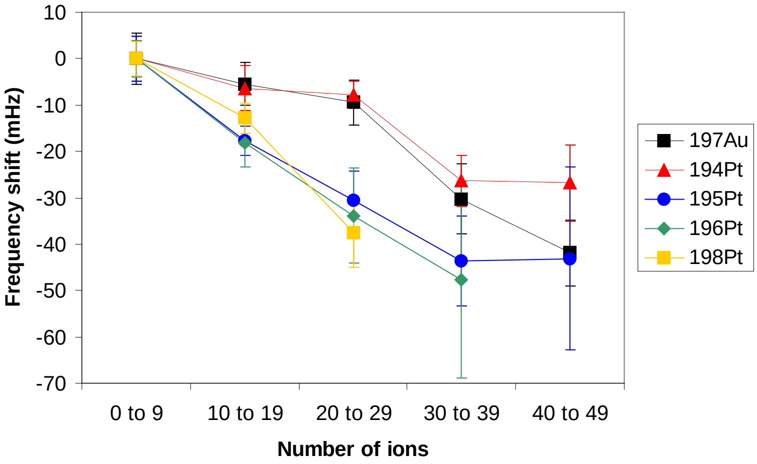

Figure 4.2: Shift of the cyclotron frequency due to the presence of many ions as reported by Ref. [52]. The data collected was first sorted into bins according to the number of ions detected per shot. Afterwards, fits using the modified Sinc function as described by Eq. 3.7 were performed on each resulting TOF spectra. The plotted shift in frequency for each isotope is with respect to the cyclotron frequency determined from the bin of 0 to 9 ions for that particular isotope. The lines shown are to guide the eye only.

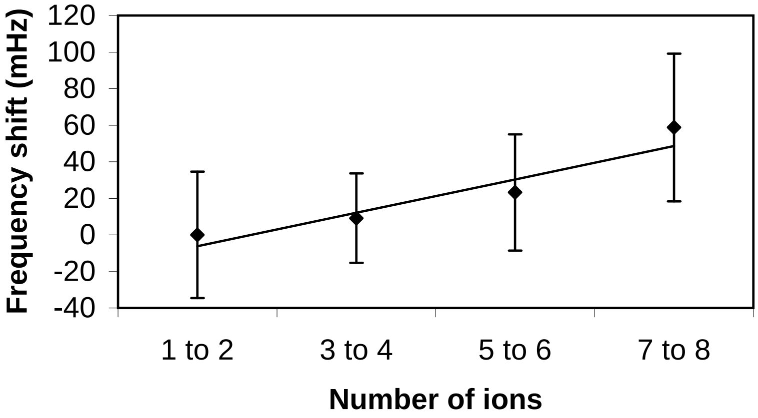

Figure 4.3: Shift of the cyclotron frequency due to the number of simultaneously trapped ^{22}Ne ions as reported by Ref. [49]. The data was first sorted into bins according to the number of ions detected per shot. Afterwards, the TOF spectra for each bin was fit with modified Sinc functions (Eq. 3.7). The plotted shifts in the cyclotron frequency are with respect to the frequency obtained from the bin with 1 to 2 ions detected per shot. The assumed linear dependence of the frequency shift due to the number of simultaneously trapped ions is represented by the line which was fit to the data.

magnetic field imperfections, then after a repositioning of the trap the trapped ions will undoubtedly be subjected to different field inhomogeneities.

The number of dissimilar ions present while the excitations are performed results in systematic effects which are much more pronounced than those arising from a pure sample of identical ions simultaneously stored in the trap. As reported in Ref. [53], the magnitude of the frequency shift depends upon both the number of desired ions and contaminant ions, in addition to the difference in masses of the two groups of ions as compared to the linewidth of the resonance. If the resolution is insufficient to resolve the desired ions from the contaminant ions, the observed cyclotron frequency resonance is narrower than expected and is at a frequency governed by the center of mass of the ions in the trap. However, if the two groups of ions can be resolved, then the cyclotron frequencies of both groups are shifted to lower frequencies with each cyclotron frequency shifted by an amount which depends upon the number of ions contributing to the other resonance. Tests of the magnitude of this effect with the CPT are not easy owing to the difficulty in having a controlled experiment where a constant number of ions of one species is maintained while the number of the other ion species is varied. One possibility is to adopt the technique discussed in Ref. [53] in which two ion species are captured in the Penning trap with the half-life of one of the species being on the order of a few tenths of a second. The number of contaminant ions can then be varied by delaying the excitation an amount of time sufficient for a reduction in the number of contaminant ions by decay. However, if the ion number is kept to a minimum, then the interactions between dissimilar ions which give rise to the systematic effects are reduced.

The timing of the pulse used to capture the ions into the Penning trap is also critical. Recall that the capture pulse is applied to the first, or bottom, two electrodes of the Penning trap: the bottom correction tube and the bottom endcap. If the desired ions reach the trap before the pulse is applied, the ions will not enter the trap and the capture efficiency is observed to decrease. On the other hand, if the capture pulse duration is too long, the ions have sufficient time to exit the trap from the same direction which they entered, also observed as a decrease in the capture efficiency. So far, these effects only affect the capture efficiency and, therefore, the precision of the measurement. However, two more cases of improper timing must be considered. First, if the capture pulse ends too early such that the potential of the bottom two electrodes return to their nominal potential while ions are still passing through the apertures in the electrodes, the energy of the ions is inadvertently changed. Similarly, if the pulse ends too late, the ions may also gain energy. In this case, the ions may have already traversed the length of the trap and are in the process of exiting the trap when the potential of the bottom electrodes are returned to their nominal potential. In either case, the energy of the incoming ions are altered, and if the evaporation pulse is not sufficient to remove these ions, the more highly energetic ions undergo a greater axial oscillation. If the magnetic field is not completely homogeneous within the trap volume, the higher axial oscillation probes a greater extent of the magnetic field inhomogeneities and therefore the cyclotron frequencies are affected. An example of the effect of the Penning capture pulse timing on the generated TOF spectra is shown in Fig. 4.4. All TOF spectra were generated under similar conditions, including the application of the evaporation pulse. Only the capture pulse timing was changed. The change in the cyclotron frequencies of the ^{22}Ne ions is evidence of the ions experiencing different magnetic field strengths. Simultaneously, the resulting gain in energy from the early closure of the trap is seen as a reduction in the baseline, and therefore, the time-of-flight depths of the TOF spectra. Even with consistent, but inefficient, timing of the capture pulse, the TOF baseline and cyclotron frequencies are still susceptible to jitter in the timing electronics. Furthermore, cyclotron frequency ratios between ions of different masses are subject to error since the simple scaling of the capture pulse timing by the square root of the mass is only accurate if no offsets in the timing exists. For these reasons, it is imperative that proper capture pulse timing be used, both for the increase in efficiency and the reduction in systematic effects. Thus, the

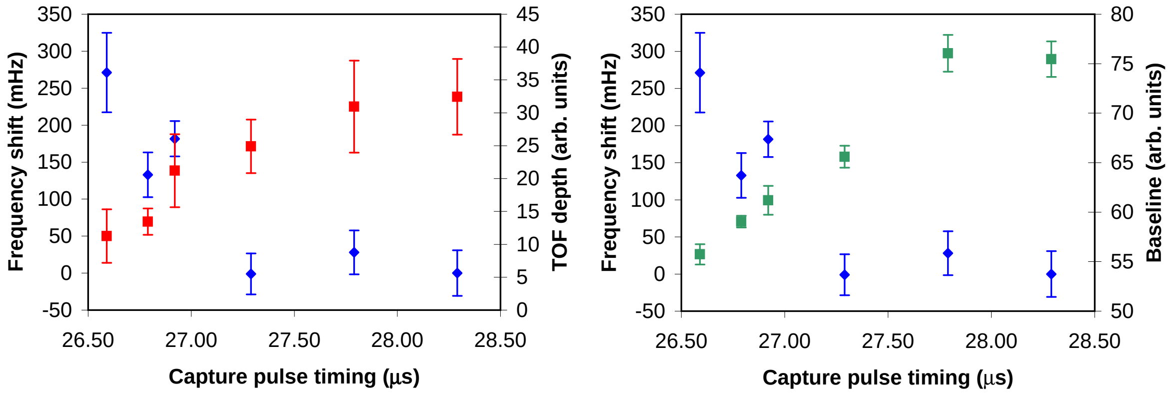

Figure 4.4: The effect of the Penning capture pulse timing on captured ^{22}Ne ions. On the left, a comparison can be made between the cyclotron frequency (blue) and TOF depth (red) resulting from fitting the modified Sinc function (Eq. 3.7) to the TOF spectra which were generated for various settings of the Penning capture pulse timing. On the right, a comparison can be made between the cyclotron frequency (blue) and baseline (green) obtained from fits of the modified Sinc function to the TOF spectra which were acquired for various settings of the Penning capture pulse timing. The capture times represent the end of the applied pulse.

procedures outlined in Sec. 3.4.2 should always be followed.

In making accurate mass measurements with the CPT, care must be taken to minimize all possible systematic effects. Some sources result in mass independent frequency shifts which can be reduced by using reference masses close to the desired masses. Other systematic effects which produce mass dependent frequency shifts can be decreased by ensuring consistent conditions between the reference and unknown mass. Overall, the following procedures are followed to produce accurate measurements with the CPT:

- reference masses are molecules composed of ^{1}H, ^{12}C, ^{14}N, and ^{16}O, or other well-known masses,
- the reference mass is close in mass to the mass of the desired ions,
- the Penning trap is carefully tuned to provide as harmonic a potential as possible,
- the amplitude of the initial magnetron motion is the same for all masses to

ensure the ions probe the same magnetic field,

- the decay of the magnetic field is measured by periodically measuring the cyclotron frequency of the reference mass,
- the number of simultaneously trapped ions are kept to a minimum,
- all contaminant ions are removed before the excitation of the desired ions, and
- the capture pulse timing is optimized before any measurements are performed.

When all these rules are followed, the CPT produces accurate mass measurements with a remaining systematic uncertainty of less than 1 part in 10^8 of the mass.

4.2 ^{68}Ge, ^{68}As, and ^{68}Se

Measurements of ^{68}Ge, ^{68}As, ^{68}Se, and the calibrant C_5H_8 were obtained from a total of three experimental runs. A description of the experiments and the determination of the nuclide masses is provided in this section.

The first experimental run, which occurred June 5 to June 8 of 2002, provided ω_c frequency ratios of ^{68}As$^+$ and ^{68}Ge$^+$ relative to $C_5H_8{}^+$ (hydrocarbons are produced in the gas catcher system [54]). The nuclides were produced using a 220 MeV ^{58}Ni^{15+} beam from ATLAS incident upon the target wheel consisting of 1 mg/cm^2 carbon foils. The production and transfer of A=68 ions were optimized by observing the amount of activity seen at the Si detectors as parameters of the various devices were adjusted. Since the Si detectors in their current configuration are only sensitive to β decay, of the possible β activity available at A=68, ^{68}As is the only nuclide produced in detectable quantities. After the instrument was tuned to maximize the amount of A=68 activity (^{68}As) at Si 3, 2200 counts per 2 minutes were detected with a beam current of 150 enA. However, with 600 enA of beam current, only 5000 counts per 2 minutes were detected, suggesting at least one of the devices prior to Si 3 was

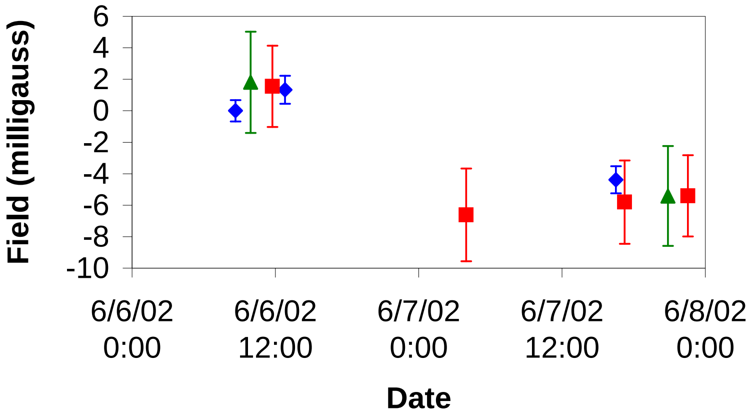

Figure 4.5: Stability of the magnetic field during the first ^{68}Se experiment. The datum points represent the field strength as determined by using ions of C_5H_8 (blue diamonds), ^{68}Ge (red squares) and ^{68}As (green triangles), normalized to the first datum point with $B = 58891094$ milligauss.

saturating at higher beam currents. Time constraints prevented the finding of the culprit during this experiment.

All cyclotron resonances obtained during this experiment were performed with quadrupole excitations of one second. The data consisted of three data sets of C_5H_8, four data sets of ^{68}Ge, and two data sets of ^{68}As. Attempts were made to obtain cyclotron resonances of ^{68}Se, but none were found by current methods. Because the linear trap acts as a buffer to the Penning trap, any change in the conditions before the linear trap has no affect on the mass measurements. All other parameters involved in the transfer and excitation of the ions following the linear trap are important. During this experiment, these conditions were essentially identical.

Contaminant ions were identified as C_4H_4O, C_5H_7, and C_5H_9. These ions, in addition to the undesired C_5H_8, ^{68}As, and ^{68}Ge ions, were first removed from the Penning trap before any magnetron or cyclotron field was applied.

The magnetic field was monitored periodically by measuring the cyclotron frequency of C_5H_8. (See Fig. 4.5.) All the plotted datum points represent the field strength $B = \frac{m\omega_c}{q}$ as calculated by using the masses determined from the combined results of all three experiments. Each datum point has a date which corresponds to

Table 4.2: Cyclotron frequencies of the specified ion in units of Hz. These frequencies (with the statistical uncertainties in parentheses) were obtained from the first ^{68}Se experiment before the high voltage discharge.

	$^{12}C_5{}^1H_8$	χ^2_R	^{68}Ge	χ^2_R	^{68}As	χ^2_R
individual fits	1328697.364(12) 1328697.394(20)	1.70 0.70	1331328.3875(73)	2.89	1331158.304(20)	1.76
summed spectra	1328697.376(10)	1.81				
weighted average	1328697.375(12)	1.41				
final value	1328697.376(14)		1331328.388(12)		1331158.304(27)	

the average of the times at the beginning and end of the data set. The error bars shown include only the uncertainties of the masses and the cyclotron frequencies. Other parameters used in the calculations were taken as constant (values are shown in Table 4.8) as their effect would be only a systematic shift of all values. An examination of Fig. 4.5 shows the field to be stable within two distinct groups, hereinafter referred to as EXP1A (field values before midnight on June 7, 2002) and EXP1B (field values after midnight on June 7, 2002). The high voltage power supply, which delivers voltages to all electrodes requiring voltages greater than 50 volts, had tripped at a time between EXP1A and EXP1B. The tripped supply probably resulted from a discharge which created many ions. These ions would travel through the Penning trap and could provide a charge on any insulating material present in the trap. The build up of charge would change the electric field of the trap and change the position of the potential minimum, placing the ions in a slightly different magnetic field which would result in different cyclotron frequencies. Regardless of the cause of the shift in the magnetic field, the analysis of the data was performed on the EXP1A and EXP1B sets independently.

For each data set, the TOF spectra obtained was fit using the modified Sinc function as given by Eq. 3.7. The resulting cyclotron frequency and the reduced chi-squared of each fit are shown in Table 4.2 and Table 4.3. In cases where more than one data set was acquired for a particular ion, a comparison was made between

Table 4.3: Cyclotron frequencies of the specified ion in units of Hz. These frequencies (with the statistical uncertainties in parentheses) were obtained from the first ^{68}Se experiment after the high voltage discharge.

	$^{12}\text{C}_5{}^1\text{H}_8$	χ^2_R	^{68}Ge	χ^2_R	^{68}As	χ^2_R
individual fits	1328697.265(19)	0.98	1331328.221(16)	1.22	1331158.140(22)	1.15
			1331328.2301(88)	1.76		
			1331328.203(30)	1.27		
summed spectra			1331328.2214(77)	2.12		
weighted average			1331328.2256(94)	0.33		
final value	1328697.265(19)		1331328.221(11)		1331158.140(24)	

Table 4.4: Average number of ions detected per shot during the first ^{68}Se experiment, both before and after the high voltage discharge. The analysis of the data only used the number of ions detected per shot as indicated.

	EXP1A			EXP1B		
	$^{12}\text{C}_5{}^1\text{H}_8$	^{68}Ge	^{68}As	$^{12}\text{C}_5{}^1\text{H}_8$	^{68}Ge	^{68}As
	8.6	9.8	5.2	34	13	8.5
	26				14	
					13	
N used	<20	<20	<20	<30	<30	<30

two different methods used to combine the data. One manner was to determine the weighted average of the individual fits, and the other procedure was to combine the different data sets together to produce a summed spectra before performing one fit on the combined data. An example of a TOF spectrum generated with summed data is shown in Fig. 4.7 which consists of the ^{68}Ge data sets accumulated during EXP1B. Good agreement between the two different methods of combining data sets was generally found and the final result used in the mass determinations was obtained from the summed data, with the statistical uncertainty inflated by the square root of the reduced chi-squared for those cases where $\chi^2_R > 1$.

During this first ^{68}Se experiment, careful consideration was not given to the number of trapped ions. The average number of ions detected per shot varied enormously as shown in Table 4.4. We tried to minimize the differences in the number of trapped ions between ion species, however, even with careful analysis of the data, a systematic effect will remain as discussed in Sec. 4.1.2. The overall magnitude of this effect is discussed later when the masses are determined from the weighted average of all cyclotron frequency ratios.

During the second experiment (August 21 - August 24, 2002), cyclotron frequency ratios of ^{68}As$^+$ and ^{68}Se$^+$ relative to ^{68}Ge$^+$ were determined. The parameters for the various devices were similar to those of the previous experiment with one major exception – the isotope separator was in use for this experiment, unlike the last one. Once the parameters for the isotope separator were optimized, the voltages for the two following ion traps were reduced by 6 volts to account for the difference in the energy of the ions ejected from the isotope separator as compared to the ion cooler from the previous experiment. Estimates of the effect of the isotope separator suggested that molecules at A=67 and A=69 were suppressed by a factor of 200 and contaminant molecules at A=68 were suppressed by a factor of 10. The total A=68 activity detected at Si 3 was $\sim$ 3200 counts per two minutes with a beam current of 450 enA, which is approximately 80% of the amount found during the first experiment.

The excitation modes of the ions trapped in the Penning trap were performed with similar conditions. Quadrupole field excitations of 200 ms were used to generate TOF spectra. Contaminant ions were identical to the previous experiment and were removed before any excitation on the ions of interest was performed. The complete set of data consisted of three data sets of ^{68}Ge, one data set of ^{68}As, and two data sets of ^{68}Se.

The magnetic field was found to be relatively stable during this experiment as seen in Fig. 4.6, and as such, the complete set of data was analyzed together. The TOF spectra for each data set was fit using the modified Sinc function (Eq. 3.7) and the resulting fits are shown in Table 4.5. A comparison between the summed ^{68}Ge data and the weighted data are consistent and, as before, the final result used in the mass determinations was obtained from the summed data, with the statistical uncertainty

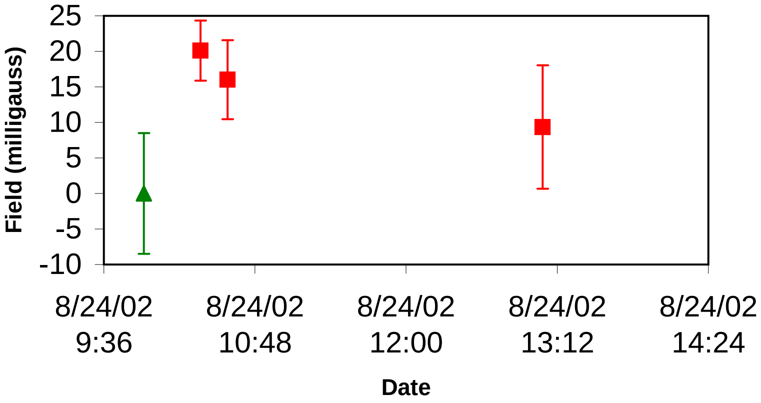

Figure 4.6: Stability of the magnetic field during the second ^{68}Se experiment. The explanation for the data shown is equivalent to that which explains Fig. 4.5. In this case, the data are normalized to the first datum point with $B = 58891061$ milligauss.

Table 4.5: Cyclotron frequencies (with statistical uncertainties in parentheses) of the particular ion species determined from the second ^{68}Se experiment (in units of Hz). The values of the reduced chi-squared from the fits to the TOF spectra are also shown. In the case of ^{68}Se, individual fits to each data set were not possible; one fit was conducted on the summed data.

	^{68}Ge	χ^2_R	^{68}As	χ^2_R	^{68}Se	χ^2_R
individual fits	1331328.052(75)	1.05	1331157.51(18)	0.81		
	1331327.96(11)	1.15				
	1331327.81(14)	1.89				
summed spectra	1331327.974(56)	1.62			1331060.13(52)	1.03
weighted average	1331328.001(60)	0.81				
final value	1331327.974(71)		1331157.51(18)		1331060.13(53)	

inflated by the square root of the reduced chi-squared.

The number of detected ions per measurement cycle was comparable between different ion species. Approximately 5 ions per shot of ^{68}Ge, 3 ions per shot of ^{68}As and less than 1 ion per shot of ^{68}Se were detected. The data analysis considered those cases with less than 15 ions per shot, effectively using all the data.

Cyclotron frequencies of all four ions of interest, C_5H_8, ^{68}Ge, ^{68}As, and ^{68}Se, were determined from the last ^{68}Se experiment which occurred September 16 to September 21 of 2002. The only significant difference from the last run was a more intense ^{58}Ni^{15+} beam. With 1600 enA of primary beam, 5000 counts per two minutes were detected at Si 3, while 1500 counts per two minutes of A=68 activity was detected for 280 enA of beam. Assuming the production cross section of ^{68}Ge and ^{68}As is roughly 100 mbarns as given by PACE4 [55], the efficiency between production and detection on the final MCP detector is on the order of 0.0001%. This not only includes unintentional losses in transmission, but processes such as the evaporation pulse in which ions are purposely removed to obtain more precise measurements. If we consider the amount of activity normalized to the primary beam current, this experiment yielded roughly 60% of the amount detected from the previous experiment, and 50% of the amount from the first ^{68}Se experiment.

In total, one data set of C_5H_8, three data sets of ^{68}Ge, eight data sets of ^{68}As, and four data sets of ^{68}Se were accumulated, all with 200 ms quadrupole excitations. An example of the TOF spectrum generated for ^{68}Se is shown in Fig. 4.7.

The magnitude of the magnetic field at various times during the experiment, as experienced by C_5H_8, ^{68}Ge, and ^{68}As ions, is shown in Fig. 4.8. With a few exceptions, the field strength is constant over the one day in which most of the data was collected. The cause of the deviation of the field as measured using the first ^{68}Ge data set could not be explained. However, the fourth and fifth data sets of ^{68}As were generated to observe the effect of changing the amplitude used to clean undesired ions. Apparently, the cyclotron frequency is influenced by this change, most probably resulting from

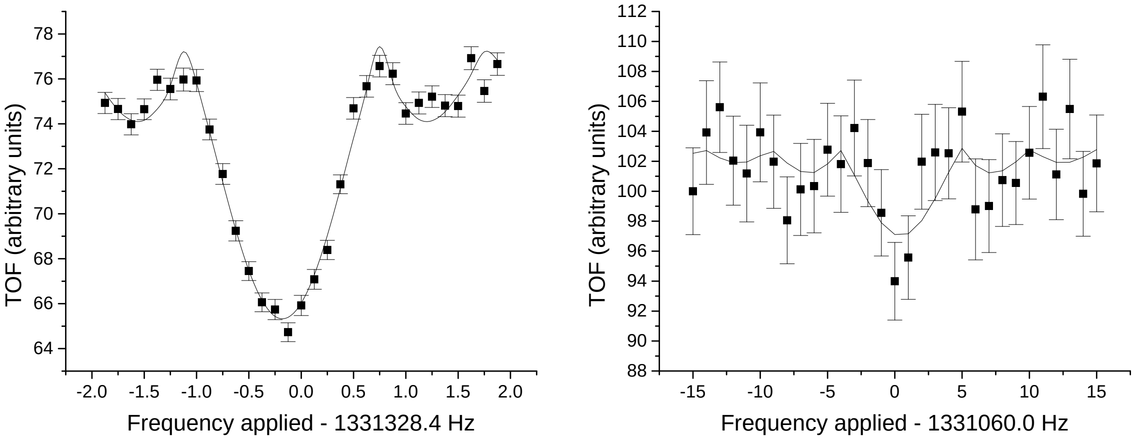

Figure 4.7: A TOF spectrum obtained for ^{68}Ge^{+} (left) and ^{68}Se^{+} (right). A quadrupole excitation of 1000 ms (left) or 200 ms (right) in duration was applied after first removing contaminant ions and establishing an orbital radius with a magnetron excitation. The ^{68}Ge^{+} spectrum has a FWHM of $\sim$ 0.9 Hz (40 keV) and the spectrum shown for ^{68}Se^{+} has a FWHM of $\sim$ 4.5 Hz (200 keV), consistent with the Fourier-limit. The curves shown represent the fits using the modified Sinc function (Eq. 3.7).

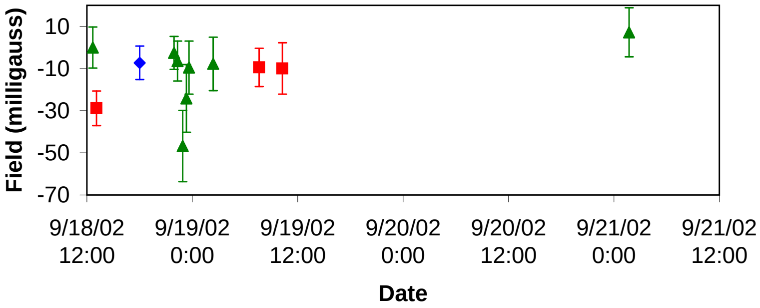

Figure 4.8: Stability of the magnetic field during the third ^{68}Se experiment. The explanation for the data shown is equivalent to that for Fig. 4.5. In this case, the data are normalized to the first datum point with $B = 58891202$ milligauss.

Table 4.6: Cyclotron frequencies (statistical uncertainties in parentheses) of the particular ion species determined from the third and final ^{68}Se experiment (in units of Hz). The values of the reduced chi-squared from the fits to the TOF spectra are also shown. See the text for further explanation.

	$^{12}C_5{}^1H_8$	χ^2_R	^{68}Ge	χ^2_R	^{68}As	χ^2_R	^{68}Se	χ^2_R
individual fits					1331160.81(21)	1.10		
	1328699.65(12)	2.40	1331330.15(18)	0.85	1331160.60(20)	1.30		
			1331330.59(16)	1.46	1331160.52(39)	2.17		
			1331330.58(25)	1.13	1331160.22(52)	1.74		
					1331160.72(29)	1.30		
					fit not possible			
summed spectra			1331330.48(12)	0.74	1331160.60(15)	1.67	1331062.09(59)	0.84
weighted average			1331330.39(12)	1.68	1331160.60(17)	0.12		
final value	1328699.65(18)		1331330.48(12)		1331160.69(15)	0.51	1331062.09(59)	

an insufficient resolution required to remove the 'nearby' ^{68}Ge without disturbing ^{68}As itself. Aside from these tests, all the other data was performed with similar conditions, including the parameters for the removal of undesired ions. In the final analysis, the two ^{68}As test data sets were not considered.

The results from fitting modified Sinc functions (Eq. 3.7) to each individual data set are shown in Table 4.6. In this case of ^{68}Se, only the summed spectra was fit using the modified Sinc function since individual fits on each ^{68}Se data set were not possible. To limit systematic effects, the analysis of ^{68}Ge, ^{68}As, and ^{68}Se was performed only from data where less than 5 ions were detected per shot. For the last data set of ^{68}As, however, an average of 19 ions per shot was observed. Limiting the analysis of this data set to data where less than 5 ions per shot weighted the ^{68}As cyclotron frequency more heavily on the earlier data sets with no consequence on the results. This data set was obtained at a much later time compared to the earlier data sets, and the strength of the magnetic field would be more uncertain anyways. Furthermore, the analysis of C_5H_8 required data with less than 10 ions per shot since there were insufficient statistics if only 5 ions or less per shot were used. The final values shown in Table 4.6 are derived from the single data set, or the summed spectra in cases where more than one data set was obtained, with the error inflated by $\sqrt{\chi^2_R}$ for those cases when $\chi^2_R > 1$. For ^{68}As, the first file listed in Table 4.6 could not be summed together with the other data sets since its span of excitation frequencies was different. In this case,

Table 4.7: Results from all three ^{68}Se experiments in terms of the cyclotron frequency ratios (with statistical uncertainties in parentheses) between the indicated calibrant ion and the measured ion.

Experiment	Measured ion	Calibrant	Ratio (R)
1	^{68}As	$^{12}C_5{}^1H_8$	0.998151288(23)
1	^{68}Ge	$^{12}C_5{}^1H_8$	0.998023769(14)
1	^{68}Ge	$^{12}C_5{}^1H_8$	0.998023811(17)
1	^{68}As	$^{12}C_5{}^1H_8$	0.998151328(23)
2	^{68}As	^{68}Ge	1.00012806(15)
2	^{68}Se	^{68}Ge	1.00020123(40)
3	^{68}As	$^{12}C_5{}^1H_8$	0.99815120(17)
3	^{68}Ge	$^{12}C_5{}^1H_8$	0.99802391(16)
3	^{68}Se	$^{12}C_5{}^1H_8$	0.99822514(46)

the final value is a weighted average of the single data set and summed spectrum, with the uncertainty in each fit inflated by $\sqrt{\chi^2_R}$ before the weighted average was calculated.

Our measured cyclotron frequency ratios between the calibrant ion and measured ion, or equivalently the mass ratio between the measured ion and calibrant ion, are given in Table 4.7 from all three experiments. For the first experiment, two ratios are shown for each measured nuclide. The first two ratios were determined with data before the high voltage discharge discussed earlier; the last two ratios were determined with data after the high voltage discharge. Since the final masses of ^{68}Ge, ^{68}As, and ^{68}Se were determined with C_5H_8 as the reference mass, mass ratios between these nuclides and C_5H_8 were required. However, since the second experiment used ^{68}Ge as a reference, the ^{68}As/^{68}Ge and ^{68}Se/^{68}Ge ratios determined from this experiment had to be first multiplied by the weighted ^{68}Ge/C_5H_8 ratio before a weighted average of the ^{68}As/C_5H_8 and ^{68}Se/C_5H_8 ratios were conducted. The results of the weighted averaging is shown in Table 4.9.

For each ratio R, the mass of the neutral isotope, m, is determined using the relationship:

$$m = R(m_c - m_e) + m_e \tag{4.24}$$

Table 4.8: Constants used in calculations throughout this thesis. Only the uncertainties used in calculations are shown in parentheses. All other uncertainties are neglected.

Constant used	Value
1 u^{a}	931.494009 MeV c^{-2}
1 u^{a}	1660538.73×10^{-33} kg
Charge of electron^{b}	1.60217653×10^{-19} C
Electron mass^{a}	548.579911 μu
Mass of $^{12}C_5{}^1H_8{}^{a,c}$	68062600.25656(80) μu
Mass of $^{64}Zn^{a,c}$	63929142.22(73) μu

a) Obtained or derived from Ref. [48].

b) Obtained from Ref. [56].

c) Neglecting effect of enthalpy of formation and electron binding energies.

where m_e is the mass of the electron and m_c is the mass of the neutral calibrant. In this manner the final masses are calculated using the values in Table 4.7 in conjunction with the mass of C_5H_8 and the mass of the electron whose values are shown in Table 4.8.

Up to this point, the careful analysis of the ^{68}Se experiments has reduced systematic effects stemming from field instability and the number of ions which simultaneously underwent quadrupole field excitations in the Penning trap. No significant shift in magnetic field was detected during each experiment within the precision of our measurements, with one exception. In one case, the magnetic field appeared to shift as a result of a high voltage discharge. This situation required the data obtained before the discharge to be treated independently from the data obtained after the discharge. Ion bunches containing only a few detected ions were used to minimize the effects caused by ion-ion interactions, whether it be interactions between ions of the same nominal mass or of remaining contaminant ions. The frequency ratios were determined with roughly the same small number of ions detected for each ion species, with the largest difference being $\sim$ 20 detected ions per ion bunch. As discussed in Sec. 4.1.2, the cyclotron frequencies are dependent upon the number of ions trapped simultaneously. Therefore, the calculated cyclotron ratios between ion species will

Table 4.9: Final cyclotron frequency ratios between $C_5H_8^+$ and the singly-ionized nuclide with statistical uncertainty only, masses of the neutral isotopes with combined statistical and systematic uncertainty, the resulting mass excesses, and comparisons with the 1995 AME[5] and FRDM[57].

			Mass excess (keV)		
Nuclide	ω_c ratio	Mass (μu)	This work	1995 AME[5]	FRDM[57]
^{68}Ge	0.998023787(15)	67928095.1(29)	-66979.0(27)	-66977.0(64)	-66480
^{68}As	0.998151310(31)	67936774.6(35)	-58894.1(32)	-58880(100)	-58460
^{68}Se	0.99822484(30)	67941779(21)	-54232(19)	-54150(300)	-53550

result in a systematic shift if the number of ions used in the analysis for each species was different. This effect is conservatively estimated to result in a possible systematic error of $\triangle m/m \sim 4\times10^{-8}$.

All other systematic effects as discussed in Sec. 4.1.2 were minimized by good choice of calibrant ions and careful attention to parameters used to acquire the data. The conditions during each experiment which may affect the cyclotron frequency measurements, including the timing of the Penning trap capture pulse, were identical between ions of different species. Therefore, systematic effects which shift the cyclotron frequency for one ion species and proportionally shifts the cyclotron frequencies of all other ion species cancel each other so that the cyclotron frequency ratios remain the same. Other effects, for which the shifts in the cyclotron frequencies do not cancel, can possibility result in a small systematic bias proportional to the difference in mass between the reference mass and the measured species. Since the largest mass difference used in our experiments was only $\sim$ 0.135 u, these effects are negligible.

The only significant systematic effect for all ^{68}Se experiments results from different numbers of trapped ions between ion species and is of magnitude $\triangle m/m \sim 4\times10^{-8}$. The final masses shown in Table 4.9 have an error which is a combination of the statistical uncertainty and this systematic error added in quadrature. Since the latest atomic mass evaluation [48] already incorporates preliminary results from this work,

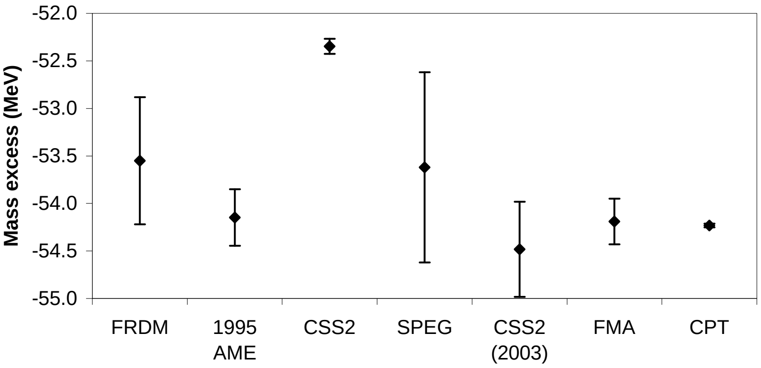

Figure 4.9: Comparison between different estimates and measurements of the mass excess of ^{68}Se. See the text for references and comments.

the masses reported here are compared to the values from the 1995 atomic mass evaluation [5] and the predictions of the finite-range droplet model (FRDM) [57]. The experimental data show that these nuclei are all more bound (by 538 keV on average) than predicted by the FRDM, but follow the expected trend based on systematics.

Due to the potential impact of the ^{68}Se mass on the outcome of x-ray burst model calculations, many different collaborations have attempted to make a measurement of the mass of ^{68}Se. A comparison of different estimates and measurements of the ^{68}Se mass from the past ten years is shown in Fig. 4.9. In 1995, estimates of the mass of ^{68}Se were provided by the Finite-Range Droplet Model (FRDM) [57] and the Atomic Mass Evaluation (1995 AME) [5]. In recent years, measurements have been made by the CSS2 cyclotron at GANIL [58], the SPEG facility also at GANIL [59], and the FMA apparatus [60] at ANL. Our measurement, labelled as CPT in Fig. 4.9, agrees well with all values except for the one determined by CSS2. Another nuclide, ^{76}Sr, was measured by CSS2 during the same experiment as for ^{68}Se and their mass determination for ^{76}Sr also disagrees with a precise measurement obtained from another Penning trap apparatus [61]. Since problems were encountered with the CSS2 experiment and two independent measurements disagree with the CSS2 results, significant doubts were raised about the reliability of those results. Due to these reasons, the results from the CSS2 experiment were not incorporated into the latest mass evaluation. A recent reattempt of the mass determination of ^{68}Se was conducted by CSS2 [62], labelled as CSS2 (2003) in Fig. 4.9. This recent result is now in agreement with our much more precise result.

An earlier measurement of the mass excess of ^{68}As [$\Delta M(^{68}\mathrm{As})$ = -58890(100) keV], which was obtained with the isochronous mode of operation of the experimental storage ring at GSI [63], agrees with our value. In addition, the Q_{EC} value (see Eq. A.8) for ^{68}Se determined from our measurements is 4662(20) keV and is in excellent agreement with the recent FMA measurement [$Q_{EC}(^{68}Se) = 4710(200)$]. Furthermore, the Q_{EC} value for ^{68}As calculated from this work [8084.9(42) keV] agrees quite well with that of Ref. [64] [Q_{EC} = 8100(100) keV]. Overall, the CPT results are in good agreement with all measurements completed by other experiments, but achieve much better precision.

4.3 ^{64}Zn, ^{64}Ga, and ^{64}Ge

The mass of the waiting-point nuclide ^{64}Ge was determined from two experiments held October 29 to November 2 of 2002 and January 27 to February 1 of 2003. This section will describe the experiments and analysis used to determine the mass ratios of ^{64}Ga and ^{64}Ge relative to ^{64}Zn.

During the first ^{64}Ge experiment, the isotopes ^{64}Zn, ^{64}Ga, and ^{64}Ge were produced using a 185 MeV ^{54}Fe^{16+} beam from ATLAS in conjunction with the rotating target wheel of 1 mg/cm^2 carbon foils. All instrumental parameters were scaled from the ^{68}Se experiments and were found to be close to the optimum values for the production and transfer of A=64 activity. Since ^{64}Ga was the only radioactive A=64 nuclide which was produced in abundant quantities, A=64 ions detected at the Si detectors were primarily from ^{64}Ga. Once the system was completely tuned, the activity attributable to ^{64}Ga detected at Si 3 during the first ^{64}Ge experiment was approximately 1500 counts per two minutes with 350 enA of primary beam current.

One data set for ^{64}Zn, four data sets for ^{64}Ga, and three data sets for ^{64}Ge were obtained with 200 ms quadrupole excitations. All data was acquired with consistent parameters except for the ^{64}Zn and first ^{64}Ga data set, in which contaminant molecules were not removed before applying the quadrupole excitations. Once the contaminants C_5H_4, CH_4O_3, CH_3O_3, and C_5H_5 were identified, these ions were removed from the trap before the remainder of the data sets were generated. An additional data set for each of ^{64}Ga and ^{64}Ge (not included in the aforementioned data sets) were obtained, but these data sets generated little data due to a dramatic decrease in transmission efficiency following an equipment malfunction. These two data sets were not considered in the following analysis.

The strength of the magnetic field, $B = \frac{m\omega_c}{q}$, was monitored periodically and is plotted in Fig. 4.10. All the values were calculated using the masses determined from the combined results of both ^{64}Ge experiments, and the error bars shown include only the uncertainties of the masses and the cyclotron frequencies. Other parameters used in the calculations (from Table 4.8) were taken as constant as their effect would systematically shift all values. Each datum point has a date which corresponds to the average of the times at the beginning and end of the data set. The collection of ^{64}Ge data and the extended loss of activity is responsible for the distinct gap in the graph. A weighted average of the field strengths plotted in Fig. 4.10 results in a reduced chi-squared of 0.4, suggesting the magnetic field was stable throughout the two-day acquisition of data.

The TOF spectra generated from each data set of ^{64}Zn and ^{64}Ga were fit using the modified Sinc function (Eq. 3.7). The resulting cyclotron frequency and the reduced chi-squared of each fit are shown in Table 4.10. All TOF spectra were generated with the condition that less than 10 ions were detected per shot, a condition which is more liberal than the 3 ions per shot detected on average for ^{64}Ga. Given that the production cross section for ^{64}Ga was on the order of 100 mbarns, the total efficiency of the system from production to final detection, including all intentional and unintentional losses, was approximately 6×10^{-4} %.

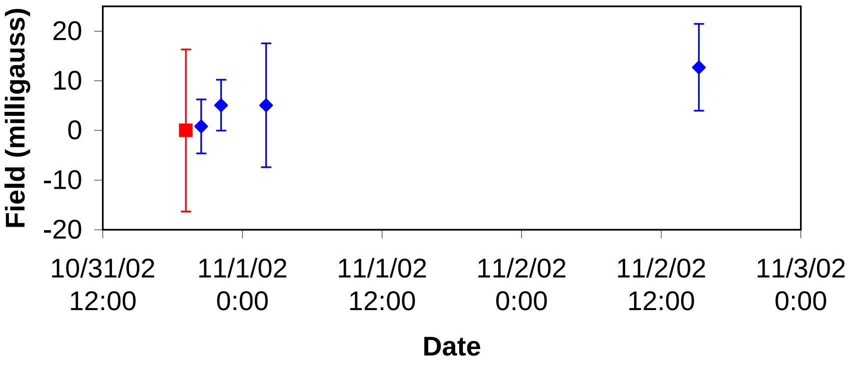

Figure 4.10: Stability of the magnetic field during the first ^{64}Ge experiment. The field strength as determined by using ions of ^{64}Ga (blue diamonds) and ^{64}Zn (red squares) is shown normalized to the first datum point with $B = 58891193$ milligauss.

Table 4.10: Cyclotron frequencies (statistical uncertainties in parentheses) obtained from the first ^{64}Ge experiment (in units of Hz). The values of the reduced chi-squared from the fits to the TOF spectra are also given.

	^{64}Zn	χ^2_R	^{64}Ga	χ^2_R
individual fits	1414609.88(39)	0.98	1414439.573(93)	1.28
			1414439.675(95)	0.84
			1414439.68(27)	1.17
			1414439.86(15)	1.81
summed spectra			1414439.639(60)	0.70
weighted average			1414439.656(65)	0.58
final value	1414609.88(39)		1414439.639(60)	

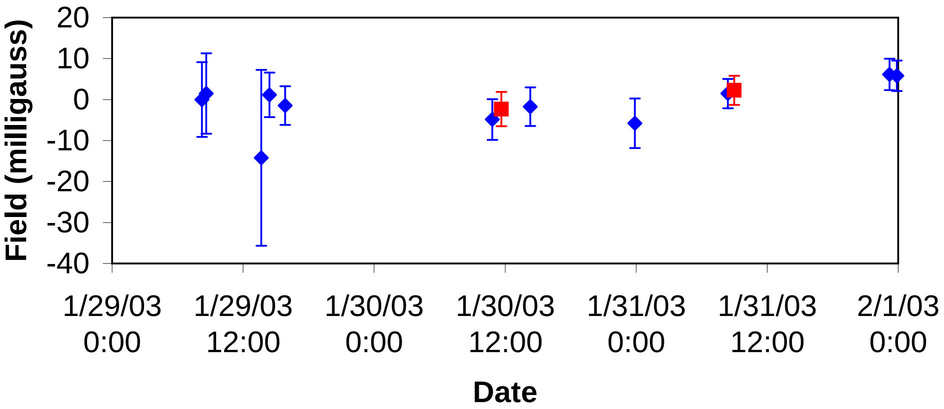

Figure 4.11: Magnetic field values determined during the second ^{64}Ge experiment from cyclotron resonances obtained of ^{64}Ga (blue diamonds) and ^{64}Zn (red squares). The data are normalized to the first datum point with $B = 58891202$ milligauss.

An attempt was made to fit the summed ^{64}Ge data by fixing the fitting parameters established by the summed ^{64}Ga data, with the exception of the baseline, central frequency, and TOF depth. However, all fits were consistent with a straight line, even with TOF spectra generated by limiting the number of ions detected per shot. Therefore, a value for the ^{64}Ge mass could not be determined from this experiment.

A second experiment was conducted to ascertain the ^{64}Ge mass. In total, eleven data sets of ^{64}Ga, two data sets of ^{64}Zn, and eight data sets of ^{64}Ge were collected. Most of the parameters for the various devices were similar to the last experiment, except for the magnetic triplet and Enge settings which were adjusted to focus a higher charge state of the ^{64}Ge recoils. Once optimum settings were found for the apparatus, up to 2500 counts per two minutes were detected at Si 3, yielding about four times more ^{64}Ga activity than was seen throughout the previous experiment.

The isotope ^{64}Ga, measured frequently during this experiment, was used to monitor the magnetic field strength. A weighted average of the field strengths plotted in Fig. 4.11 results in a reduced chi-squared of 0.7, which suggests the magnetic field was stable throughout the experiment. However, a high voltage discharge, similar to the one during the first ^{68}Se experiment, occurred. Since the electrostatic potential

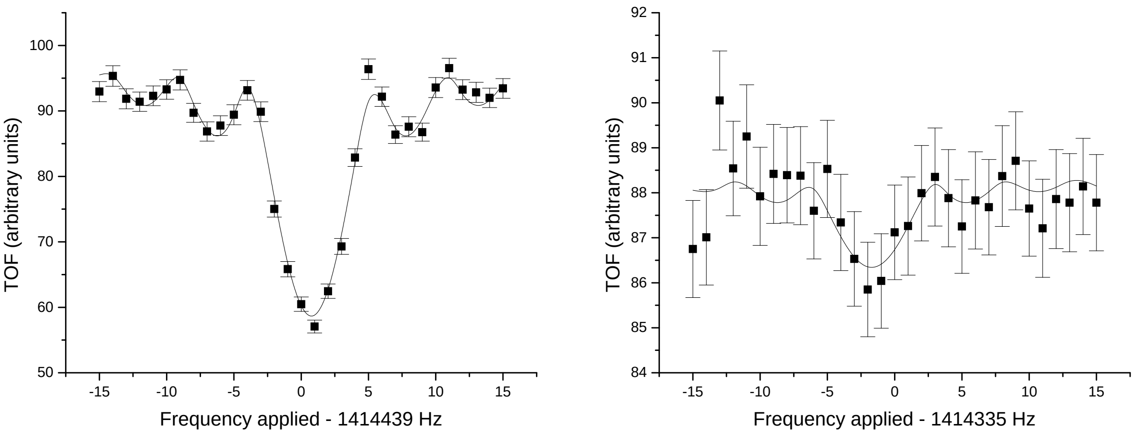

Figure 4.12: A TOF spectrum obtained for ^{64}Ga^{+} (left) and ^{64}Ge^{+} (right). Quadrupole excitations of 200 ms in duration were applied after first removing contaminant ions and establishing an orbital radius with a magnetron excitation. Both spectra have a FWHM of $\sim$ 4.5 Hz (190 keV) which is consistent with the Fourier limit. The curves shown represent the fits using the modified Sinc function (Eq. 3.7).

used to trap ions in the Penning trap is known to be affected by such high voltage discharges, the analysis of the last four data sets acquired after the discharge (including the last two ^{64}Ga data sets shown in Fig. 4.11) was conducted independently from the rest of the data sets.

All of the cyclotron resonances were obtained with ions exposed to the quadrupole field excitation for 200 ms except for the last three data sets of ^{64}Ga and the last data set of ^{64}Zn which were acquired with a 400 ms duration. Sample TOF spectra for ^{64}Ga and ^{64}Ge are shown in Fig. 4.12. Up to six ions were detected per second on the last MCP detector, delivering a total efficiency of $\sim$ 0.002% which confirms the four-fold increase in yield from the previous experiment as seen on Si 3.

The results of fitting modified Sinc functions (Eq. 3.7) to the TOF spectra obtained prior to the high voltage discharge are provided in Table 4.11. The first individual fits listed in Table 4.11 for ^{64}Ga and ^{64}Zn represent the cyclotron frequencies determined from ions subjected to a quadrupole field for 400 ms. All other data sets were generated from 200 ms exposures to the field. The final value combines the results from the two different excitation durations by calculating a weighted av-

Table 4.11: Cyclotron frequencies (with statistical uncertainties in parentheses) of the specified ion species determined from the second ^{64}Ge experiment (in units of Hz) before the high voltage discharge. The values of the reduced chi-squared from fitting the modified Sinc functions (Eq. 3.7) to the TOF spectra are also shown. Refer to the text for more details.

	^{64}Zn	χ^2_R	^{64}Ga	χ^2_R	^{64}Ge	χ^2_R
individual fits	1414610.179(73)	1.33	1414439.829(37)	0.57		
	1414610.07(10)	0.94	1414439.79(18)	1.26		
			1414439.83(22)	0.74		
			1414439.45(28)	3.37		
			1414439.82(10)	0.86		
			1414439.759(81)	1.04		
			1414439.677(90)	0.78		
			1414439.752(77)	1.14		
			1414439.66(12)	0.96		
summed spectra			1414439.763(40)	1.08	1414333.20(71)	0.61
weighted average			1414439.741(40)	0.31		
final value	1414610.134(64)	0.72	1414439.800(33)	1.39	1414333.20(71)	

erage using the fits resulting from the summed spectra for each field duration, with all uncertainties used in the weighted averages first inflated by $\sqrt{\chi^2}$. In situations where only one data set was obtained for a particular field duration, the individual fit was used in place of the fit to the summed spectra. On average, spectra of ^{64}Ga were obtained with 2 detected ions per shot, ^{64}Zn data were also collected with 2 ions per shot, and ^{64}Ge spectra consisted of 0.7 ions detected per shot. Occasionally, more than ten ions were detected per shot, but these cases were not considered in the analysis.

Only data sets of ^{64}Ga and ^{64}Ge were obtained after the high voltage discharge, but fits to the summed ^{64}Ge data were consistent with a straight line. Even if the fitting parameters for the ^{64}Ge spectra were fixed to the parameters established by the ^{64}Ga data, no evidence of a cyclotron resonance was detected. Therefore, the two ^{64}Ge data sets collected after the high voltage discharge were not used. Since the only remaining data sets which produced successful TOF spectra after the discharge were from ^{64}Ga, no mass determination could be made.

The cyclotron frequency ratios determined from the ^{64}Ge experiments relative to

Table 4.12: Cyclotron frequency ratios between the calibrant ion and the measured ion. The results from both ^{64}Ge experiments are shown. Statistical uncertainties in the ratios are shown in parentheses.

Experiment	Measured ion	Calibrant	Ratio (R)
1	^{64}Ga	^{64}Zn	1.00012036(28)
2	^{64}Ga	^{64}Zn	1.000120425(51)
2	^{64}Ge	^{64}Zn	1.00019580(51)

the reference nuclide ^{64}Zn are shown in Table 4.12. As before with the ^{68}Se experiment, the mass of ^{64}Ga and ^{64}Ge could be calculated using the relation given by Eq. 4.24 with the values given in Table 4.12 and the constants listed in Table 4.8.

Sources of systematic effects as discussed in Sec. 4.1.2 were minimized as much as possible. Magnetic field variations were monitored by measuring the cyclotron frequencies of ^{64}Zn and ^{64}Ga; no shifts in the measured frequencies were observed. Furthermore, only a few ions were simultaneously subjected to quadrupole field excitations. The largest difference in the number of ions detected per shot between ion species was ~ 4, which results in a systematic uncertainty of $\triangle m/m \sim 8{\times}10^{-9}$. One systematic effect which could contribute significantly to the overall systematic uncertainty is from the presence of contaminant ions. Although the magnitude of this effect has not been determined precisely with the CPT, an estimate is derived from Ref. [49]. In that paper, after corrections were made for all other systematic effects, the remaining differences in the mass determinations between the CPT and the 2003 AME for precisely known nuclides was $\triangle m \sim 1{\times}10^{-8} \cdot m$. This remaining systematic uncertainty could possibly be due to the presence of contaminant ions, and since the conditions for that experiment and the ^{64}Ge experiment are similar in terms of the number of simultaneously trapped ions, the uncertainty $\triangle m/m \sim 1{\times}10^{-8}$ is used as an estimate for the effect from contaminant ions. All other systematic effects are negligible since mass independent shifts were minimized by using ^{64}Zn as a reference mass which has a mass difference from ^{64}Ge of only 0.012 u, and mass

Table 4.13: Final weighted average of the cyclotron frequency ratios between ^{64}Zn and the specified singly-ionized nuclide with statistical uncertainty only, masses of the neutral isotopes with combined statistical and systematic uncertainty, the resulting mass excesses, and comparisons with the AME[5] and FRDM[57].

			Mass excess (keV)		
Nuclide	ω_c ratio	Mass (μu)	This work	AME[5]	FRDM[57]
^{64}Ga	1.000120423(50)	63936840.7(35)	-58832.5(33)	-58834.7(40)	-57650
^{64}Ge	1.00019580(51)	63941660(32)	-54344(30)	-54420(250)	-53040

dependent shifts were minimized because all acquisition parameters were identical between ions of different species. Finally, the total systematic uncertainty for the ^{64}Ge experiments is estimated as the sum of the largest two sources of uncertainty: $\triangle m/m = 1{\times}10^{-8} + 8{\times}10^{-9} \sim 2{\times}10^{-8}$.

The systematic uncertainty is combined with the statistical uncertainty in quadrature to arrive at the final masses shown in Table 4.13. As for ^{68}Se, the latest atomic mass evaluation [48] already incorporates preliminary results from this work, so the masses reported in Table 4.13 are compared to the values from the 1995 atomic mass evaluation [5] instead and the FRDM predictions [57]. Good agreement exists with the 1995 AME, but the experimental results show that ^{64}Ga and ^{64}Ge are more bound by 1243 keV on average than predicted by the FRDM.

Although the potential impact of the ^{64}Ge mass on the timescale of the rp-process could be more significant than the contribution from ^{68}Se, surprisingly few measurement attempts have been made. The CPT results disagree with the only other recent measurement, that obtained from the SPEG facility [59], where a mass excess for ^{64}Ge of -53180(640) keV was reported. However, our derived Q_{EC} value for ^{64}Ge of 4489(30) keV (see Eq. A.8) is in excellent agreement with the value of 4410(250) keV reported by Ref. [65] many years ago. Furthermore, the determination of the ^{64}Ga mass reported here is also in good agreement with the 2003 AME which takes as inputs to the evaluation two experimental results, one of which is from the Penning trap mass spectrometer ISOLTRAP. Since the mass determinations of other nuclides by the CPT have been in excellent agreement with preceding precision measurements, we are confident that the results presented here are accurate. While an independent confirmation of our results for the mass of ^{64}Ge would be desirable, no such data is available at present.

Chapter 5

Discussion

During an x-ray burst event, the reaction path is set by thousands of reaction rates, the proton-capture, photodisintegration, and β-decay being the predominant processes. Both the forward and the reverse reactions need to be considered. One example of such a pair of reactions is the proton-capture reaction:

$$^{68}\mathrm{Se} + \mathrm{p} \rightarrow \ ^{69}\mathrm{Br} + \gamma, \tag{5.1}$$

and its inverse reaction:

$$^{69}\mathrm{Br} + \gamma \rightarrow \ ^{68}\mathrm{Se} + \mathrm{p}. \tag{5.2}$$

To fully understand x-ray burst events, both processes must be taken into account. Using statistical and thermodynamic arguments, the two reaction rates are found to be related as shown in Appendix E:

$$\lambda_{\gamma,p}(^{69}\mathrm{Br}) =< \mathrm{p}\ ^{68}\mathrm{Se} > \frac{g(^{68}\mathrm{Se})g(^{1}\mathrm{H})}{g(^{69}\mathrm{Br})} \left(\frac{m(^{68}\mathrm{Se})m(^{1}\mathrm{H})}{m(^{69}\mathrm{Br})}\right)^{3/2} \left(\frac{kT}{2\pi\hbar^2}\right)^{3/2} e^{-Q_p(^{68}\mathrm{Se})/kT}, \tag{5.3}$$

where $\lambda_{\gamma,p}(^{69}\mathrm{Br})$ represents the photodisintegration rate of ^{69}Br and $< \mathrm{p}\ ^{68}\mathrm{Se} >$ represents the proton-capture reaction rate per pair of (p, ^{68}Se) particles. The masses of the nuclides involved are critical since the photodisintegration rate is exponentially dependent upon the proton-capture Q value, Q_p.

As a result of temperatures of $\sim$ 1-2 $\times$ 10^9 K during the x-ray burst, the proton-capture and photodisintegration rates are greater than the β-decay rates of the nuclides involved. Hence, protons are rapidly captured by previously created nuclides

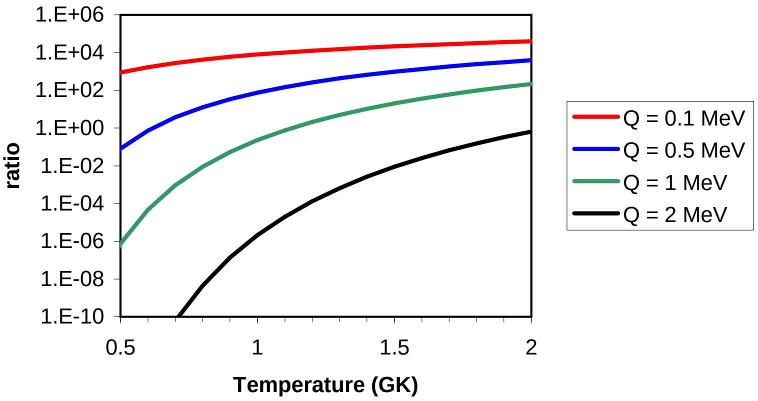

Figure 5.1: Ratio of the photodisintegration rate to the proton-capture rate for ^{68}Se as a function of temperature for various values of the proton-capture Q value.

until the photodisintegration rates become more dominant. Nuclides for which the photodisintegration rates are comparable to the proton-capture rates are those at the proton dripline since little energy, if any at all, is needed to remove a proton from the nucleus. In other words, the photodisintegration rate for nuclides becomes more dominant as the proton separation energy, S_p(Z+1,N) $= -Q_p$(Z,N) approaches zero. Figure 5.1 shows the ratio between the photodisintegration rate and the proton-capture rate for ^{68}Se as a function of temperature for various values of the proton-capture Q value. From Eq. E.32, this ratio is:

$$\frac{\lambda_{\gamma,p}(^{69}\mathrm{Br})}{\lambda_{p,\gamma}(^{68}\mathrm{Se})} = \frac{1}{\rho Y_p N_A} \frac{g(^{68}\mathrm{Se})g(^{1}\mathrm{H})}{g(^{69}\mathrm{Br})} \left(\frac{m(^{68}\mathrm{Se})m(^{1}\mathrm{H})}{m(^{69}\mathrm{Br})}\right)^{3/2} \left(\frac{kT}{2\pi\hbar^2}\right)^{3/2} e^{-Q_p/kT}. \quad (5.4)$$

In generating Fig. 5.1, a value of 1 for the partition functions of ^{68}Se and ^{69}Br and of 2 for ^{1}H was used. The variation in the partition functions with temperature is small and essentially negligible. The mass of the proton used in the calculation is from Ref. [48], the mass of ^{68}Se is taken from this thesis, and the mass of ^{69}Br is determined through the Coulomb displacement energy method which is discussed on p.140. All other constants were taken from Table 5.1 and Table 5.2. With these parameters, for temperatures of 1-2 GK, the photodisintegration rate of the (Z+1,N) nuclide becomes comparable to the proton-capture rate on the (Z,N) nuclide when Q_p is $\sim$ 1-2 MeV.

Once a balance has been reached between the photodisintegration rates on nucleus

(Z+1,N) and proton-capture rates on nucleus (Z,N), an equilibrium is established and consequently the rp-process slows down. At this point, the delay in the rp-process timescale is determined by how quickly the (Z,N) waiting-point nuclide can bypass the (Z+1,N) nuclide. Two possibilities exist. The waiting-point nuclide can either bridge the (Z+1,N) nuclide by capturing two protons in rapid succession, or it can β decay to nucleus (Z-1, N+1) which can then capture protons and continue the rp-process. Therefore, the decay constant, λ, of the waiting-point nuclide is a combination of the β-decay constant, λ_β, and the decay constant resulting from the capture of two protons, $\lambda_{(2\mathrm{p},\gamma)}$, such that:

$$\lambda = \lambda_\beta + \lambda_{(2\mathrm{p},\gamma)}. \tag{5.5}$$

The loss of the (Z,N) nuclide abundance can then be expressed in the usual way (see Eq. C.1), with:

$$\frac{dN(Z,N)}{dt} = -\lambda N(Z,N). \tag{5.6}$$

In chemical and thermodynamic equilibrium as discussed in Appendix E, the (Z,N) and (Z+1,N) nuclides reach an equilibrium abundance. Therefore, the destruction of the (Z,N) waiting-point nuclide by two-proton capture is equivalent to the destruction of the (Z+1,N) nuclide by single-proton capture. In this sense:

$$\frac{dN(Z,N)}{dt} = -(\lambda_\beta + \lambda_{(2\mathrm{p},\gamma)})\ N(Z,N) = -\lambda_\beta N(Z,N) - \lambda_{(\mathrm{p},\gamma)}(Z+1,N)\ N(Z+1,N) \tag{5.7}$$

where $\lambda_{(\mathrm{p},\gamma)}(Z+1,N)$ explicitly indicates that the decay constant due to the proton capture is for nucleus (Z+1,N), not for nucleus (Z,N). Therefore,

$$\lambda_{(2\mathrm{p},\gamma)} = \frac{N(Z+1,N)}{N(Z,N)} \lambda_{(\mathrm{p},\gamma)}(Z+1,N) \tag{5.8}$$

and after using Eq. E.32, we find:

$$\lambda_{(2\mathrm{p},\gamma)} = n_p \frac{g(Z+1,N)}{g(^1\mathrm{H})g(Z,N)} \left(\frac{2\pi\hbar^2}{kT}\right)^{3/2} \left(\frac{m(Z+1,N)}{m(^1\mathrm{H})m(Z,N)}\right)^{3/2} e^{\frac{Q_p}{kT}}\ \lambda_{(\mathrm{p},\gamma)}(Z+1,N). \tag{5.9}$$

Using Eq. E.31, the decay constant due to the proton capture on nucleus (Z+1,N) can be determined:

$$\lambda_{(\mathrm{p},\gamma)}(\mathrm{Z{+}1,N}) = n_p < \mathrm{p},\gamma >_{[^{\mathrm{A+1}}(\mathrm{Z+1})]} . \tag{5.10}$$

The number density of protons, n_p, can be found by considering a mass density $\rho = M/V$ with M representing the total mass of all nuclides within a volume V, and a mass fraction $X_p = M_p/M$ where M_p represents the total mass of all the protons. Using these quantities, the number density of protons:

$$n_p = \rho \frac{X_p}{A_p} N_A = \rho Y_p N_A \tag{5.11}$$

with the atomic mass A_p in units of g·mol^{-1}, and N_A representing Avogadro's constant. The quantity $Y_p = X_p/A_p$ then represents the mole fraction of the protons in units of mol · g^{-1}. By combining Eqs. 5.5, 5.9, 5.10, and 5.11, the total decay constant for the waiting-point nuclide ^{68}Se can be expressed as:

$$\lambda = \lambda_\beta + (\rho Y_p N_A)^2 \frac{g(^{69}\mathrm{Br})}{g(^{1}\mathrm{H})g(^{68}\mathrm{Se})} \left(\frac{2\pi\hbar^2}{kT}\right)^{3/2} \left(\frac{m(^{69}\mathrm{Br})}{m(^{1}\mathrm{H})m(^{68}\mathrm{Se})}\right)^{3/2} e^{\frac{Q_p}{kT}} < \mathrm{p},\gamma >_{[^{69}\mathrm{Br}]} . \tag{5.12}$$

The preceding arguments inherently assume the (Z+1,N) nucleus is bound with $S_p > 0$. For unbound (Z+1,N) nuclides, proton decay occurs much more quickly and the lifetime of the (Z+1,N) is insufficient to continue the rp-process path. However, the lifetime of a *weakly* unbound (Z+1,N) nucleus can be adequate for an additional proton capture to bridge the (Z+1,N) nuclide to a more proton stable (Z+2,N) nuclide. (Nuclides with an even number of protons, ie: even Z, are more stable than those with odd Z due to the pairing effects of the protons). The treatment of proton unstable nuclides is not described here, but a more rigorous and complete derivation found in Ref. [1] shows that Eq. 5.12 is valid for both a bound and unbound (Z+1,N) nucleus provided that an equilibrium is established between the (Z,N) and (Z+1,N) nuclides.

5.1 The waiting-point nuclide ^{68}Se

The effective stellar lifetime of ^{68}Se as determined by Eq. 5.12 is very sensitive to the proton-capture Q value of ^{68}Se. Since the ^{68}Se mass has now been obtained from measurements with the CPT, the difficulty in obtaining a Q_p value for the ^{68}Se(p, γ)^{69}Br reaction now rests with the uncertainty in the ^{69}Br mass. However, the upper limit of the half-life of this nucleus (24 ns) [66] makes a direct measurement of the mass of ^{69}Br with Penning trap mass spectrometers impossible and very difficult with any existing techniques. However, an estimate for the ^{69}Br mass can be obtained by Coulomb energy displacement methods. This method uses the fact that the nuclear strong force essentially does not distinguish between protons and neutrons. Therefore, a pair of nuclei in which the number of protons of one nuclide equals the number of neutrons of the other nuclide and vice versa, should therefore have the same nuclear binding energy. These mirror nuclei, as they are called, not only have identical numbers of nucleons, but also the orbital states occupied by the neutrons of one nucleus are identical to the states occupied by the protons in the other. Thus, the difference in energy between mirror nuclei is due solely to the Coulomb interactions. Once the Coulomb displacement energy, Δ_{CE}, has been calculated, the mass excess of the neutron rich mirror nucleus is simple to calculate as shown below for the mirror nuclei ^{69}Br and ^{69}Se:

$$\Delta(^{69}\mathrm{Br}) = \Delta_{CE} + \Delta(^{69}\mathrm{Se}). \tag{5.13}$$

The Coulomb energies for the relevant nuclei along the rp-process path have been calculated by Brown *et al.* in Ref. [67]. In that article, the proton-capture Q value of ^{68}Se is tabulated using the Coulomb energy displacement method to determine $\Delta(^{69}$Br) (ie: Eq. 5.13). Most Q_p values reported in Ref. [67] were determined using the 1995 Atomic Mass Evaluation (1995 AME [5]) for the masses of the N=Z nuclei and the neutron-rich partners of the mirror nuclei. In this work, the Q_p value for ^{68}Se was reevaluated to account for our mass measurements and the most recent mass

Table 5.1: Fundamental constants and other constants used for x-ray burst model calculations.

Constant used	Value
Y_p	$^a0.771$ mol/g
ρ	$^a10^6$ g/cm^3
^bN_A	$6.0221415 \cdot 10^{23}$ mol^{-1}
$^b\hbar$	$6.58211915 \cdot 10^{-16}$ eV·s
^bk	$8.617343 \cdot 10^{-5}$ eV/K
^bc	$2.99792458 \cdot 10^{10}$ cm/s

a) Commonly used value for x-ray burst models. See Ref. [1] for example.

b) Obtained from [56].

evaluation (AME [48]) as such:

$$
\begin{aligned}
Q_p = Q_{p[67]} &- [\Delta(^{68}\mathrm{Se})_{1995AME} - \Delta(^{68}\mathrm{Se})_{CPT}] \\
&- [\Delta(^{1}\mathrm{H})_{1995AME} - \Delta(^{1}\mathrm{H})_{AME}] \\
&+ [\Delta(^{69}\mathrm{Se})_{1995AME} - \Delta(^{69}\mathrm{Se})_{AME}]
\end{aligned}
\tag{5.14}
$$

with the subscripts indicating the source of the respective quantity. The uncertainty in the new Q_p value is calculated using:

$$
\delta Q_p = \sqrt{(\delta\Delta_{CE})^2 + [\delta\Delta(^{69}\mathrm{Se})]^2 + [\delta\Delta(^{68}\mathrm{Se})]^2 + [\delta\Delta(^{1}\mathrm{H})]^2}, \tag{5.15}
$$

where the uncertainty in the calculated Coulomb displacement energy is 100 keV as quoted in Ref. [67]. In the case of the $^{68}\mathrm{Se}(\mathrm{p},\gamma)^{69}\mathrm{Br}$ reaction, the new calculated Q_p value is -810(110) keV which is consistent with a determination of the upper limit of the ^{69}Br half-life (24 ns) suggesting that it is proton unbound by at least 500 keV [66].

The effective stellar half-life of ^{68}Se, $t_{1/2,eff}(^{68}\mathrm{Se}) = \ln(2)/\lambda$, can be determined from Eq. 5.12 using our mass measurements along with the values shown in Table 5.1 and Table 5.2. Although the proton-capture rates are also dependent upon the masses of the nuclides involved, new rates were not calculated as the impact of the masses reported here is expected to be negligible in comparison to the exponential

Table 5.2: Constants used for x-ray burst model calculations of ^{68}Se. Only the uncertainties used in calculations are shown in parentheses. All other uncertainties are neglected.

	^{68}Se	^{69}Se	^{70}Se	^{69}Br	^{70}Kr
^{a,d}w	1.01			1.19	1.14
^{b}J$_o$	0			$\frac{1}{2}$	0
$^{b}\Delta$ (keV)		-56300(30)	-62050(60)		
$^{c,d}N_A$ <p, γ> (cm^3 s^{-1} mol^{-1})				0.0522	

a) Obtained from [68].

b) Obtained from [48].

c) Obtained from [1].

d) This temperature dependent value is for T=1.5GK.

factor. The temperature dependent partition functions, g, were collected from Ref. [68] and are reported as normalized partition functions, w, such that:

$$g = w(2J_o + 1) \tag{5.16}$$

where J_o represents the nuclear spin of the ground state. Therefore, the normalized partition functions from Ref. [68] were used in conjunction with the spins of the ground states obtained from Ref. [48] to arrive at the true partition functions, g, needed in Eq. 5.12. In addition, a β-decay half-life of $\ln(2)/\lambda_{beta} = 35.5$ s [69] was used.

The effect of our mass determination of ^{68}Se on its effective stellar half-life, as compared with other groups, can be seen in Fig. 5.2. The original mass measurement of ^{68}Se by CSS2 suggests that the effective stellar half-life of ^{68}Se is less than 1 ms; a recent remeasurement of the ^{68}Se mass by CSS2 (CSS2 2003) [62] revises the previous suggestion to 25 s. A relatively imprecise value from SPEG indicates the effective stellar half-life ranges from less than 1 ms to 34 s. Quite a variation exists indeed! A recently published β-decay measurement of ^{68}Se with the FMA apparatus [60] determined the ^{68}Se mass and indicated the effective stellar half-life of ^{68}Se is about 7 s when using the 2003 AME for the ^{69}Br mass. Our precise result, when combined with the ^{69}Br mass using Coulomb displacement energy methods, suggests

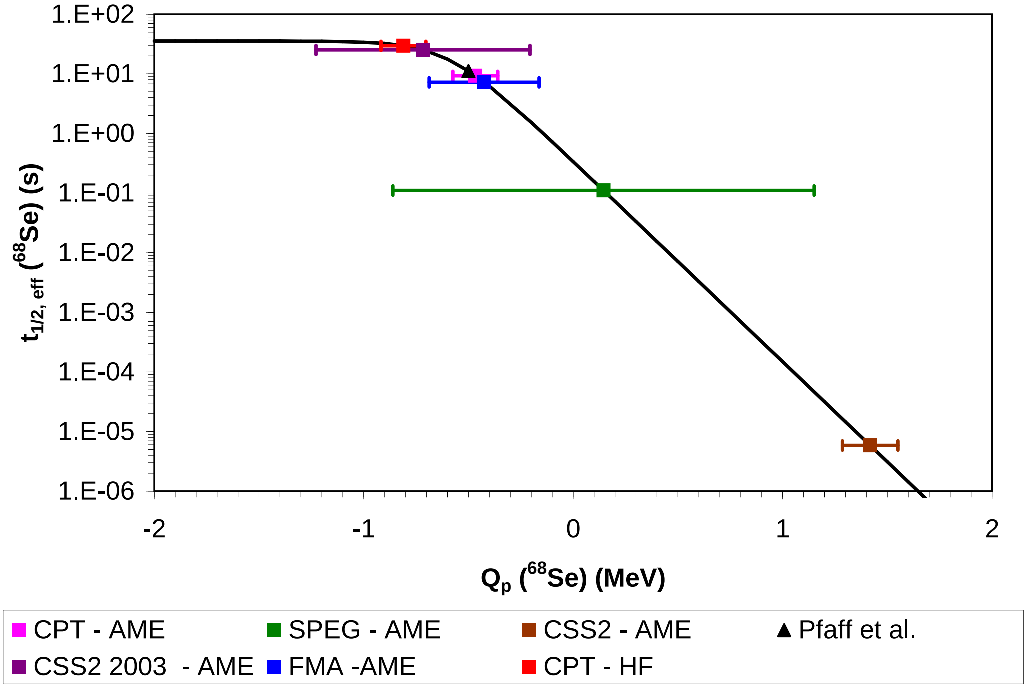

Figure 5.2: The effective stellar half-life of ^{68}Se as a function of $Q_p(^{68}\mathrm{Se})$. For the datum points with a two-part legend entry, the first part represents the values used for the mass of ^{68}Se, and the second part indicates the value used for the mass of ^{69}Br. Also shown is the upper limit for $Q_p(^{68}\mathrm{Se})$ as determined by Pfaff *et al.* [66]. The curve was calculated under conditions typical for x-ray burst models (temperature of 1.5 GK, density of 10^6 g cm^{-3}, solar hydrogen abundance).

the effective stellar half-life of ^{68}Se is between 24 and 33 seconds which is consistent with the upper limit of $Q_p(^{68}\mathrm{Se})$ proposed by Pfaff *et al.* [66]. Our result for the mass of ^{68}Se is the most precise and accurate to date and strongly suggests ^{68}Se is a true waiting-point nuclide and that the rp-process will be delayed at this point.

At stellar temperatures higher than 1.5 GK, the photodisintegration of ^{70}Kr is not negligible and the waiting-point nuclide ^{68}Se establishes an equilibrium with both ^{69}Br and ^{70}Kr. In this scenario, the delay in the rp-process at ^{68}Se is determined by the β-decay rates of both ^{68}Se and ^{70}Kr, such that:

$$\frac{dN(^{68}\mathrm{Se})}{dt} = -\lambda_\beta(^{68}\mathrm{Se})N(^{68}\mathrm{Se}) - \lambda_\beta(^{70}\mathrm{Kr})N(^{70}\mathrm{Kr}), \tag{5.17}$$

where $\lambda_\beta(^{68}\mathrm{Se})$ signifies the β-decay rate of ^{68}Se and similarly for ^{70}Kr. Therefore, the β-decay lifetime of ^{70}Kr becomes important in determining the effective stellar half-life of ^{68}Se. Since ^{70}Kr is in equilibrium with both ^{69}Br and ^{68}Se, the abundance of ^{70}Kr can be determined by noting that:

$$N(^{70}\mathrm{Kr}) = \frac{N(^{70}\mathrm{Kr})}{N(^{69}\mathrm{Br})}\,\frac{N(^{69}\mathrm{Br})}{N(^{68}\mathrm{Se})}\,N(^{68}\mathrm{Se}), \tag{5.18}$$

and with the help of Eq. E.32, we find:

$$N(^{70}\mathrm{Kr}) = n_p^2 \frac{g(^{70}\mathrm{Kr})}{g^2(^{1}\mathrm{H})g(^{68}\mathrm{Se})}\left(\frac{2\pi\hbar^2}{kT}\right)^3\left(\frac{m(^{70}\mathrm{Kr})}{m^2(^{1}\mathrm{H})m(^{68}\mathrm{Se})}\right)^{3/2} e^{\frac{Q_p(^{68}\mathrm{Se})+Q_p(^{69}\mathrm{Br})}{kT}}\, N(^{68}\mathrm{Se}). \tag{5.19}$$

If Eq. 5.17 is rewritten as:

$$\frac{dN(^{68}\mathrm{Se})}{dt} = -\lambda N(^{68}\mathrm{Se}) \tag{5.20}$$

where:

$$\lambda = \lambda_\beta(^{68}\mathrm{Se}) + \lambda_\beta(^{70}\mathrm{Kr})\frac{N(^{70}\mathrm{Kr})}{N(^{68}\mathrm{Se})}, \tag{5.21}$$

then the effective stellar decay constant, λ, can be determined with Eq. 5.19 and Eq. 5.11 to be:

$$\begin{aligned}\lambda = {} & \lambda_\beta(^{68}\mathrm{Se}) \\ & + \lambda_\beta(^{70}\mathrm{Kr})(\rho Y_p N_A)^2 \frac{g(^{70}\mathrm{Kr})}{g^2(^{1}\mathrm{H})g(^{68}\mathrm{Se})}\left(\frac{2\pi\hbar^2}{kT}\right)^3\left(\frac{m(^{70}\mathrm{Kr})}{m^2(^{1}\mathrm{H})m(^{68}\mathrm{Se})}\right)^{3/2} e^{\frac{Q_{2p}(^{68}\mathrm{Se})}{kT}},\end{aligned} \tag{5.22}$$

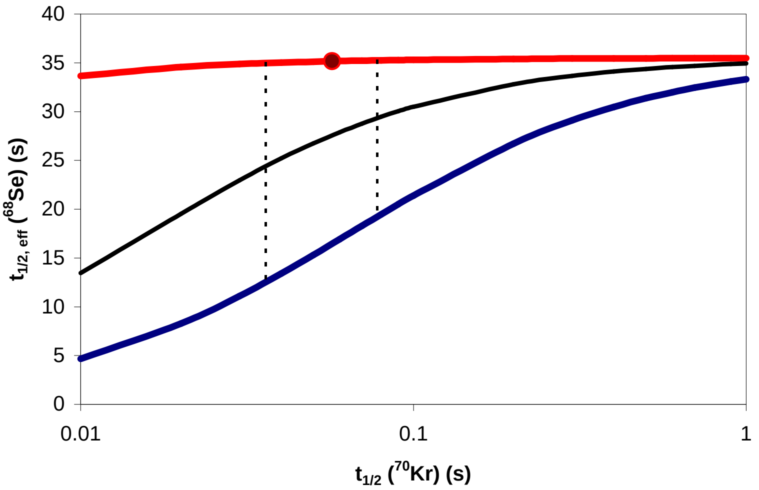

Figure 5.3: The effective stellar half-life of ^{68}Se as a function of the half-life of ^{70}Kr for three values of $Q_{2p}(^{68}\mathrm{Se})$: 1.95 MeV (blue curve), 1.32 MeV (red curve), and 1.77 MeV (black curve). The datum point shown indicates the known half-life of ^{70}Kr [70] with its uncertainty represented by the vertical dashed lines.

which is similar to Eq. 43 in Ref. [1]. Note that the two-proton-capture Q value (see Appendix A) is given by:

$$Q_{2p}(^{68}\mathrm{Se}) = Q_p(^{68}\mathrm{Se}) + Q_p(^{69}\mathrm{Br}) = \Delta(^{68}\mathrm{Se}) + 2\Delta(^{1}\mathrm{H}) - \Delta(^{70}\mathrm{Kr}), \tag{5.23}$$

and since the total stellar decay constant is exponentially dependent upon Q_{2p}, a precise knowledge of the masses of ^{70}Kr and ^{68}Se is required. Once again, Eq. 5.22 assumes that the intermediate ^{69}Br nucleus is bound, but it is valid for unbound intermediate nuclei as well. (See Ref. [1] for a more rigorous derivation.)

The effective stellar half-life of ^{68}Se can now be calculated with Eq. 5.22 and constants from Table 5.1 and Table 5.2. As shown in Fig. 5.3, the recent ^{70}Kr half-life measurement of 57(21) ms [70] could significantly affect the effective stellar half-life of ^{68}Se if $Q_{2p}(^{68}\mathrm{Se})$ = 1.95 MeV is used as in Ref. [70]. In their paper, the value for $Q_{2p}(^{68}\mathrm{Se})$ was determined by adding together the $Q_p(^{68}\mathrm{Se})$ value of -450 keV from Ref. [71] to the $Q_p(^{69}\mathrm{Br})$ value of 2400 keV from the FRDM [57]. However, the uncertainty in $Q_{2p}(^{68}\mathrm{Se})$ is important since the effective stellar half-life of ^{68}Se is exponentially dependent upon this quantity under the assumed conditions. For the purposes of this thesis, the tabulated values for Q_{2p} in Ref. [67], which were generated using the Coulomb displacement energy method, are adjusted to account for the new CPT mass measurements as follows:

$$\begin{aligned} Q_{2p} = Q_{2p[67]} &- [\Delta(^{68}\mathrm{Se})_{1995AME} - \Delta(^{68}\mathrm{Se})_{CPT}] \\ &- 2[\Delta(^{1}\mathrm{H})_{1995AME} - \Delta(^{1}\mathrm{H})_{AME}] \\ &+ [\Delta(^{70}\mathrm{Se})_{[72]} - \Delta(^{70}\mathrm{Se})_{AME}] \end{aligned} \tag{5.24}$$

with the subscripts indicating the source of the respective quantity. Our original paper was published prior to the release of the 2003 AME (labelled as AME in Eq. 5.24) and in a manner consistent with Ref. [67], a mass excess for ^{70}Kr of -61604(120) keV from Ref. [72] was used instead of the more imprecise value from the 1995 AME. The resulting $Q_{2p}(^{68}\mathrm{Se})$ is this case is 1.33(16) MeV, where the uncertainty in the new Q_{2p} value:

$$\delta Q_{2p} = \sqrt{(\delta\Delta_{CE})^2 + [\delta\Delta(^{70}\mathrm{Se})]^2 + [\delta\Delta(^{68}\mathrm{Se})]^2 + [2 \cdot \delta\Delta(^{1}\mathrm{H})]^2}. \tag{5.25}$$

(A value of 100 keV was used as an estimate for the uncertainty in the Coulomb displacement energy calculations [67].) If the $Q_{2p}(^{68}\mathrm{Se})$ value of 1.33 MeV is used in Eq. 5.22, the effective stellar half-life of ^{68}Se is insensitive to the ^{70}Kr half-life as seen in Fig. 5.3, and as stated in the original publication, " ... a $Q_{2p}(^{68}\mathrm{Se})$ of 1.75 MeV would be required to reduce the effective stellar half-life of ^{68}Se by 20%, which is well outside our combined theoretical and experimental uncertainty." [73]. However, the recent atomic mass evaluation indicates the ^{70}Se mass excess from Ref. [72] disagrees with other well documented data from Ref. [59] and Ref. [63]. The results from the latter two publications carry more weight in determining the mass excess of ^{70}Se as -62050(60) keV. Using this mass excess in Eq. 5.24, the result for $Q_{2p}(^{68}\mathrm{Se}) = 1.77(12)$ MeV, and the effective stellar half-life of ^{68}Se is reduced by roughly 23%. Therefore, under the assumed conditions, the photodisintegration rate of ^{70}Kr is not entirely negligible as first reported in Ref. [73], but ^{68}Se remains to be a true waiting-point nuclide and poses a significant delay in the rp-process.

5.2 The waiting-point nuclide ^{64}Ge

The total timescale of the rp-process depends, to a large extent, upon the sum of the individual delays at each waiting-point nuclide. Since the maximum possible delay at each waiting-point nuclide is governed by its β-decay rate, ^{64}Ge, with a β-decay half-life of 63.7(25) s [48], could potentially contribute a larger delay to the rp-process timescale than ^{68}Se. Once again, Eq. 5.12 is used to determine the effective stellar half-life of ^{64}Ge, where the data for ^{68}Se and ^{69}Br are replaced by that for the nuclides ^{64}Ge and ^{65}As. To determine the Q_p value for the ^{64}Ge(p,γ)^{65}As reaction, both the masses of ^{64}Ge and ^{65}As are needed. The mass of ^{64}Ge has been measured with the CPT and is reported in this thesis. However, during this measurement, no attempt was made to measure the mass of ^{65}As for a couple of reasons. First, the time available was insufficient to obtain the masses of both ^{64}Ge and ^{65}As, because of the time spent in achieving the required mass precision for ^{64}Ge. Second, the mass resolution to remove contaminant ions, necessary to minimize systematic effects, required much more time than the 126-ms half-life [74] of ^{65}As. The small number of ^{65}As ions left after the cleaning processes would have been significantly reduced from the already low production rates. Since the measurement of ^{64}Ge, the efficiency and speed of the apparatus has improved to the point that a mass measurement of ^{65}As with the CPT may now be possible. For now, however, an estimate for Q_p(^{64}Ge) can be determined from the combination of the ^{64}Ge mass measured with the CPT, the mass of ^{65}Ge from the 2003 AME, and the Coulomb displacement energy calculations from Ref. [67]. With the help of Eq. 5.14 and Eq. 5.15, after substitution of appropriate values, the proton-capture Q-value is found to be -340(140) keV.

The dependence of the effective stellar half-life of ^{64}Ge upon the proton-capture Q-value (Fig. 5.4) was generated in a similar manner as for ^{68}Se. If the value for Q_p is determined using the mass of ^{64}Ge from Ref. [59] and the ^{65}As mass from the 2003 AME, then the effective stellar half-life of ^{64}Ge is less than 1 ms. However, our

Table 5.3: Constants used for x-ray burst model calculations of ^{64}Ge. Only the uncertainties used in calculations are shown in parentheses. All other uncertainties are neglected.

	^{64}Ge	^{65}Ge	^{66}Ge	^{65}As	^{66}Se
^{a,d}w	1.01			1.31	1.00
^{b}J$_o$	0			$\frac{3}{2}$	0
$^{b}\Delta$ (keV)		-56410(100)	-61620(30)		
$^{c,d}N_A$ <p, γ> (cm^3 s^{-1} mol^{-1})				0.246	

a) Obtained from [68].

b) Obtained from [48].

c) Obtained from [1].

d) This temperature dependent value is for T=1.5GK.

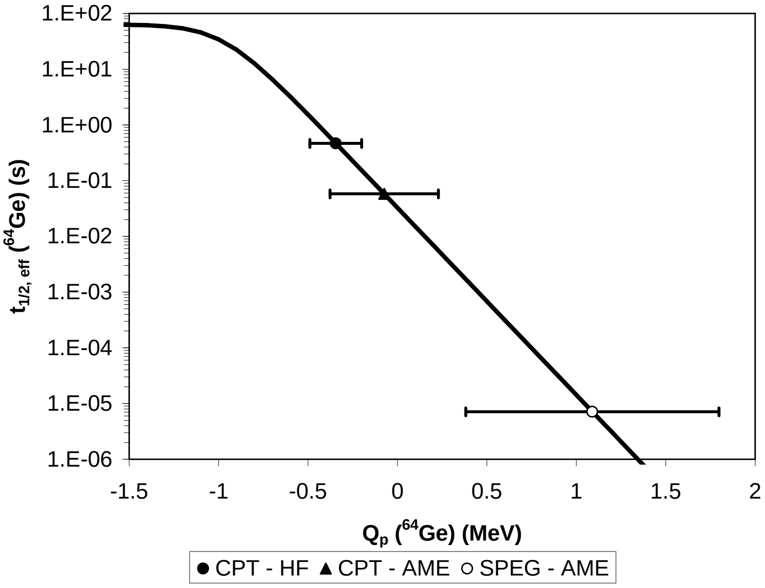

Figure 5.4: The effective stellar half-life of ^{64}Ge as a function of Q_p(^{64}Ge). For the datum points with a two-part legend entry, the first part represents the values used for the mass of ^{64}Ge, and the second part indicates the value used for the mass of ^{65}As. The curve was generated using identical parameters to those used in making Fig. 5.2.

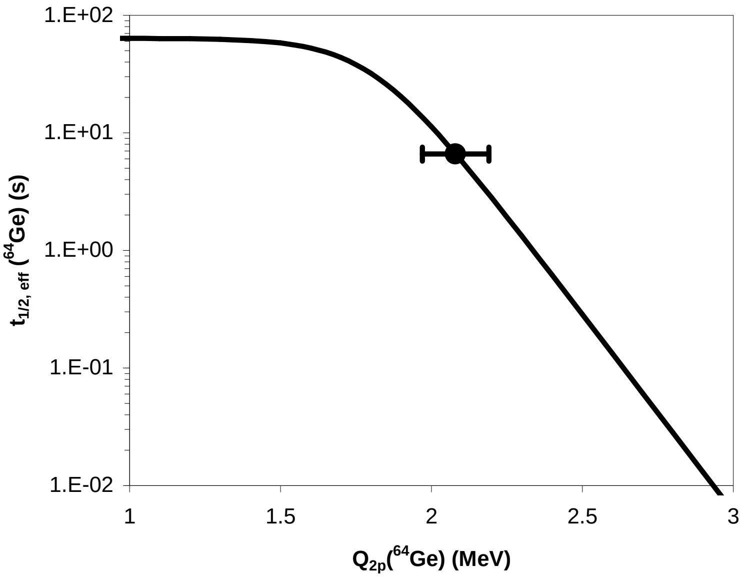

Figure 5.5: The effective stellar half-life of ^{64}Ge as a function of Q_{2p}(^{64}Ge) accounting for the photodisintegration of ^{66}Se. The datum point shown represents the Q_{2p} value of ^{64}Ge obtained from the CPT measurement of ^{64}Ge in conjunction with the mass of ^{66}Se derived from Coulomb displacement energy methods. In comparison with Fig. 5.4, the effective stellar half-life of ^{64}Ge is extended due to the high photodisintegration rate of ^{66}Se at a temperature of 1.5 GK which is assumed here.

much more precise result, combined with the mass calculation of ^{65}As obtained with Coulomb displacement energy methods, suggests the effective stellar half-life of ^{64}Ge is between 0.2 and 1.4 seconds. Therefore, the rp-process seems to encounter a small delay at ^{64}Ge, but not nearly as significant as the delay at ^{68}Se.

At a temperature of 1.5 GK which has been assumed for the previous calculations, the photodisintegration rate of ^{66}Se cannot be neglected. Therefore, the destruction of the waiting-point nuclide ^{64}Ge simply by two-proton capture to ^{66}Se is not sufficient. Only through the β decay of ^{64}Ge or ^{66}Se can the rp-process emerge from the ^{64}Ge-^{66}Se equilibrium. From Eq. 5.22, with the substitution of the appropriate parameters for ^{64}Ge and ^{66}Se, the contribution of the photodisintegration rate of ^{66}Se to the rp-process timescale has been determined (see Fig. 5.5). As usual, the values for the constants were taken from Table 5.1 and Table 5.3 and the Q_{2p} value for ^{64}Ge was determined from Coulomb displacement energy methods as described in the derivation of Eq. 5.24. With our value for the mass of ^{64}Ge, in addition to the ^{66}Se mass from Ref. [48], the value for $Q_{2p}(^{64}\text{Ge})$ was found to be 2080(110) keV. Due to the resultingly high photodisintegration rate of ^{66}Se, the effective stellar half-life of ^{64}Ge can be extended to as long as 14 s with our current uncertainties in the $Q_{2p}(^{64}\text{Ge})$ value. Under the assumed conditions, then, ^{64}Ge is indeed a waiting-point nuclide and the delay in the rp-process timescale at ^{64}Ge is significant.

Chapter 6

Summary and outlook

X-ray bursts are thought to originate in binary star systems consisting of a gas giant and a neutron star. The burst is observed as a result of a thermonuclear runaway which occurs on the surface of the neutron star after sufficient quantities of hydrogen and helium have accreted from the gas giant. During the thermonuclear runaway, heavier elements are produced via a series of rapid proton-capture reactions between the abundantly available hydrogen and the ashes on the surface of the neutron star. The reaction path is dictated by thousands of reaction rates, predominantly those of proton capture, photodisintegration, and β decay. Along the rp-process path, waiting-point nuclides are encountered in which a balance is reached between the fast proton capture and photodisintegration reactions. At these points, the rp-process cannot continue and must wait for the destruction of the waiting-point nuclide through its β decay or via two-proton capture to bridge the impeding nucleus. The total timescale of the rp-process, or x-ray burst, is essentially determined by the sum of the individual delays encountered at each waiting-point nuclide. Since the photodisintegration rates are exponentially dependent upon the proton-capture Q values of the nuclides involved, precise mass information is one of the most important pieces of knowledge required to identify and determine the delay at each waiting-point nuclide.

The difficulty in measuring the masses of waiting-point nuclides arises from their short-lived nature and their unnatural supply on Earth. The production of these isotopes by accelerator facilities with current technology is limited, such that any successful mass measurement demands an efficient and fast delivery system. The CPT mass spectrometer was designed with these requirements in mind. Each component of the rather complicated apparatus meets at least one objective in obtaining precise and accurate mass measurements of short-lived, weakly produced isotopes. To date, more than 60 nuclides have been measured with the CPT, including nuclides along areas of the rp-process path where mass information is needed the most: the waiting-point nuclides ^{68}Se and ^{64}Ge.

Reported here are substantially improved values for the masses of ^{68}Se and ^{64}Ge. To determine the proton-capture Q values which heavily influence the photodisintegration reactions in the rp-process, the additional masses of ^{69}Br, ^{70}Kr, ^{65}As, and ^{66}Se were most reliably obtained by calculations based upon isospin symmetry which inherently cannot provide mass values for ^{68}Se and ^{64}Ge. Our precise mass measurements of ^{68}Se and ^{64}Ge, in combination with these calculations, find both ^{68}Se and ^{64}Ge to be waiting-point nuclides which present considerable delays in the rp-process.

The outlook for the CPT looks very promising. Evolution of the apparatus from its early days at Chalk River Laboratories has resulted in a fast, efficient system which produces both precise and accurate mass measurements. The evolution continues and as this document was being written, measurements with the CPT, having even higher precision than those reported here, were performed with nuclides of shorter half-lives [49, 75].

In the quest to push the system to make measurements of even more rare, short-lived nuclides with ever-increasing accuracy, the CPT apparatus is continually being modified. During the writing of this document, a new isotope separator was being installed which is similar to the previous one, but with the magnetic field supplied by a 7 Tesla superconducting magnet (see Fig. 6.1). A mass resolving power greater than 100,000 is expected which will make this device a true isobar separator, not just an isotope separator. The buffer gas pressure will also be independently controlled, as

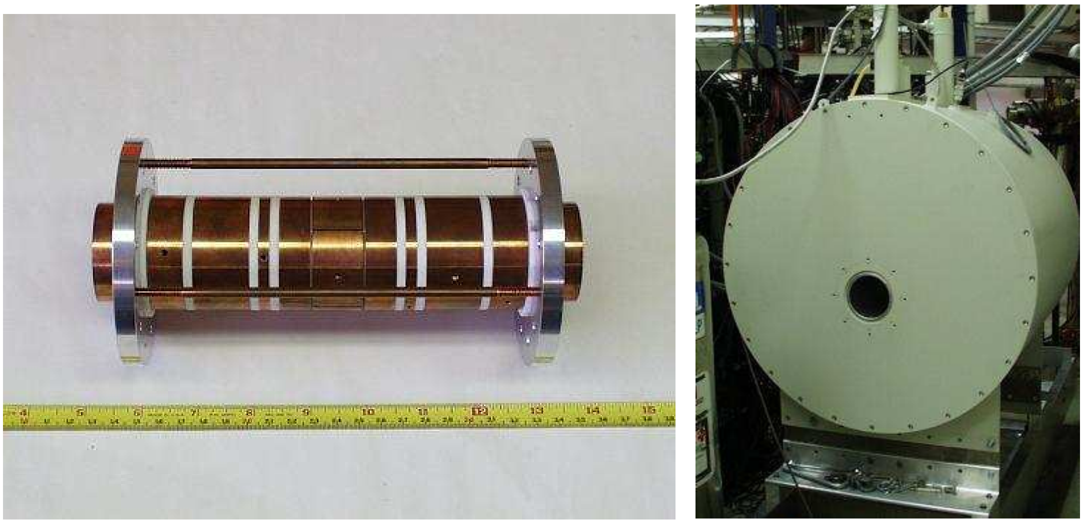

Figure 6.1: The new isobar separator. At the left is a picture of the cylindrical Penning trap which will be installed in the 7 Tesla magnet shown on the right.

opposed to the current design in which the pressure in the trap volume is controlled by a balance of pumping speed and choice of apertures. Converting the room temperature Paul trap to a cryogenically-cooled one will produce an ion bunch with an energy spread conducent to a more efficient transfer of ions to the Penning trap, and the ions will subsequently probe a smaller extent of the trap volume which will yield more accurate measurements. In addition, the circuitry which applies radio-frequency voltage to the linear trap has recently been altered to allow a more flexible range of operating frequencies, as opposed to the limited selection of frequencies earlier. This enhancement permits a more efficient accumulation of ions at all masses. Operating the Enge spectrograph in gas-filled mode will allow the collection of more than just one charge state in the gas catcher. The degrader is also seeing a facelift. It is being transformed from the ladder-like structure described previously to a set of two wheels which can be placed closer to the gas catcher window. (See Fig. 6.2.) On each wheel will be four foils of different thicknesses, selectable by rotating the wheel to a prescribed position. The different combinations of foils from the two wheels will provide a range of quantized effective foil thicknesses. The foils themselves will be circular, in approximate size to the gas catcher itself as opposed to the current design of

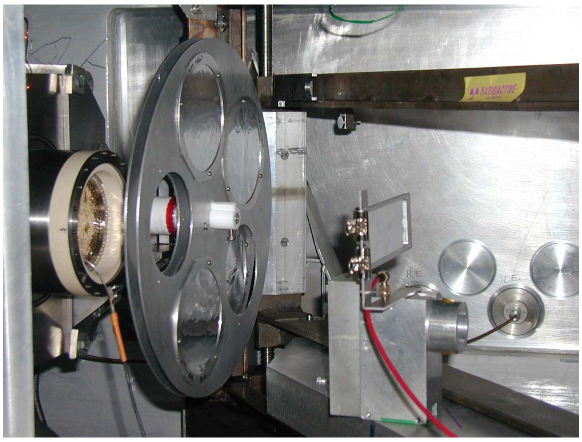

Figure 6.2: A look at the new degrader system inside the Enge spectrograph. The window of the gas catcher can be seen to the left of the degrader wheels.

rectangular foils which does not cover the entire gas catcher entrance. The magnetic field of the 5.9 Tesla superconducting magnet used for precision mass measurements was found not to be as homogeneous as desired, due mainly to the malfunction of 3 shim coils and 2 superconducting shunts. Since the magnet is extremely stable, and not susceptible to external pressure variations, the option of disposing it for a newer magnet with reduced stability is not being considered. Having the magnet repaired is also not an option, due in part, to unsuccessful attempts in the past with similar magnets. Instead, external correction coils, strapped to the outside of the vacuum chamber is an option being pursued. Ultimately, the decision will be made after consideration of the precision desired, and the risks assessed with all options. The process of removing contaminant ions has recently been modified. Previously, as done with the measurements reported here, the undesired ions were removed with a sequence of dipole field excitations, each frequency for a specific ion. Now contaminant ions are removed with the simultaneous application of all required frequencies. This new method saves valuable time and decreases the number of desired ions lost via radioactive decay. In addition, the square envelope of the original cleaning process was replaced with a Blackmon envelope, resulting in more power applied at the desired frequency and less power at the sidebands. In this manner, the interference of the cleaning frequencies upon the ions to be measured is significantly reduced. As a consequence, less resolution, and therefore a smaller duration of the dipole field excitation, is required to remove the unwanted ions. A large loss in efficiency occurs in the last stage of the apparatus – the final MCP detector. Its efficiency has been estimated to be 25%. Investigation of other microchannel plate designs suggest a wire grid in front of the first plate at an appropriate potential will increase the likelihood of ion detection. Floating the entire plate assembly to high voltage is also desirable. In this manner, ions will accelerate to the plate and strike it with much higher kinetic energy which will result in improved efficiency. As the precision of measurements becomes comparable to the accuracy obtained, a closer examination of the functions used to fit the data is essential. A more general function which includes the possibility of asymmetrical effects in its structure is desired since the Penning trap is never perfectly tuned and the resulting asymmetrical effects are noticed at high mass resolution. Furthermore, the deviations in the cyclotron frequencies determined by fitting to varying frequency ranges and increments should be investigated. Finally, further automation of the acquisition system is necessary both for effortless operation and to prevent human error. As the system has become more complicated, more time than necessary is sacrificed in performing routine tasks. A genuine effort should be exercised on automation before any other changes are made. The relatively brief amount of time spent automating the system in the beginning will yield a more efficient use of time in the long run. Overall, the modifications as described will increase not only the precision, but perhaps more importantly the accuracy, of future mass measurements of an extended set of rare, short-lived isotopes.

Soon to be within the reach of the CPT are measurements of ^{65}As, and more proton-rich nuclides along the rp-process path. Of the three most critical waiting-point nuclides (^{72}Kr, ^{68}Se, and ^{64}Ge), the proton-capture Q value for ^{64}Ge now has the largest uncertainty, due to the uncertainty in the mass of ^{65}As. Scientific investigations, including those of the astrophysical r-process and of tests of the CKM matrix unitarity, have motivated other mass measurements with the CPT. Mass measurements will continue to play an important role in nuclear physics and astrophysics. The advances in techniques and technology have driven the field to new heights, but as US economist and social philosopher Thorstein Veblen once said:

> *"The outcome of any serious research can only be to make two questions grow where only one grew before."*

Appendix A

Atomic masses, Q values, and Einstein

Consider the following reaction:

$$p + t \rightarrow r \tag{A.1}$$

in which particles 'p' and 't' fuse together to create particle 'r'. The Q value of the reaction is defined as the difference in mass energy between the initial and final particles such that:

$$Q = (m_p + m_t - m_r)\ \mathrm{c}^2 \tag{A.2}$$

where c refers to the speed of light in vacuum. To obtain Q in energy units, the well-known relation between mass and energy derived by Einstein in 1905 [76] was used. The Q value is therefore a measure of the energy released in the reaction. If the Q value is positive, the reaction is exothermic; if the Q value is negative, the reaction is endothermic. For example, if the reaction involves the capture of a proton by $^{\mathrm{A}}\mathrm{Z}_{\mathrm{N}}$ to produce $^{\mathrm{A+1}}(\mathrm{Z+1})_{\mathrm{N}}$, ie:

$$^{\mathrm{A}}\mathrm{Z}_{\mathrm{N}} +^{1}\mathrm{H} \rightarrow\ ^{\mathrm{A+1}}(\mathrm{Z+1})_{\mathrm{N}}, \tag{A.3}$$

then the Q value of the reaction, identified as the proton-capture Q value, or Q_p value, is simply determined by with:

$$Q_p = \{m(^{\mathrm{A}}\mathrm{Z}_{\mathrm{N}}) + m(^1\mathrm{H}) - m(^{\mathrm{A+1}}[\mathrm{Z+1}]_{\mathrm{N}})\}\mathrm{c}^2, \tag{A.4}$$

where all masses are the neutral, or atomic, masses. Since the mass excess, Δ, is defined as:

$$\Delta = (m_u - \mathrm{A}_u)\ b\ \mathrm{c}^2, \tag{A.5}$$

where the atomic mass, m_u, and the mass number, A_u, are both in unified mass units, u, and the conversion factor $b = 1.66053873(13) \times 10^{-27}$ kg / u [48], then Eq. A.4 can be rewritten in terms of the mass excesses as:

$$Q_p = \Delta(^{\mathrm{A}}\mathrm{Z}_{\mathrm{N}}) + \Delta(^1\mathrm{H}) - \ \Delta(^{\mathrm{A+1}}(\mathrm{Z+1})_{\mathrm{N}}). \tag{A.6}$$

An electron capture reaction is another reaction to consider, where a nucleus converts a proton to a neutron by capturing an atomic electron which is in close proximity to the nucleus. Since this reaction can be expressed as:

$$^{\mathrm{A}}\mathrm{Z}_{\mathrm{N}} \rightarrow\ ^{\mathrm{A}}(\mathrm{Z\text{-}1})_{(\mathrm{N+1})}, \tag{A.7}$$

the electron-capture Q value, Q_{EC}, can be written in terms of the mass excesses as:

$$Q_{EC} = \Delta[^{\mathrm{A}}\mathrm{Z}_{\mathrm{N}}] - \Delta[^{\mathrm{A}}(\mathrm{Z\text{-}1})_{(\mathrm{N+1})}]. \tag{A.8}$$

The Q values for other types of reactions are determined in the same manner as the examples given above.

Appendix B

Time of flight

Much of the CPT system involves the transfer of cooled ion bunches from one device to another. Following the ejection of an ion bunch from one of these devices, such as a Paul trap or Penning trap, the ion bunch travels through an electrostatic beam transport system and individual ions arrive at the next position after a time dependent upon their mass. As the ions are often cooled with helium gas within these devices, they exit with the same charge state, q, and with roughly the same energy. The ions are then accelerated through a potential difference V and gain kinetic energy E given by:

$$E = qV = \frac{1}{2}mv^2. \tag{B.1}$$

In a region with no external forces (ie: within a drift tube) the velocity of each ion remains constant. Therefore, to travel a distance d, the ions take a time t given by:

$$qV = \frac{1}{2}m\left(\frac{d}{t}\right)^2 \Rightarrow t = d\sqrt{\frac{m}{2qV}}. \tag{B.2}$$

For all ions which are accelerated through a potential V, they reach a position at distance d at a time dependent upon the square root of the mass to charge ratio. Therefore, an ion with mass m will take half the time to reach the position as an ion with mass $4m$.

Appendix C

Radioactive decay

Radioactive decay is a statistical process. For a sample of N nuclei at time t, the number of nuclei of a particular state which decay per unit time into another state is proportional to N:

$$\frac{dN}{dt} = -\lambda N, \tag{C.1}$$

assuming no new nuclei are introduced into the sample. The Greek letter λ is the proportionality constant and is termed the disintegration or decay constant. Due to the statistical nature of radioactive decay, the exact moment at which a specific atom will disintegrate is impossible to predict. Instead, we can only describe the probability with which a specific nucleus will decay within a particular time interval.

The number of nuclei at a time t can be obtained by integrating Eq. C.1:

$$N = N_o e^{-\lambda(t-t_o)} \tag{C.2}$$

where N_o is the number of nuclei at time t_o. This relation is known as the exponential decay law. The half-life, $t_{1/2}$, is a term which is used to describe the amount of time for half of the sample of N nuclei to decay. Returning to Eq. C.2, the relation between the half-life and decay constant can be determined by substituting $\frac{1}{2}N$ for N and $t_o + t_{1/2}$ for t. The result is that:

$$t_{1/2} = \frac{\ln(2)}{\lambda}. \tag{C.3}$$

Owing to the difficulty in measuring the number of nuclei within a sample, a more practical use of Eq. C.1 is to measure the number of decays, or activity A of the sample. In this manner,

$$A = \lambda N. \tag{C.4}$$

Equation C.1 was obtained assuming no new nuclei were introduced into the sample. Often, however, as in the production of nuclei in an accelerator facility, new nuclei are introduced into the sample at a constant rate R. In this situation, the number of nuclei in the sample follows the relationship:

$$dN = Rdt - \lambda N dt \tag{C.5}$$

with solution:

$$N = \frac{R}{\lambda}(1 - e^{-\lambda t}). \tag{C.6}$$

Appendix D

χ_R^2 and propagation of errors

The χ_R^2 test is an established test for determining how well a particular function fits to a given set of data. Essentially, this test determines the ratio between the squared differences of the datum points from the fitted function to the squared uncertainties of the individual datum points. The function is said to fit well to the data if the sum of these ratios over the entire set of data, when divided by the number of free parameters, is equal to 1.

Consider a set of N datum points y_i with independent uncertainties σ_i as a function of some parameter value x_i. Also consider a n-parameter function $y' = f(x_i)$ to be fitted to the given set of data. The residual r_i defined as:

$$r_i = y' - y_i \tag{D.1}$$

is used to determine the external spread of the data, σ_{ext}:

$$\sigma_{ext}^2 = \frac{1}{N-n}\left(\frac{\sum r_i^2 w_i^2}{\sum w_i^2}\right), \tag{D.2}$$

where the squared residuals have been weighted with individual weights w_i:

$$w_i = \frac{1}{\sigma_i}, \tag{D.3}$$

and the ratio has been reduced by the number of free parameters $N - n$. Statistics alone determine the internal uncertainty, σ_{int}, given by:

$$\sigma_{int}^2 = \frac{1}{\sum w_i^2} \tag{D.4}$$

and provides χ_R^2 when combined with the external uncertainty:

$$\chi_R^2 = \frac{\sigma_{ext}^2}{\sigma_{int}^2} = \frac{1}{N-n}\left(\sum r_i^2 w_i^2\right). \tag{D.5}$$

Equation D.5 produces the traditional definition of χ_R^2 as the sum of the square of the weighted residuals reduced by the number of degrees of freedom in the fit. Minimizing χ_R^2, also referred to as the least squares method, yields the best fit for the specific function used. For example, the average of a given set of data is obtained by minimizing χ_R^2 with the function $y' = \overline{y}$. Minimizing Eq. D.5 requires setting the derivative of χ_R^2 with respect to $\overline{y}$ to be zero:

$$\frac{\partial \chi_R^2}{\partial \overline{y}} = \frac{1}{N-n}\sum -2(y_i - \overline{y})w_i^2 = 0. \tag{D.6}$$

After some simple algebra:

$$\sum 2y_i w_i^2 = \sum 2\overline{y} w_i^2. \tag{D.7}$$

Therefore:

$$\overline{y} = \frac{\sum y_i w_i^2}{\sum w_i^2}, \tag{D.8}$$

in which $\overline{y}$ is commonly known as the weighted average. With more complicated functions, such as one which describes the time of flight of ions reaching a MCP detector after ejection from the Penning trap, computer algorithms are used to determine the parameters of the particular function so that χ_R^2 is minimized. The Marquardt method is commonly used and is the one utilized for analyzing data obtained with the CPT. Reference [77] provides a more complete description of the computer algorithms used to determine the parameters and their uncertainties.

Given a function $f(u, v, w, ...)$ with independent parameters u, v, w, ... the uncertainty in the function, σ_f, can be determined from the individual uncertainties in the parameters, σ_u, σ_v, σ_w, ... through the error propagation formula:

$$\sigma_f^2 = \sigma_u^2 \left(\frac{\partial f}{\partial u}\right)^2 + \sigma_v^2 \left(\frac{\partial f}{\partial v}\right)^2 + \sigma_w^2 \left(\frac{\partial f}{\partial w}\right)^2 + ... \tag{D.9}$$

The derivation of this equation has implicitly assumed the parameters were completely independent of one another. If this assumption is not valid, then the formula would have to be modified to include the addition of covariance terms of the nature:

$$2\sigma_{uv}^2 \left(\frac{\partial f}{\partial u}\right)\left(\frac{\partial f}{\partial v}\right), 2\sigma_{uw}^2 \left(\frac{\partial f}{\partial u}\right)\left(\frac{\partial f}{\partial w}\right), 2\sigma_{vw}^2 \left(\frac{\partial f}{\partial v}\right)\left(\frac{\partial f}{\partial w}\right), \text{etc.} \tag{D.10}$$

Careful attention was taken to ensure the calculations conducted throughout this thesis used parameters independent from one another, except when fits were performed to the TOF spectra. The functions used for this purpose consisted of parameters which were known to be correlated with each other, but the cyclotron frequency was the only parameter extracted from these fits which was used in subsequent calculations. Therefore, the final uncertainties in the masses reported in this thesis are accurate, but the masses will be correlated in situations when they were determined with the same series of calibration measurements.

Appendix E

Stellar reaction rates

Determining the nuclear flow of events requires a knowledge of how probable, or equivalently how quickly, the reactions in the sequence occur. The cross section for a particular reaction, symbolized as σ, is a measure of the probability of that reaction occurring. Classically, the cross section can be thought of as an effective area, traditionally reported in units of barns, b, where 1 b $= 10^{-28}$ m^2, within which an incident particle must pass to react with a target particle. This somewhat simplistic and erroneous statement suggests the cross section depends only upon the sum of the individual radii, r_1 and r_2, of the two nuclei such that $\sigma = \pi(r_1 + r_2)^2$. Actually, the cross section must be treated quantum mechanically and is usually dependent upon the energy, and thus velocity, of the projectile. Even so, the classical treatment provides a more intuitive feel for the cross section and this view will be continued for the sake of simplicity. Given a number density, n_t of target nuclei each with a cross sectional area of $\sigma(v)$, the total effective area established by the target is equal to the product, $n_t\sigma(v)$. The flux of projectile nuclei which pass through this area is $n_p v$ where n_p represents the number density of the incident nuclei and v is the velocity of the nuclei. Therefore, the reaction rate, r, between the incident and target nuclei can be written as:

$$r = n_p n_t v\sigma(v). \tag{E.1}$$

Here, the reaction rate is expressed in units of reactions per cubic centimeter per second. Note that in deriving Eq. E.1, the target nuclei were assumed to be at rest and the incident nuclei were the only particles moving with velocity v. However, any reaction between two nuclei can be transformed into a reference frame where one nuclei is at rest while the other has a velocity v. Therefore, the velocity in Eq. E.1 actually represents the relative velocity between the two nuclei.

For a gas in thermodynamic equilibrium, the spectrum of relative velocities can be represented by a probability distribution described by:

$$\int_0^\infty \phi(v)dv = 1 \tag{E.2}$$

such that $\phi(v)dv$ signifies the probability of finding a particle with velocity between v and $v+dv$. This distribution must be folded into Eq. E.1 which yields:

$$r = n_p n_t < \sigma v > \tag{E.3}$$

for the reaction rate with:

$$< \sigma v >= \int_0^\infty \phi(v)v\sigma(v)dv, \tag{E.4}$$

where $< \sigma v >$ is interpreted as the velocity averaged cross section, or the reaction rate per pair of particles.

For most stellar media, the gas is nondegenerate and nonrelativistic and can therefore be described by a Maxwell-Boltzmann velocity distribution:

$$\phi(v) = 4\pi v^2 \left(\frac{m}{2\pi kT}\right)^{3/2} \exp\left(-\frac{mv^2}{2kT}\right) \tag{E.5}$$

for particles of mass m in an environment at temperature T. The constant k refers to the Boltzmann constant. In general, each set of particles in Eq. E.1 can be described with its own Maxwell-Boltzmann distribution:

$$\phi(v_p) = 4\pi v_p^2 \left(\frac{m_p}{2\pi kT}\right)^{3/2} \exp\left(-\frac{m_p v_p^2}{2kT}\right) \tag{E.6a}$$

$$\phi(v_t) = 4\pi v_t^2 \left(\frac{m_t}{2\pi kT}\right)^{3/2} \exp\left(-\frac{m_t v_t^2}{2kT}\right), \tag{E.6b}$$

such that the reaction rate per pair of particles must take both velocity distributions into account:

$$< \sigma v >= \int_0^\infty \int_0^\infty \phi(v_p)\phi(v_t)\sigma(v) v dv_p dv_t. \tag{E.7}$$

To simplify the mathematical analysis, a conversion to the center of mass frame is appropriate. With v representing the relative velocity, expressed as:

$$v = v_p - v_t \tag{E.8}$$

and V is the center of mass velocity given by:

$$V = \frac{m_p v_p + m_t v_t}{M}, \tag{E.9}$$

where $M = m_p + m_t$ is the combined mass of the reaction pair of particles, then the velocities of each set of particles can be rewritten as:

$$v_p = V + \frac{m_t}{M} v \tag{E.10a}$$

$$v_t = V - \frac{m_p}{M} v. \tag{E.10b}$$

In this way, the product $\phi(v_p)\phi(v_t)$:

$$\left\{4\pi v_p^2 \left(\frac{m_p}{2\pi kT}\right)^{3/2} \exp\left(-\frac{m_p v_p^2}{2kT}\right)\right\} \left\{4\pi v_t^2 \left(\frac{m_t}{2\pi kT}\right)^{3/2} \exp\left(-\frac{m_t v_t^2}{2kT}\right)\right\} \tag{E.11}$$

can be rewritten, after some algebraic steps, as:

$$\left\{4\pi v_p^2 \left(\frac{M}{2\pi kT}\right)^{3/2} \exp\left(-\frac{MV^2}{2kT}\right)\right\} \left\{4\pi v_t^2 \left(\frac{\mu}{2\pi kT}\right)^{3/2} \exp\left(-\frac{\mu v^2}{2kT}\right)\right\} \tag{E.12}$$

where the reduced mass, μ, defined as:

$$\mu = \frac{m_p m_t}{m_p + m_t} = \frac{m_p m_t}{M} \tag{E.13}$$

has been used. Even in this form, the integrand in Eq. E.7 still contains the original velocity terms as a product of $4\pi v_p^2 dv_p$ and $4\pi v_t^2 dv_t$. These terms are equivalent to volume terms in Maxwellian velocity space, and could just as easily be written as a product of d^3v_t and d^3v_p. This latter form allows the theory of jacobian determinants to convert an integral over $d^3v_t d^3v_p$ to one over $d^3v d^3V$. (See Ref. [78] for more details.) The volume terms can then be converted back to the form $(4\pi V^2 dV)(4\pi v^2 dv)$. In this manner, Eq. E.7 can be rewritten as:

$$< \sigma v >= \int_0^\infty \int_0^\infty \phi(V)\phi(v)\sigma(v) v dV dv \tag{E.14}$$

with:

$$\phi(V) = 4\pi V^2 \left(\frac{M}{2\pi kT}\right)^{3/2} \exp\left(-\frac{MV^2}{2kT}\right) \tag{E.15a}$$

$$\phi(v) = 4\pi v^2 \left(\frac{\mu}{2\pi kT}\right)^{3/2} \exp\left(-\frac{\mu v^2}{2kT}\right). \tag{E.15b}$$

Since the cross section depends only on the relative velocity between the two sets of particles, the integral over the center-of-mass velocity can be integrated separately and because $\int_0^\infty \phi(V) dV = 1$, Eq. E.14 can be rewritten as:

$$< \sigma v >= \int_0^\infty 4\pi v^3 \left(\frac{\mu}{2\pi kT}\right)^{3/2} \exp\left(-\frac{\mu v^2}{2kT}\right) \sigma(v) dv. \tag{E.16}$$

This equation can be written using the center-of-mass energy instead of the relative velocity. With $E = \frac{1}{2}\mu v^2$, then:

$$< \sigma v >= \left(\frac{8}{\pi\mu}\right)^{1/2} \frac{1}{(kT)^{3/2}} \int_0^\infty \sigma(E) E \exp\left(-\frac{E}{kT}\right) dE, \tag{E.17}$$

the familiar expression for the reaction rate per particle pair.

In environments with excess energy, or high temperatures, inverse reactions can occur and these reaction rates must also be considered. Consider the forward reaction where particles ‘p’ and ‘t’ fuse together to form particle ‘c’, symbolized as:

$$p + t \rightarrow c. \tag{E.18}$$

In energy-rich environments, the inverse process is possible whereby particle ‘c’ can be destroyed, or disintegrate, back into particles ‘p’ and ‘t’:

$$c \rightarrow p + t. \tag{E.19}$$

Recall that the chemical potential is defined as the change in the energy of a system when one more particle of a particular species is added with the entropy and volume of the system held fixed. Then, under the assumed conditions that each set of particles can be represented by a Maxwell-Boltzmann velocity distribution, the chemical potential can be expressed as:

$$\mu_A = kT \ln \left[\frac{N_A}{g_A} \left(\frac{2\pi\hbar^2}{m_A kT} \right)^{3/2} \right] + m_A \mathrm{c}^2 \tag{E.20}$$

for particles of type ‘A’. Here, c represents the constant speed of light in vacuum, $\hbar$ is the usual Planck’s constant divided by 2π, and g_A is the nuclear partition function as given by the following:

$$g_A = \sum_{\delta} (2J_\delta + 1) \exp\left(-\frac{E_\delta}{kT} \right) \tag{E.21}$$

for states δ of spin J_δ and excitation energy E_δ. Returning to the case at hand as described by Eq. E.18 and Eq. E.19, in chemical equilibrium:

$$\mu_p + \mu_t = \mu_c. \tag{E.22}$$

Therefore, after substituting Eq. E.20 for the different species into Eq.

E.22:

$$kT \ln \left[\frac{N_p N_t}{g_p g_t} \left(\frac{2\pi\hbar^2}{kT} \right)^3 \frac{1}{(m_p m_t)^{3/2}} \right] + (m_p + m_t)\mathrm{c}^2 \tag{E.23}$$
$$= kT \ln \left[\frac{N_c}{g_c} \left(\frac{2\pi\hbar^2}{m_c kT} \right)^{3/2} \right] + m_c\mathrm{c}^2.$$

After some algebra:

$$\ln \left[\frac{N_p N_t}{N_c} \frac{g_c}{g_p g_t} \left(\frac{2\pi\hbar^2}{kT} \right)^{3/2} \left(\frac{m_c}{m_p m_t} \right)^{3/2} \right] = \frac{(m_c - m_p - m_t)\mathrm{c}^2}{kT} \tag{E.24}$$

so that, with $Q = (m_p + m_t - m_c)\mathrm{c}^2$:

$$\frac{N_p N_t}{N_c} = \frac{g_p g_t}{g_c} \left(\frac{kT}{2\pi\hbar^2} \right)^{3/2} \left(\frac{m_p m_t}{m_c} \right)^{3/2} \exp\left(-\frac{Q}{kT} \right). \tag{E.25}$$

From Eq. E.3, the rate of the reaction described by Eq. E.18 in producing particle c from particles p and t can be expressed as:

$$\frac{dN_{pt}}{dt} = -N_p N_t < \sigma v > \tag{E.26}$$

where the negative sign shows that the number of p, t particle pairs, N_{pt}, is decreasing with time. The reaction rate of the inverse reaction illustrated in Eq. E.19 can be formulated using Eq. C.1:

$$\frac{dN_c}{dt} = -\lambda_c N_c, \tag{E.27}$$

with λ_c representing the decay constant for the destruction of particles c. Eventually the two reactions come into chemical equilibrium, at which point the creation of particles c from the reaction between a and b is balanced by the destruction of particles c into a and b. The two rates given by Eq. E.26 and Eq. E.27 are then equal and therefore:

$$\lambda_c = \frac{N_p N_t}{N_c} < \sigma v > . \tag{E.28}$$

Using Eq. E.25, λ_c can be rewritten as:

$$\lambda_c = < \sigma v > \frac{g_p g_t}{g_c} \left(\frac{kT}{2\pi\hbar^2} \right)^{3/2} \left(\frac{m_p m_t}{m_c} \right)^{3/2} \exp\left(-\frac{Q}{kT} \right) \tag{E.29}$$

which relates the photodisintegration rate, λ_c, with the reaction rate per pair of (p,t) particles.

Returning to Eq. E.26, if we reconsider the reaction rate as one which describes the rate of change of the target only, then the equation can be rewritten as:

$$\frac{dN_t}{dt} = -\lambda_t N_t \tag{E.30}$$

in which the decay constant for the target:

$$\lambda_t = N_p < \sigma v > . \tag{E.31}$$

Now with Eq. E.28 and Eq. E.29, the relationship between the forward and inverse decay constants can be determined as:

$$\frac{\lambda_c}{\lambda_t} = \frac{N_t}{N_c} = \frac{1}{N_p} \frac{g_p g_t}{g_c} \left(\frac{kT}{2\pi\hbar^2} \right)^{3/2} \left(\frac{m_p m_t}{m_c} \right)^{3/2} \exp\left(-\frac{Q}{kT} \right) \tag{E.32}$$

which is an important relation in describing the waiting-point concept of the astrophysical rp-process.

Bibliography

[1] H. Schatz, A. Aprahamian, J. Görres, M. Wiescher, T. Rauscher, J. F. Rembges, F.-K. Thielemann, B. Pfeiffer, P. Möller, K.-L. Kratz, H. Herndl, B. A. Brown and H. Rebel, Phys. Rep. **294**, 167 (1998).

[2] M. Wiescher, J. Görres and H. Schatz, J. Phys. G **25**, R133 (1999).

[3] R. K. Wallace and S. E. Woosley, Astrophys. J. Suppl. Ser. **45**, 389 (1981).

[4] T. Strohmayer and L. Bildsten, in *Compact Stellar X-Ray Sources*, edited by W. H. G. Lewin and M. van der Klis, (Cambridge University Press, Cambridge, in press).

[5] G. Audi and A. H. Wapstra, Nucl. Phys. **A595**, 409 (1995).

[6] J. J. Thomson, Phil. Mag. **24**, 209, 668 (1912).

[7] R. C. Barber and K. S. Sharma, Nucl. Instrum. Methods Phys. Res. B **204**, 460 (2003).

[8] R. S. van Dyck, S. L. Zafonte, S. van Liew, D. B. Pinegar and P. B. Schwinberg, Phys. Rev. Lett. **92**, 220802 (2004).

[9] S. Rainville, J. K. Thompson and D. E. Pritchard, Science **303**, 334 (2004).

[10] C. Thibault, R. Klapisch, C. Rigaud, A. M. Poskanzer, R. Prieels, L. Lessard and W. Reisdorf, Phys. Rev. C **12**, 644 (1975).

[11] H. Savajols, Hyperfine Interact. **132**, 245 (2001).

[12] G. Auger *et al.*, Nucl. Instrum. Methods Phys. Res. A **350**, 235 (1994).

[13] H. Geissel *et al.*, Nucl. Phys. **A746**, 150 (2004).

[14] K. Blaum, G. Audi, D. Beck, G. Bollen, P. Delahaye, S. George, C. Guénaut, F. Herfurth, A. Herlert, A. Kellerbauer, H.-J. Kluge, D. Lunney, M. Mukherjee, S. Schwarz, L. Schweikhard and C. Yazidjian, Nucl. Phys. **A752**, 317 (2005).

[15] G. Bollen, S. Becker, H.-J. Kluge, M. König, R. B. Moore, T. Otto, H. Raimbault-Hartmann, G. Savard, L. Schweikhard and H. Stolzenberg, Nucl. Instrum. Methods Phys. Res. A **368**, 675 (1996).

[16] V. S. Kolhinen, S. Kopecky, T. Eronen, U. Hager, J. Hakala, J. Huikari, A. Jokinen, A. Nieminen, S. Rinta-Antila, J. Szerypo and J. Äystö, Nucl. Instrum. Methods Phys. Res. A **528**, 776 (2004).

[17] G. Sikler *et al.*, Nucl. Instrum. Methods Phys. Res. B **204**, 482 (2003).

[18] G. Bollen, S. Schwarz, D. Davies, P. Lofy, D. J. Morrissey, R. Ringle, P. Schury, T. Sun and L. Weissman, Nucl. Phys. **A746**, 597 (2004).

[19] J. Dilling, P. Bricault, M. Smith, H.-J. Kluge and Titan Collaboration, Nucl. Instrum. Methods Phys. Res. B **204**, 492 (2003).

[20] J. Szerypo, D. Habs, S. Heinz, J. Neumayr, P. Thirolf, A. Wilfart and F. Voit, Nucl. Instrum. Methods Phys. Res. B **204**, 512 (2003).

[21] W. Quint, J. Dilling, S. Djekic, H. Häffner, N. Hermanspahn, H.-J. Kluge, G. Marx, R. Moore, D. Rodriguez, J. Schönfelder, G. Sikler, T. Valenzuela, J. Verdú, C. Weber and G. Werth, Hyperfine Interact. **132**, 457 (2001).

[22] H.-J. Kluge and K. Blaum, Nucl. Phys. **A746**, 200 (2004).

[23] P. H. Dawson (Ed.), Quadrupole Mass Spectrometry and its Applications, (Elsevier, Amsterdam, 1976).

[24] I. E. Dayton, F. C. Shoemaker and R. F. Mozley, Rev. Sci. Inst. **25**, 485 (1954).

[25] G. E. Lee-Whiting and L. Yamazaki, Nucl. Instrum. Methods **94**, 319 (1971).

[26] D. R. Denison, J. Vac. Sci. & Tech. **8**, 266 (1971).

[27] J. Y. Tu, J. Phys. E **22**, 368 (1989).

[28] E. A. Mason and E. W. McDaniel, Transport properties of ions in gases, (Wiley, New York, 1988).

[29] P. H. Dawson (Ed.), Quadrupole Mass Spectrometry and its Applications, (American Institute of Physics, New York, 1995).

[30] L. S. Brown and G. Gabrielse, Rev. Mod. Phys. **58**, 233 (1986).

[31] M. König, G. Bollen, H.-J. Kluge, T. Otto and J. Szerypo, Int. J. Mass Spectrom. Ion Process. **142**, 95 (1995).

[32] G. Gräff, H. Kalinowsky and J. Traut, Z. Phys. A **297**, 35 (1980).

[33] J. E. Spencer and H. A. Enge, Nucl. Instrum. Methods **49**, 181 (1967).

[34] G. Savard *et al.*, Nucl. Instrum. Methods Phys. Res. B **204**, 582 (2003).

[35] G. Savard, S. Becker, G. Bollen, H.-J. Kluge, R. B. Moore, T. Otto, L. Schweikhard, H. Stolzenberg and U. Wiess, Phys. Lett. A **158**, 247 (1991).

[36] A. Gavron, Phys. Rev. C **21**, 230 (1980).

[37] H. Betz, Rev. Mod. Phys. **44**, 465 (1972).

[38] C. Boudreau, Master's thesis, McGill University, 2001.

[39] J. V. F. Vaz, Ph.D. thesis, University of Manitoba, 2002.

[40] L. Nikkinen (private communication).

[41] H. Fukutani, Master's thesis, University of Manitoba, 2000.

[42] P. Martinez, Master's thesis, McGill University, 1998.

[43] J. F. Ziegler, J. Biersack and U. Littmark, The Stopping and Range of Ions in Matter, (Pergamon Press, New York, 1985).

[44] J. F. Ziegler, Nucl. Instrum. Methods Phys. Res. B **219**, 1027 (2004).

[45] G. Bollen, Nucl. Phys. **A693**, 3 (2001).

[46] E. D. Donets, Review of Scientific Instruments **69**, 614 (1998).

[47] G. Bollen, R. B. Moore, G. Savard and H. Stolzenberg, J. Appl. Phys. **68**, 4355 (1990).

[48] G. Audi, A. H. Wapstra and C. Thibault, Nucl. Phys. **A729**, 337 (2003).

[49] G. Savard, J. A. Clark, F. Buchinger, J. E. Crawford, S. Gulick, J. C. Hardy, A. A. Hecht, V. E. Iacob, J. K. P. Lee, A. F. Levand, B. F. Lundgren, N. D. Scielzo, K. S. Sharma, I. Tanihata, I. S. Towner, W. Trimble, J. C. Wang, Y. Wang and Z. Zhou, Phys. Rev. C **70**, 042501 (2004).

[50] D. J. Wineland and H. G. Dehmelt, J. Appl. Phys. **46**, 919 (1975).

[51] R. S. van Dyck, F. L. Moore, D. L. Farnham and P. B. Schwinberg, Phys. Rev. A **40**, 6308 (1989).

[52] K. S. Sharma, J. Vaz, R. C. Barber, F. Buchinger, J. A. Clark, J. E. Crawford, H. Fukutani, J. P. Greene, S. Gulick, A. Heinz, J. K. P. Lee, G. Savard, Z. Zhou and J. C. Wang, Eur. Phys. J. A (to be published).

[53] G. Bollen, H.-J. Kluge, M. König, T. Otto, G. Savard, H. Stolzenberg, R. B. Moore, G. Rouleau, G. Audi and Isolde Collaboration, Phys. Rev. C **46**, 2140 (1992).

[54] M. Maier, C. Boudreau, F. Buchinger, J. A. Clark, J. E. Crawford, J. Dilling, H. Fukutani, S. Gulick, J. K. P. Lee, R. B. Moore, G. Savard, J. Schwartz and K. S. Sharma, Hyperfine Interact. **132**, 521 (2001).

[55] O. B. Tarsov and D. Bazin, Nucl. Instrum. Methods Phys. Res. B **204**, 174 (2003).

[56] P. J. Mohr and B. N. Taylor, Rev. Mod. Phys. **77**, 1 (2005).

[57] P. Möller, J. R. Nix, W. D. Myers and W. J. Swiatecki, At. Data Nucl. Data Tables **59**, 185 (1995).

[58] A. S. Lalleman, G. Auger, W. Mittig, M. Chabert, M. Chartier, J. Fermé, A. Gillibert, A. Lépine-Szily, M. Lewitowicz, M. H. Moscatello, N. A. Orr, G. Politi, F. Sarazin, H. Savajols, P. Van Isacker and A. C. C. Villari, Hyperfine Interact. **132**, 315 (2001).

[59] G. F. Lima *et al.*, Phys. Rev. C **65**, 044618 (2002).

[60] A. Wöhr, A. Aprahamian, P. Boutachkov, J. L. Galache, J. Görres, M. Shawcross, A. Teymurazyan, M. C. Wiescher, D. S. Brenner, C. N. Davids, S. M. Fischer, A. M. Heinz, R. V. F. Janssens and D. Seweryniak, Nucl. Phys. **A742**, 349 (2004).

[61] F. Herfurth, G. Audi, D. Beck, K. Blaum, G. Bollen, P. Delahaye, C. Guénaut, A. Kellerbauer, H.-J. Kluge, D. Lunney, D. Rodríguez, S. Saxena, S. Schwarz, L. Schweikhard, G. Sikler and C. Yazidjian, Nucl. Phys. **A746**, 487 (2004).

[62] M. Chartier (private communication).

[63] M. Hausmann *et al.*, Hyperfine Interact. **132**, 291 (2001).

[64] R. C. Pardo, C. N. Davids, M. J. Murphy, E. B. Norman and L. A. Parks, Phys. Rev. C **15**, 1811 (1977).

[65] C. N. Davids and D. R. Goosman, Phys. Rev. C **7**, 122 (1973).

[66] R. Pfaff, D. J. Morrissey, W. Benenson, M. Fauerbach, M. Hellström, C. F. Powell, B. M. Sherrill, M. Steiner and J. A. Winger, Phys. Rev. C **53**, 1753 (1996).

[67] B. A. Brown, R. R. Clement, H. Schatz, A. Volya and W. A. Richter, Phys. Rev. C **65**, 045802 (2002).

[68] T. Rauscher and F. Thielemann, At. Data Nucl. Data Tables **75**, 1 (2000).

[69] P. Baumann, M. Bounajma, A. Huck, G. Klotz, A. Knipper, G. Walter, G. Marguier, C. Richard-Serre, H. Ravn, E. Hagebø, P. Hoff and K. Steffensen, Phys. Rev. C **50**, 1180 (1994).

[70] M. Oinonen, J. Äystö, A. Jokinen, P. Baumann, F. Didierjean, A. Huck, A. Knipper, M. Ramdhane, G. Walter, M. Huyse, P. van Duppen, G. Marguier, Y. Novikov, A. Popov, D. M. Seliverstov and H. Schatz, Phys. Rev. C **61**, 035801 (2000).

[71] B. Blank, S. Andriamonje, S. Czajkowski, F. Davi, R. del Moral, J. P. Dufour, A. Fleury, A. Musquère, M. S. Pravikoff, R. Grzywacz, Z. Janas, M. Pfützner, A. Grewe, A. Heinz, A. Junghans, M. Lewitowicz, J.-E. Sauvestre and C. Donzaud, Phys. Rev. Lett. **74**, 4611 (1995).

[72] B. E. Tomlin, C. J. Barton, N. V. Zamfir, M. A. Caprio, R. L. Gill, R. Krücken, J. R. Novak, J. R. Cooper, K. E. Zyromski, G. Cata-Danil, C. W. Beausang, A. Wolf, N. A. Pietralla, H. Newman, J. Cederkall, B. Liu, Z. Wang, R. F. Casten and D. S. Brenner, Phys. Rev. C **63**, 34314 (2001).

[73] J. A. Clark, G. Savard, K. S. Sharma, J. Vaz, J. C. Wang, Z. Zhou, A. Heinz, B. Blank, F. Buchinger, J. E. Crawford, S. Gulick, J. K. P. Lee, A. F. Levand, D. Seweryniak, G. D. Sprouse and W. Trimble, Phys. Rev. Lett. **92**, 192501 (2004).

[74] M. J. López Jiménez, B. Blank, M. Chartier, S. Czajkowski, P. Dessagne, G. de France, J. Giovinazzo, D. Karamanis, M. Lewitowicz, V. Maslov, C. Miehé, P. H. Regan, M. Stanoiu and M. Wiescher, Phys. Rev. C **66**, 025803 (2002).

[75] G. Savard, F. Buchinger, J. A. Clark, J. E. Crawford, S. Gulick, J. C. Hardy, A. A. Hecht, J. K. P. Lee, A. F. Levand, N. D. Scielzo, H. Sharma, K. S. Sharma, I. Tanihata, A. C. Villari and Y. Wang, Phys. Rev. Lett. (to be published).

[76] A. Einstein, Annalen der Physik **18**, 639 (1905).

[77] P. R. Bevington and D. K. Robinson, Data reduction and error analysis for the physical sciences, (McGraw-Hill, New York, 2003).

[78] D. D. Clayton, Principles of stellar evolution and nucleosynthesis, (University of Chicago Press, Chicago, 1983).